Development of an innovative Metrology Technique for Freeform Optics Based on a Modified Talbot-Wavefront-Sensor

Dissertation zur Erlangung des
akademischen Grades Doktor-Ingenieur (Dr.-Ing.)

vorgelegt der
Fakultät für Maschinenbau der
Technischen Universität Ilmenau

von
Dipl.-Ing (FH) Mohamed Bichra

1. Gutachter: Univ.-Prof. Dr. rer. nat. habil. Stefan Sinzinger
2. Gutachter: Univ.-Prof. Dr.-Ing. habil. Eberhard Manske
3. Gutachter: Univ.-Prof. Dr.-Ing. habil. Martin Hoffmann

Tag der Einreichung: 30.03.2020
Tag der wissenschaftlichen Aussprache: 20.11.2020

urn:nbn:de:gbv:ilm1-2020000589

Abstract

The performance of high-precision optical systems with spherical optics is generally limited by aberrations. By using aspheric and free-form optics, the geometric aberrations can be reduced or eliminated. Meanwhile, the required number of components, size, and weight of the system can be reduced. Nowadays, new production techniques that enable the fabrication of high-precision free-form surfaces exist. However, suitable metrology (universal, highly accurate, contactless, non-expensive and fast/realtime) is the key to the production, development and application of these surfaces. This work describes the derivation, implementation and testing of a new wavefront measuring principle for freeform optics. One of the most relevant features of the presented wavefront sensor is the possibility for simultaneous characterization of the freeform element in transmission and reflection modes. The novel wavefront sensor is based on diffraction theory and Fourier analysis with a modified angular spectrum propagator. From an experimental point of view, the propagation of a wavefront behind a two-dimensional grating is observed. Then, a universal method to extract the phase gradient directly from a recorded intensity image is utilized. For this purpose, the intensity distribution in the spectral range is analyzed and the processing is simplified by a corresponding decomposition of the propagator core. This method works for arbitrary distances behind the grating. Our new formulation is tested by numerous simulations. The wavefront generated by a free-form surface is measured by the new method and compared successfully with the result of a measurement with a commercial Shack-Hartmann sensor. For the measurement of reflecting surfaces, the presented setup for transmitting optical elements is slightly modified. Thus, all optical elements can be placed on a single optical axis without shading between the illumination and the measuring unit. The absence of a side illumination or a conventional beam splitter as well as the use of a partially coherent illumination are the main features of this part of the dissertation.

Zusammenfassung

Die Leistungsfähigkeit hochpräziser optischer Systeme mit sphärischer Optik ist im Allgemeinen durch Aberrationen begrenzt. Durch die Verwendung asphärischer und Freiform-Optiken können die geometrischen Aberrationen reduziert oder beseitigt werden. Gleichzeitig können die erforderliche Anzahl von Komponenten, die Größe und das Gewicht des Systems reduziert werden. Heutzutage existieren neue Produktionstechniken, die die Herstellung hochpräziser Freiformflächen ermöglichen. Eine geeignete Messtechnik (universell, hochgenau, berührungslos, kostengünstig und schnell/echtzeitfähig) ist jedoch der Schlüssel für die Herstellung, Entwicklung und Anwendung dieser Oberflächen. Diese Arbeit beschreibt die Ableitung, Implementierung und Erprobung eines neuen Wellenfront-Messprinzips für Freiformoptik. Eine der wichtigsten Eigenschaften des vorgestellten Wellenfrontsensors ist die Möglichkeit der gleichzeitigen Charakterisierung der Freiform im Transmissions- und Reflexionsmodus. Der neuartige Wellenfrontsensor basiert auf der Beugungstheorie und der Fourier-Analyse mit einem modifizierten Winkelspektrum-Propagator. Aus experimenteller Sicht wird die Ausbreitung einer Wellenfront hinter einem zweidimensionalen Gitter beobachtet. Dann wird ein universelles Verfahren verwendet, um den Phasengradienten direkt aus einem aufgezeichneten Intensitätsbild zu extrahieren. Hierzu wird die Intensitätsverteilung im Spektralbereich analysiert und die Verarbeitung durch eine entsprechende Zerlegung des Propagatorkerns vereinfacht. Diese Methode funktioniert für beliebige Abstände hinter dem Gitter. Unsere neue Formulierung wurde durch zahlreiche Simulationen getestet. Die von einer Freiformfläche erzeugte Wellenfront wird nach der neuen Methode gemessen und mit Messergebnissen eines handelsüblichen Shack-Hartmann-Sensors verglichen. Für die Messung reflektierender Oberflächen wurde der vorgestellte Aufbau leicht modifiziert. Somit können alle optischen Elemente auf einer optischen Achse platziert werden, ohne dass eine Verschattung zwischen der Beleuchtung und der Messeinheit auftritt. Das Fehlen einer seitlichen Beleuchtung oder eines Strahlteilers sowie die Möglichkeit der Verwendung einer partiell kohärenten Beleuchtung sind die Hauptmerkmale des im Rahmen dieser Dissertation erforschten Messsystems.

Content

Acknowledgements

The realization of this thesis was a wonderful opportunity to meet and exchange ideas with many people. I cannot quote them all without exceeding the number of pages that are appropriate for this type of work. I acknowledge that everyone to different degrees, but with the same goodwill, has made a positive contribution to its completion. From this point of view, my recognition debts are enormous.

First of all, I would like to thank my parents, Haj Marhoum Sidi Ahmed Bichra and l haja Lala Aicha Rouhi, who were everything for me and who taught me to choose my own path in life and supported me in all my decisions. They raised me with infinite love. To my father, who died recently and who would be happy to learn that his son has finally finished the work he had started. Mom and Dad, I can't thank you enough.

I thank my brother and my sisters, Aissam, Madiha, Zineb, Assia and Tata, for their support during these years and without whom I would not be here today. A special thank goes to my parents-in-law l haja la Batoul Lokrifa et si l haj Abdeljalil El Mofid.

I am thanking particularly Professor Stefan Sinzinger, my supervisor, for the finesse of his attitude on both human and scientific levels. His successive remarks made it possible for me to improve the different versions of this work. As a supervisor, he always found the right balance between the freedom he left me in choosing the main directions and determining the tracks to be followed. On the other hand, I am deeply acknowledging his total and flawless support in delicate moments. I have always received from him not only the encouragement that a doctoral student needs, but also the valuable practical advice that only a man with human characteristics like him can give away. Thanks to his respectful treating of people, I have always felt comfortable. I am very grateful to him for that. I also thank all employees, especially Dr.-Ing. Nail Sabitov, for the partial reading of this work and the continuous provision of my research questions. Special thanks are addressed to Thomas Meinecke and Prof. Gufran Sayeef Khan for their technical contributions.

Many thanks to Dr. Mostafa Agour from BIAS - Bremen Institute for Applied Beam Technology GmbH for his technical contribution and help in the implementation of the frankot shelappa algorithm. Best thanks to Patrick Feßer for the manufacture and characterization of the diffractive optical elements.

To Dr.-Ing. Wassima El Mofid, my wife. This work owes you a lot ... May it be for you the testimony of my infinite gratitude for these years of understanding and common efforts. You're always there for me, you cheer me up when I'm sad, you encourage me when I give up and you console me when I fail. Words are not much to say thank you for all this, I know, but I wanted to do it. Thank you so much with all my love.

To Yakout, my daughter, all astonished that her father has finally finished "his thesis"! you always gave me hope to move forward.

List of important symbols and abbreviations

Z_t	Talbot distances
d	Grating period
$\mathrm{d_x}$, and $\mathrm{d_y}$	Grating periods
λ	Wavelength
CCD	Charge-Coupled-Device
E	Electric field strength
B	Magnetic flux density
μ_0	Magnetic permeability
ε_0	Electric field constant
j	Current density
ρ	Charge density
$c = \frac{1}{\sqrt{\mu_0 \varepsilon_0}}$	Speed of light in a vacuum
U	Three-dimensional complex amplitude
k	Wave vector
T	Complex amplitude transmission function
A_n	Fourier coefficient
$\omega_{x,y}$	Spatial frequencies
$\mathrm{W(x,y)}$	Wavefront
$\psi(t)$	Relative phase shift
$\phi(x,y,t)$	Phase to be detected
SHS	Shack Hartman Sensor
2D	Two dimentional
$\tau\,(x,y)$	Transparency function
$\tilde{S}_g(\omega_x, \omega_y)$	Spectrum of the transmitted signal
$\tilde{S}(\omega_x, \omega_y)$	Wavefront signal
$\tilde{\tau}(\omega_x, \omega_y)$	Spectrum of the grating transfer function

$\widetilde{P}_z$	Propagation kernel
φ_{z0}	Spherical propagator phase
φ_{zq}	Additive offset
φ_t	Slope of the linear tangential term
$\varphi_t(\omega_x, \omega_y)$	Tangential plane
ω_x and ω_y	Spectral coordinates in x and y direction
$\tilde{S}_C(\omega_x, \omega_y)$	Spectrum of the propagated signal after the grating
$\tilde{I}_C(\omega_x, \omega_y)$	Fourier transform of the propagated wave intensity
$\otimes$	Convolution
$A_{qy,qx}$	Matrix of replica coefficients
ω_{max}	Maximum spatial frequency
ω_{min}	Smallest (basic) frequency of the grating
θ_{min}	Smallest angular step
g_{cam}	Period of the camera
α_{max}	Maximum bandwidth of spatial frequencies accepted by the camera
$\eta(q_x,q_y)$	Efficiency of each diffraction order
α	Absorption
ρ	Reflection
τ	Transmission
SRR_{setup}	“signal-to-back-reflection” ratio of the setup
$\nabla\cdot$	the divergence operator
$\nabla\times$	the curl operator

List of figures

I. Introduction

The humanity has been applying optical laws since time immemorial. For instance, the invention of glass lenses was a big step forward in the human history.

This relatively simple optical instrument has gone through a development period of over 700 years to its present form. The development of other optical devices, such as the telescope and the microscope, has been the basic for several science areas. Current optical systems are usually much more complicated and are typically developed and manufactured within a few months to a few years. Nowadays, optical technologies are being used profitably in all industries.

Despite enormous progress, especially during the last century, the majority of all optical components are still based on relatively simple surface types, which can be mathematically described with a small number of geometrical parameters.

The demand of optical systems with very good imaging properties or else the need of complex illumination systems always require the use of a high number of optical components such as mirrors, lenses or prisms that are perfectly aligned. Due to Fresnel reflections, this e.g. may lead to challenges concerning the optical loss of the overall systems. On the other hand, the field of non-imaging optics strives for high optical efficiencies and therefore for the smallest possible number of optical components.

In classical optical systems mostly spherical lenses are used. The geometry of such optical elements can be fully described by specifying the radii of the surfaces curvature and the lens thickness. A disadvantage of such systems is that very often, many optical elements are needed to correct aberrations, resulting in large and heavy optical systems. If the spherical shell, which describes the surfaces, is replaced by a rotationally symmetrical surface deviating from the spherical shape, then an aspherical lens is obtained. Such aspheres are usually described by the aspheric equation [1] or alternative polynomial representations [2]. Depending on the amount of deviation from the spherical shape, a distinction is made between weak and strong aspheres. The advantage of such aspheres is the greatly increased number of degrees of freedom in terms of optical design. As a result, systems with significantly improved optical properties can be realized with the same number of optical elements. For example, in imaging systems, by the use of only one aspheric, spherical aberration can be completely corrected. Often it is also possible to replace several spherical surfaces with an aspherical surface, which can greatly reduce the size and weight of the system.

Due to these advantages, aspherical optics are increasingly used in modern optical systems [3]. The application of aspheres ranges from cheap plastic lenses to high-end optics such as lithography lenses for integrated circuits production.

Lifting the condition that the surface of the asphere is rotationally symmetric, a so-called free-form surface is obtained [4-6]. Such a free-form surface can be described, for instance, by a two-dimensional polynomial [7]. These optical elements offer an even higher number of degrees of freedom for the optical design compared to aspheres.

Thus, by using free-form surfaces, progressive lenses with a continuous refractive power transition or illumination optics with almost any distribution of the energy density can be realized. An example of a freeform optical element is shown in Fig.1.1.

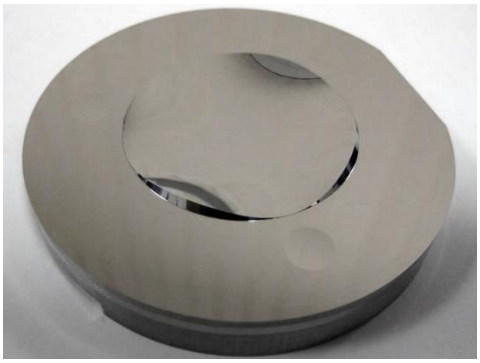

Fig.1.1 Example of a free-form optical surface [8].

An important field of application is in optical systems in which the optical axis is folded [9]. Such folded systems allow a more compact design and are therefore more robust against mechanical disturbances, such as vibrations or thermal influences.

For certain wavelength ranges, such as extreme ultraviolet (EUV) radiation, which is used for the next generation of semiconductor lithography, there are no refractive materials with a tolerable absorption rate, so that it is necessary to avoid lenses. In order to master this challenge, a solution of specular freeform optics is the solution [10,11].

Despite the numerous advantages of aspheres and free-form optics, many optical systems are still calculated based on classical spherical optics. This is due to the higher production costs of the aspherical surfaces. Methods of manufacturing such surfaces have made great progress in recent years. Technologies such as magnetorheological polishing (MRF)[12], ion beam figuring (IBF)[13], diamond turning or precision milling [14] enable flexible, computer-controlled and high-precision production of such surfaces. To achieve the desired nominal shape, an iterative process is usually used in which measurements of the surface are required to control the machining process. Therefore, the surface can only be produced to the maximum extent in the accuracy in which it can be measured. In addition to the sufficient accuracy, there are further requirements for a measuring method to control the production of aspheres and free-form surfaces.

To minimize the manufacturing costs, the aim is to have the shortest possible measuring time with simultaneously high lateral resolution, so that only small dead times occur on the polishing machines. It is also desirable to minimize the response times between measurement and adjustment of the manufacturing parameters in order to reduce rejects and not disrupt the manufacturing process, which can be achieved by near-production metrology.

The in-line characterization of freeform optical elements during the production cycle is still challenging. For the measurement of the shape or the wavefront of optically smooth surfaces, there is currently a wide range of methods that allow a three-dimensional measurement. The most common techniques are contact or tactile coordinate measuring machines whose

application aims to measure a complex surface. Nevertheless, these are limited in spatial resolution. Another disadvantage is the long measuring time. In order to achieve reasonable measurement results, a vibration-free environment must be guaranteed. Therefore, these measurement methods are used for the characterization of few samples rather than for in process control. The integration into a Computerized Numerical Control (CNC) machine-based fabrication process is not possible.

Other measuring methods use the properties of light as an electromagnetic wave to measure wavefronts. The tested object is illuminated with a well-defined wavefront. The latter is reflected at the tested surface. For the transmission, the light passes through the tested objects. In both cases, the wavefront is recorded and analyzed with different principles (measuring devices).

For the reflection mode, the measuring devices or their modules must not be positioned in the beam path of the lighting. Otherwise, the entire test object or a part of the optical components is shaded. This problem is circumvented in practice by the use of beam splitters or slightly tilted illumination of the reflective test object. These variants lead to an increase of the measuring setups dimensions or to complex configurations.

The desirable features of an ideal measuring method are shown schematically in Fig 1.2.

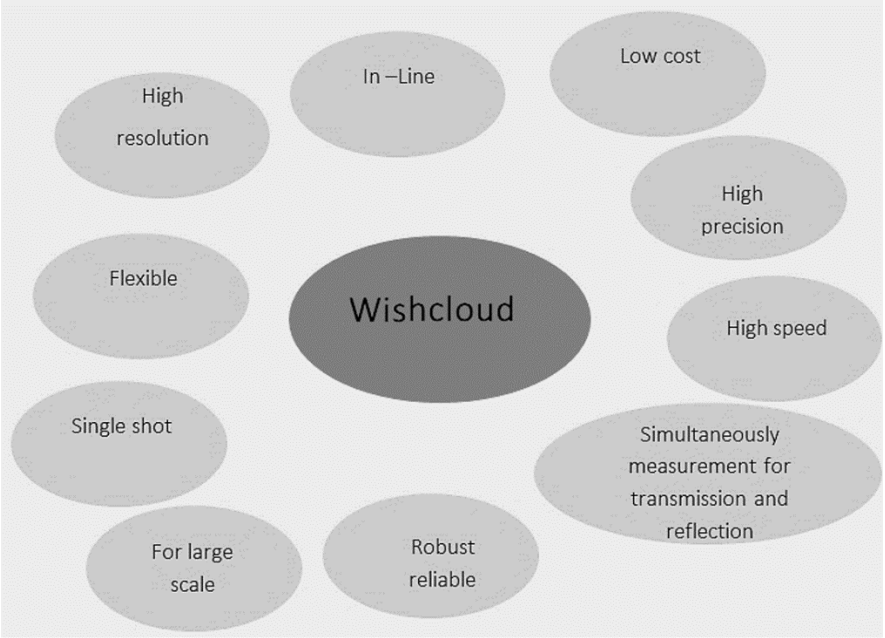

Fig.1.2 The Wishcloud of an ideal measuring method.

Despite numerous extensive research works, there are no simple measuring systems on the market for the simultaneous measurement of transmission and reflection surfaces without the use of conventional beam splitter or complex side lighting systems.

This dissertation offers an innovative solution to this challenge without any mechanical movements or adjustment during the measuring process. The other main objective of this work

is the development of a universal measurement method that allows a simultaneous characterization of the freeform in reflection as well as in transmission modes.
After a brief introduction of the current state of the art, a general summary of the established measuring approach is presented. The third chapter is setting out the principle of the developed measurement method and its theory. It is based on diffraction theory and Fourier analysis. It allows observing the propagation of a wavefront behind a two-dimensional lattice (grating) at known distances. This theory represents a universal method for extracting the phase gradient directly from a recorded intensity image. By additionally positioning a point light source in the measurement setup, the same theory can also be used for reflective surfaces.
The theory in question is then confirmed in the following chapters on the basis of various simulations. In the first section of the fourth chapter, freeform wavefronts are modulated with an amplitude diffraction grating and the result is propagated to different distances behind the grating. From the extracted intensities, the theory is numerically tested under ideal conditions. The second section examines the influence of tolerance on measurement accuracy.
The penultimate chapter introduces the experimental implementation of the presented method. The theory is tested on the example of a phase plate. A commercial Shack Hartman sensor is used as a comparative measurement method. The first section of this chapter describes the preparation, production and characterization of the used elements. Subsequently, a test setup that enables a simultaneous comparison of the two measuring methods is demonstrated. A statistical study is then presented. Finally, the expansion of the theory to the reflection approach was experimented and confirmed by the SHS.

II. Fundamentals and state of the art

Nowadays the wavefront analysis of freeform optical elements can be determined in interferometric and non-interferometric ways. There are other options such as laser telemetry and mechanical scanning.
In the present dissertation, an innovative measurement method based on the Talbot effect is reported. The following section contains a short derivation of the Talbot effect theory and a general summary of the established wavefront measurement methods for the characterization of optical surfaces.

2.1 Talbot effect:

A coherent plane wave illuminates an object with a periodic amplitude transmission function. Replications of the complex amplitude, so-called self-images, can be observed behind the object at certain distances. This effect is known as the Talbot effect and was first observed by William Henry Fox Talbot in 1836 [15]. 45 years later, the theory of this effect was examined by Lord Rayleigh and derived for planar waves [16]. The Talbot effect can also be described using the Rayleigh-Sommerfeld-Debye theory or the plane-wave theory.
In fact, a Talbot interferometer consists of a diffraction grating that splits an incident coherent light wave into several diffraction orders. The interference of the diffraction orders creates a periodic interference pattern at certain distances called Talbot distances. Those are depending on the Illumination´s wavelength λ and the grating´s period d. It is a diffraction-interference phenomenon that occurs in the field of Fresnel diffraction [17-23] [Fig2.1].

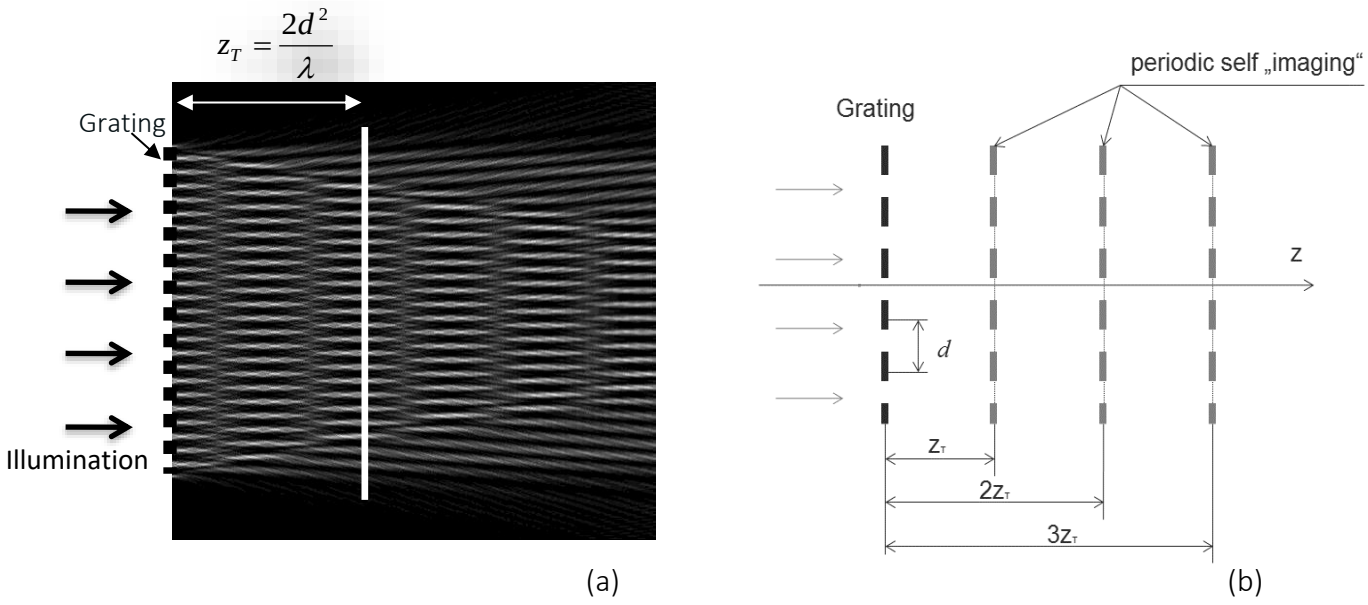

Fig.2.1 (a) Simulation of Talbot effect with a plane wavefront, (b) Schematic illustration of the periodic self-imaging.

The Talbot interferometer belongs to the group of common path interferometers. The division into several interferometer arms is therefore not necessary. If the diffractive grating is illuminated with a spatially coherent wavefront with aberrations, then the self-reproduced image can be described with the field of local displacements, which are proportional to the phase gradients of the incident wavefront [24-26] [Fig2.2].
The shifts of the properly chosen image parts provide information about the illumination wavefront slopes [27-29].

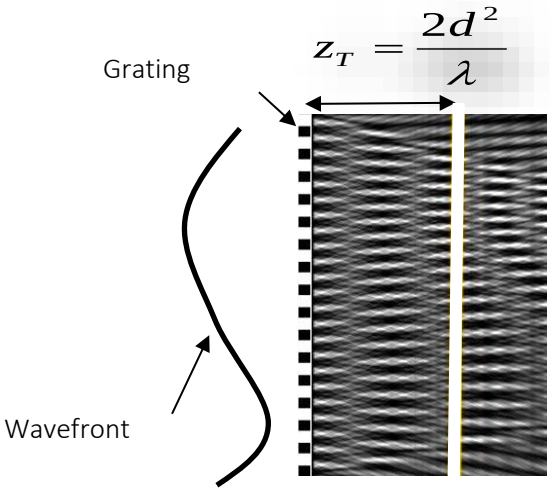

Fig.2.2 Simulation of Talbot effect with a freeform wavefront.

In [30] Takeda presented a method to extract the wavefront from the interference patterns in the Talbot distance. This method is called “analysis of the space carrier”. The discrete Fourier transformation will be applied to the intensity distribution captured by a light sensor and an analysis of the oscillations in the domain of spatial harmonics has to be carried out. K. Ichikawa and A. Lohmann [31] have shown in experimental studies that the periodicity of a diffraction grating can be used to solve the intensity transfer equation at the periodic boundary conditions. Indeed, the diffraction element can be considered as a mask with diffractive properties equivalent to those of a Shack-Hartmann test [32][33].If there is an amplitude grating of the same period and orientation in such a self-imaging plane, which is laterally shifted by half a period in comparison to self-imaging, a dark field image is obtained [Fig.2.3]. The light streaks of the self-image are hidden by the opaque stripes of the second grating and no light enters the detection plane. If the incident light is now disturbed, the diffraction orders of the first grating are influenced, and the self-imaging is disturbed. The stripes deform, and an evaluation is made using the moiré effect. The first grating plays the role of a beam splitter, while the second increases the encoded information in the Fresnel diffraction pattern [34].

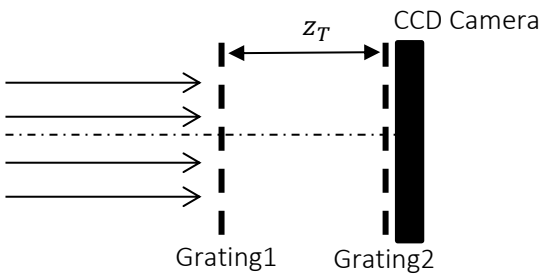

Fig.2.3 Schematic illustration of the Talbot Lau interferometer.

With the Talbot Lau interferometers, the object causing the phase disturbance or the optical element to be measured can either be in front of or behind the first grating. With a small variation in the phase distribution of the object in relation to x and y, it can be shown [35] that the stripes of self-imaging are no longer straight line. The deformation is proportional to the first derivative of the phase function to be examined.
The Talbot interferometer is also suitable for the so-called zero test. To assess the quality of a phase object, the second grating is designed in such a way that it corresponds to the first grating deformed by a standard object. If the object to be tested differs from the standard object, moiré stripes are created. If the object to be tested is perfect, the self-mapping of grating1 after the deformation fits perfectly on grating2, a uniform light or dark area is created. The second grating can be a photo, a slide, a mask of the deformed grating1 [36] or a computer-generated hologram (CGH) [37]. The use of Talbot interferometers as time domain filters [38] [39] is likewise reported in the literature. It is used for the investigation of vibrating phase objects [40] and for measuring step heights with two wavelengths as well [41].
If the period of the grating is much larger than the wavelength, the scalar diffraction can be considered for the light distribution behind the diffractive element. In the next section, the derivation of the Fresnel diffraction integral is briefly discussed. This is important for deriving and understanding the Talbot effect.

2.2 Scalar diffraction theory

Light can be represented as an electromagnetic wave. The wavefront sensor treated in this work can also be explained by the wave characteristics of the light. The Maxwell equations describe the behavior of light waves in space. These represent the mathematical relationships between the electric field strength E and the magnetic flux density B. The following applies [42]:

$$\nabla \times \mathrm{E} = -\frac{\partial \mathrm{B}}{\partial \mathrm{t}}$$

$$\nabla \times \mathrm{B} = \mu_0 \mathrm{j} + \frac{1}{\mathrm{c}^2}\frac{\partial \mathrm{E}}{\partial \mathrm{t}}$$

$$\nabla \cdot \mathrm{E} = \frac{\rho}{\varepsilon_0}$$

$$\nabla \cdot \mathrm{B} = 0 \qquad (2.1)$$

μ_0 denotes the magnetic permeability, ε_0 the electric field constant, j the current density, ρ the charge density and $\mathrm{c} = \frac{1}{\sqrt{\mu_0 \varepsilon_0}}$ the speed of light in a vacuum, under the assumption that the electromagnetic wave is in the charge and current free space $(\rho = 0\,, \mathrm{j} = 0)$. From the calculation rules for vectors, the wave equation for the electric and magnetic fields in vacuum is concluded as follows

$$\Delta \mathrm{E} = \frac{1}{\mathrm{c}^2}\frac{\partial^2 \mathrm{E}}{\partial \mathrm{t}^2}; \qquad \Delta \mathrm{B} = \frac{1}{\mathrm{c}^2}\frac{\partial^2 \mathrm{B}}{\partial \mathrm{t}^2} \tag{2.2}$$

Neglecting the vectorial character and separating the time dependence leads to the Helmholtz equation, which is scalar and stationary

$$\Delta \mathrm{U} + \mathrm{k}^2 \mathrm{U} = 0 \tag{2.3}$$

The light propagates in a homogeneous medium, i.e. there is no coupling between the components of the electric and magnetic fields. U is the three-dimensional complex amplitude, k is the wave vector in the propagation direction $|\mathrm{k}| = \mathrm{k} = \frac{2\pi}{\lambda}$ and λ is the wavelength. The exact solution of the Helmholtz equation for $\mathrm{U}(\mathrm{x}, \mathrm{y}, \mathrm{z})$ is the Debye-Sommerfeld diffraction integral [43]. For relatively small angles ϵ, (ϵ is the angle between the normal vector and the vector $\overrightarrow{\mathrm{r}_{01}}$ that goes from point P_0 in the diffraction plane to the point P_1 shown in the observation plane) [Fig2.4] Kirchhoff's diffraction integral can be used, which is integrated via the diffractive opening A.

$$\mathrm{U}(\mathrm{P1}) = \frac{1}{\mathrm{j}\lambda}\iint_{\Sigma} \mathrm{U}(\mathrm{P}_0)\frac{\mathrm{e}^{\mathrm{j}(\mathrm{k}\mathrm{r}_{01})}}{\mathrm{r}_{01}}\cos(\epsilon)\,\mathrm{ds} \tag{2.4}$$

The integral describes the observed field $\mathrm{U}(\mathrm{P1})$ as a superposition of divergent spherical waves of the form $\frac{\mathrm{e}^{\mathrm{j}(\mathrm{k}\mathrm{r}_{01})}}{\mathrm{r}_{01}}$, which originate from secondary light sources at every point P_0 in the aperture A.

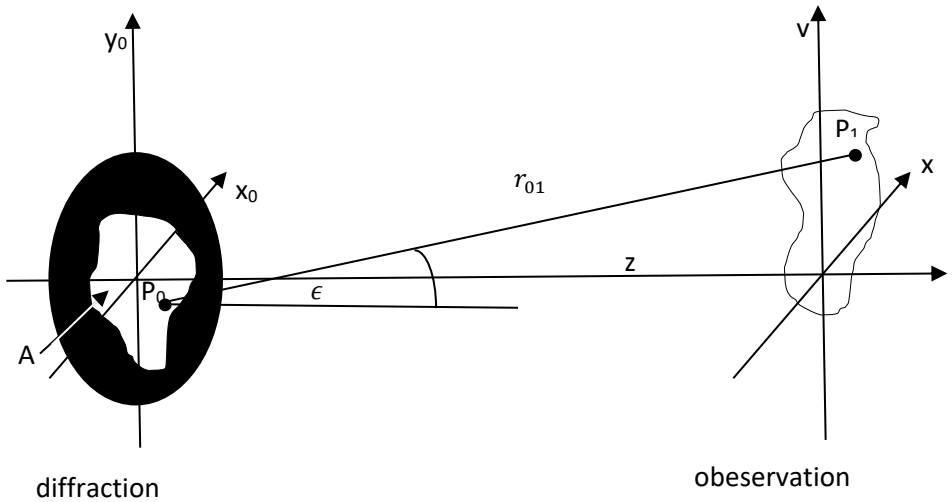

Fig.2.4 Diffraction geometry.

This represents Huygens principle, which describes the spread of any phase area as the sum of many individual spherical waves that coherently interfere to get a resulting wave. This principle is shown in Figure2.5.

Fig.2.5 Clarification of the Huygens principle. This means that a wavefront can be represented by the sum of many point sources. In this picture, the diffraction at a single slit is simulated by the sum of three spherical waves.

The Kirchhoff diffraction integral serves as the starting point for deriving the Fresnel diffraction integral. The Fresnel-Huygens principle can be described as follows:

$$\mathrm{U(x,y)} = \frac{\mathrm{z}}{\mathrm{j\lambda}} \iint_{\Sigma} \mathrm{U_0(x_0,y_0)} \frac{\mathrm{e^{j(kr_{01})}}}{\mathrm{r^2_{01}}} \mathrm{dx_0 dy_0} \tag{2.5}$$

with the vector:

$$\mathrm{r_{01}} = \sqrt{\mathrm{z^2} + (\mathrm{x} - \mathrm{x_0})^2 + (\mathrm{y} - \mathrm{y_0})^2}$$

Where $r_{01} \gg \lambda$ and $\mathrm{U_0(x_0,y_0)}$ is the field distribution in the diffraction plane at $z_0 = 0$. In Fresnel diffraction, which is often also referred to as near-field diffraction, the vector r_{01} in equation (2.5) is approximated by a Taylor series [44].
In order to be able to use the Taylor series, z is first excluded:

$$r_{01} = z\sqrt{1 + \left(\frac{x-x_0}{z}\right)^2 + \left(\frac{y-y_0}{z}\right)^2} \tag{2.6}$$

After developing the series and maintaining the first two terms, the result is:

$$r_{01} \approx z\left[1 + \left(\frac{x-x_0}{z}\right)^2 + \left(\frac{y-y_0}{z}\right)^2\right]$$

$$= z + \frac{(x-x_0)^2}{2z} + \frac{(y-y_0)^2}{2z} \tag{2.7}$$

This means that a spherical wave can be approximated by a parabola. Substituting the approximate r_{01} in the Fresnel-Huygens principle equation (2.5), the next equation will be deduced:

$$U(x,y,z) = \frac{e^{jkz}}{j\lambda z}\int_{-\infty}^{\infty}\int_{-\infty}^{\infty} U_0(x_0,y_0)e^{\frac{j\pi}{\lambda z}[(x-x_0)^2+(y-y_0)^2]}\,dx_0\,dy_0 \qquad (2.8)$$

The resulting equation (2.8) is the Fresnel diffraction integral, which relates the optical field in the observation plane U to the optical field in the object plane U_0 and with the help of this integral, several diffraction problems can be calculated.

2.3 Huygens-Fresnel-Kirchhoff theory of Talbot effect

With the help of the Fresnel integral, the optical field behind a one-dimensional periodic object can now be determined. The complex amplitude transmission function $T$of a periodic object can be represented in the form of Fourier series.

$$T(x) = \sum_n A_n e^{2\pi jn\nu x} \qquad (2.9)$$

A_n is the Fourier coefficient and ν is the spatial frequency which is related to the grating period with the following equation $\nu = \frac{1}{d_x}$. The diffraction grating is illuminated with a plane wave. In front of the grating $(z < 0)$, the field is described as follows:

$$U(x,z) = e^{jkz} \qquad (2.10)$$

If the plane wave reaches the point $= 0^-$, then it is immediately in front of the grating. Directly after the grating, at the point $z = 0^+$, the field is corresponding to the transmission function of the periodic grating:

$$U(x,0^+) = \sum_n A_n e^{2\pi inx} \qquad (2.11)$$

At a distance $z > 0$ from the grating in the propagation direction, the diffraction pattern can be described using the Fresnel integral:

$$U_g(x,z) \approx \int_{-\infty}^{+\infty} U_0(x_0,0)e^{\frac{j\pi}{\lambda z}(x-x_0)^2}dx_0 \qquad (2.12)$$

For U_0, the field $T(x) = \sum_n A_n e^{2\pi jn\nu x}$ at the position $z = 0^+$ is used when solving the Fresnel diffraction integral [45]:

$$U_g(x,z) \approx \int_{-\infty}^{+\infty}\left(\sum_n A_n e^{2\pi inx}\right)e^{\frac{j\pi}{\lambda z}(x-x_0)^2}dx_0$$

$$= \sum_n A_n \int_{-\infty}^{+\infty} e^{\frac{j\pi}{\lambda z}[(x-x_0)^2+2x_0 n\lambda\nu z]}dx_0 \qquad (2.13)$$

After a few mathematical simplifications, the integral is rewritten as follows:

$$U_g(x,z) = \sum_n A_n \, e^{\frac{j\pi}{\lambda z}[x^2-(x-n\lambda\nu z)^2]} \int_{-\infty}^{+\infty} e^{\frac{j\pi}{\lambda z}(x_0-x+n\lambda\nu z)^2} dx_0 \quad (2.14)$$

The integral with the boundaries in infinity provides a constant factor and can be neglected [46]. What remains is:

$$U_g(x,z) = \sum_n A_n \, e^{-j\pi(n\nu)^2\lambda z} e^{2\pi j n\nu x} \quad (2.15)$$

The distribution of the wave field reproduces the same complex amplitude of the grating $T(x)$ when the first exponential equals one. that will be fulfilled if:

$$\pi(n\nu)^2\lambda z = 2\pi \quad (2.16)$$

if we resolve to z, we get:

$$z = z_T = \frac{2}{\lambda\nu^2} = \frac{2d^2}{\lambda} \quad (2.17)$$

In addition to self-imaging in the Talbot distance, there are other images of the periodic grating at other distances. These distances called fractional Talbot distances and can be calculated as follows:

$$z_F^l = \frac{(2l-1)d^2}{\lambda} \; ; l \in \mathbb{N} \quad (2.18)$$

2.4 State of art:

➢ Shack Hartmann Test

A prominent tool for the wavefront analysis is the Shack-Hartmann sensor. It consists of a regular matrix of homogeneous micro-lenses and a common solid-state sensor array in their focal plane. With each micro-lens, a subarray is linked. Each subarray, called pixel cell, contains $m \cdot n = N_{cell}$ pixel elements. Shack-Hartmann sensors are applied in several areas such as adaptive optics in astronomy [47], ophthalmology [48], inspection of local profiles of extended surfaces, etc. The classical Shack-Hartmann analyzer is a technically simple achromatic measurement system. It determines the profile of an unknown wave by measuring the decentering of the light spots formed in the focal plane of a micro-lens matrix (Fig.2.6). This field of eccentric spots is called a Hartmann-gram. Depending on the local gradient of the incident wavefront in lateral x and y direction, the light beam is focused locally. This results in a lateral lag of its focal spot on the pixel cell. While a plane wave causes a mesh of equal spaced foci on the sensor array (regular separation), any arbitrary wavefront distorts this pattern. The local variations of its phase should be nevertheless small with respect to the size of a micro-lens pupil, so that they are taken as average partial derivatives $\Delta W_{x,y}$ [48] of the incident wavefront $W(x,y) = \frac{\phi(x,y)\lambda}{2\pi}$.

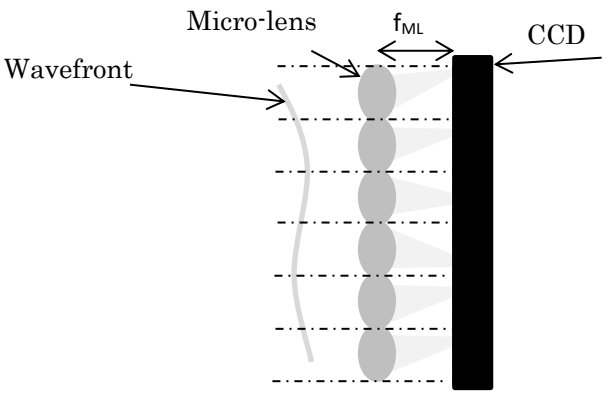

Fig.2.6 Schematic representation of the Shack Hartmann sensor.

$$\Delta x_{m,n} = \frac{f.\partial W_x(m,n)}{\sqrt{1+\partial W_x^2(m,n)}} \approx f.\partial W_x \quad , \quad \Delta y_{m,n} = \frac{f.\partial W_y(m,n)}{\sqrt{1+\partial W_y^2(m,n)}} \approx f.\partial W_y \tag{2.19}$$

$$\Delta W_x = \frac{\int\int \frac{\partial W(m,n)}{\Delta x} dxdy}{d^2} \quad , \quad \Delta W_y = \frac{\int\int \frac{\partial W(m,n)}{\Delta y} dxdy}{d^2} \tag{2.20}$$

In the equations (2.19) and (2.20), the parameter d represents the periodicity and f the focal length of the micro-lenses. In terms of the photodetector, the sampling of a pupil image takes place on a certain number of pixels, so that the position of its center of gravity is not always obvious. Under the influence of the aberrations, its energy peak can degrade considerably and thus decrease the accuracy of the decentering measurement. In the cases when the experiment requires a very precise measurement (analysis of low deformations), the micro-lenses are constrained to have a large focal length and, consequently, a reduced aperture. Conversely, short-focal micro-lenses are used when measuring large oscillations. Considering the dynamic range, the Shack-Hartmann test is limited to the maximum measurable slope defined by the numerical aperture of a micro-lens. Indeed, the beams refracted at the edges of certain openings where the local slopes vary greatly, are likely to be perturbed by the neighboring beams. To avoid the discontinuity of the phase shift between the pupils, the difference of displacement of the two neighboring spots must be less than half the period of the array [49]:

$$\left|\frac{\partial W(m,n)}{\partial x} - \frac{\partial W(m,n\pm1)}{\partial x}\right| < \frac{d}{2f} \tag{2.21}$$

This explains the advantage of sampling as fine as possible with dense micro-lenses. Moreover, in order to correctly detect the central peak of the pupillary image, the peak is supposed to have a size ρ smaller than the separation of the micro-lenses, in other words to correspond to the equation:

$$\rho = \frac{f*\lambda}{d} \tag{2.22}$$

The maximum dynamic range of the classical Shack-Hartmann analyzer is expressed as follows:

$$\Delta W_{max} = \frac{\left(\frac{d}{2}-\rho\right)*N_{lens}*d}{f} \quad (2.23)$$

Where the N_{lens} parameter is the number of pupils in the matrix. Once the field of partial derivatives is obtained, the unknown phase can be approximated with its polynomial decomposition ("modal" reconstruction) or numerically integrated ("zonal" reconstruction). An interesting idea about the Shack-Hartmann analyzer appears in the publication [50]. The authors were able to give the conventional instrument a variable sensitivity. They have substituted the traditional static micro-lenses with a programmable spatial light modulator (SLM), capable of generating on its liquid crystal display (LCD) a Fresnel diffractive lens array with the desired focal length f and geometry. The new properties acquired by the instrument are as follows:

- Great flexibility due to the instantaneous change of the parameters of the diffracting wavefront,
- A multiresolution as a function of the chosen focal length,
- The possibility of correcting the shape of the degraded spots without modifying their position in the pupil.

The latter property is extremely valuable as it contributes to the detection of the exact spot position. Finally, the resolution of the device depends on the minimum focal length displayed on the SLM [50]:

$$f_{min} = \frac{Nd^2}{\lambda} \quad (2.24)$$

Where N, d and λ are respectively the number of pixels constituting a Fresnel micro-lens, the periodicity of the lenses in the matrix and the wavelength of the incident light. In the interest of improving the dynamic range of the conventional Shack Hartmann sensor, the focal length of lenslet components can be reduced. Nevertheless, the sensitivity of the WFS in this case is reduced. The author in [51] solved this problem by using bifocal holographic lenslets. The lenslet is combined with a holographic optical element (HOE). These lenses have two focal planes in which two sensors are placed. In the case of small distortions, the long focal length arm of the WFS, which has the higher sensitivity, is used. While in the case of large distortions, when can occur the effect of “missing dot”, the data from the short focal length can be used [52].

➢ Differential analyzer

To measure the curvature, which is the second derivative of a wavefront passing the pupil of a telescope, F. Roddier proposed a different analyzer [53]. This includes a Hartmann mask (a matrix of regularly spaced holes), a variable focal length lens and an imaging lens conjugated with a CCD sensor.

The underlying technique of characterizing the phase variations consists in comparing the lateral deviations $\Delta x, \Delta x'$ of the light beams passing through the measurement planes 1 and 2 [Fig.2.7] symmetric with respect to the lens. This configuration of the analyzer doubles its sensitivity as for the traditional instrument based on a Hartmann mask. If the vergence of the lens in the middle of the system is changed, the intensity distributions captured in the measurement planes 1 and 2 can be imaged in the photodetector plane. By modifying the defocusing parameter l, the sensitivity of the analyzer is adjusted to the dynamics of the CCD matrix where the light beams are subjected to extremely variable atmospheric turbulence.

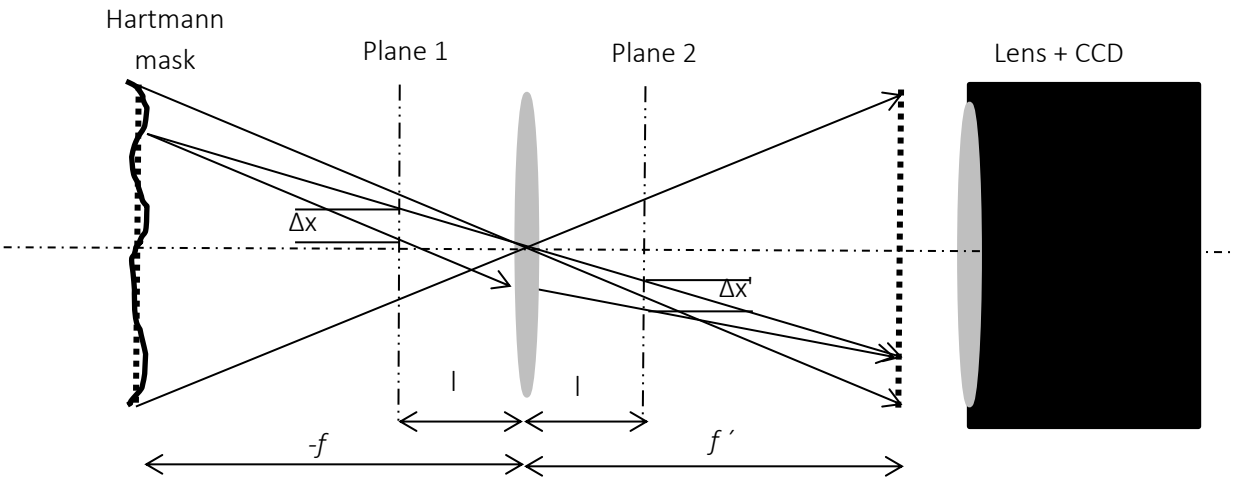

Fig.2.7 Schematic representation of the differential analyzer. The traditional wavefront characterization technique by means of a Hartmann-mask is combined with a comparison of the deviations of the light beams measured in two symmetric planes 1 and 2.

- Interferometer with temporal modulation

The interferometer tools are based on the comparison of the unknown wave to a reference wave. The temporal modulation of the reference wave has found an application in the generation of a controlled variable phase shift, which is introduced into the interferogram during its sequential acquisition. This principle is executed in particular in a speckle interferometer [54][55] used for the detection of static and / or dynamic deformations of the optically diffusing surfaces. The phase of the probe beam is coded by the intensity of M interferograms as a function of time:

$$\mathrm{I(x,y,t)} = \mathrm{I_0(x,y,t)} + \mathrm{I_m(x,y,t)} \cdot \cos[\phi(\mathrm{x,y,t}) + \Psi \mathrm{t}]$$

$$\mathrm{I(x,y,t)} = \mathrm{I_0(x,y,t)} + \frac{\mathrm{I_m(x,y,t)}}{2}(\mathrm{e}^{\mathrm{i}[\phi(\mathrm{x,y,t})+\Psi(\mathrm{t})]} + \mathrm{e}^{-\mathrm{i}[\phi(\mathrm{x,y,t})+\Psi(\mathrm{t})]}) \qquad (2.25)$$

Where $I_0(x, y, t)$ and $I_m(x, y, t)$ represent respectively the continuous background and the temporal variation of the fringes. $\phi(\mathrm{x,y,t})$ is the phase to be detected, while ψ indicates the linear phase shift introduced in the reference wave over time between two successive acquisitions.

To modulate the temporal carrier, we consider, for instance, a Pockels effect element that produces the relative phase shift $\psi = 0, \frac{\pi}{2}, \pi, \frac{3\pi}{2}$ in a repetitive way. Since in this case the analysis of the fringes focuses on their evolution over time, the signal in each pixel of the sensor is treated independently of the others. A Fourier transform is applied for separating the temporal carrier from the other harmonics in the frequency domain. If the modulation frequency of the reference wave is much greater than the desired phase variation, a low-pass filter easily performs the insulation of the carrier $I^1(t) = \frac{I_m}{2} e^{i[\phi(t)+\Psi(t)]}$ before undergoing an inverse Fourier transform. The access to the imaginary part of the signal after the filtering gives the phase:

$$\phi(t) + \Psi(t) = \arctan\{\frac{Im[I^1(t)]}{Re[I^1(t)]}\} \quad (2.26)$$

From which the relative phase shift $\psi(t)$ from the modulator must be deduced. The evaluation of the phase in all the pixels of the interferogram sequence completes the topography of the entire wavefront. However, the nature of the $\arctan(-)$ function, used in the extraction of the data on the phase of the unknown wave, bends the detected phase profile. Nevertheless, it is possible to erase its discontinuities by submitting it to an unfolding procedure. In general, the temporal modulation interferometry performs phase measurement (sub-nanometer scale) more precisely than spatial modulation techniques. On the other hand, it requires complicated modulation equipment; capable of maintaining its characteristics stable during the experiment (The time of the video sequence is typically $120 - 500\, ms$ depending on the number of images). Regarding the Nyquist sampling, the phase variation introduced in the interferometer between two successive acquisitions must not exceed the value $\frac{\pi}{2}$. Moreover, the temporal modulation retains its functionality in the presence of an extended light source as long as its coherence length is sufficient to ensure that the waves are offset.

- Progressive shift phase profilometer

The phase profilometer, with a progressive offset of the reference wave, modulates the wavefront spatially [56]. Due to its simplicity of the phase measurement (the so-called "direct" method) and its outstanding high precision $(\lambda/1000 \text{ or } < 1 \text{ nm})$ it has a strong reputation, particularly in the industry. At least 3 phase-shifted interferograms must be captured. The actual phase distribution is determined by a simple calculation algorithm [57]:

$$I_i(x,y) = I_0(x,y)\{1 + \mu \cdot \text{sinc}(\Delta/2)\cos[\phi(x,y) + \alpha_i]\}, \quad \alpha_i = \frac{i2\pi}{N}, i = 1, \dots N \quad (2.27)$$

There are three unknowns: the intensity of the continuous background $I_0(x,y)$, the phase $\phi(x,y)$ of the wave to be characterized, and the depth of the fringe's modulation μ. The parameter α_i defines the relative average phase introduced before the i^{th} acquisition and Δ is the phase shift carried out during an acquisition.

Since vibrations can seriously distort the offset of the reference wave, a stable configuration of Michelson type or Twyman-Green interferometer are often adopted. Such a setup has an adjustable arm by means of a movable mirror attached to the piezoelectric support (PZT) which moves it. Supplied via a high-voltage amplifier, the PZT element moves the mirror over a distance of a few µm, either in a continuous linear way (integrating-bucket technique, $0 < \Delta < \pi$) or discretized step by step (phase stepping technique, $\Delta = 0$). The continuous phase shift introduced into the interference pattern is integrated by the photodetector during an acquisition. Since the intensity of the interferogram depends on the relative phase introduced, the characteristic of the PZT engine needs to be calibrated.

$$\phi(x,y) = \arctan\left(\frac{\sum_i I_i(x,y)\sin(\alpha_i)}{\sum_i I_i(x,y)\cos(\alpha_i)}\right) \tag{2.28}$$

[58] and [59] state that the generalized form of the sought solution is an application of the least square's method. Depending on the number of acquisitions considered in the processing, a whole range of algorithms for extracting the unknown phase exists. Their detailed comparison is available in [57].

- ✓ Three intensity method [60]
- ✓ Four-intensity method [61]
- ✓ Method of Square [62]

The nature of the $arctan(-)$ function used in the calculation of the phase is at the origin of a modulo π ambiguity suitable for measuring large phase jumps when the separation of the fringes is very small. Some instruments solve this problem by using a second wavelength of the illuminating beam. Thus, the desired phase is deduced as a difference between the values calculated for each wavelength [63]:

$$\phi_{eq}(x,y) = \phi_1(x,y) - \phi_2(x,y) = \frac{2\pi W(x,y)}{\lambda_{eq}} \ , \ \lambda_{eq} = \frac{\lambda_1\lambda_2}{|\lambda_1 - \lambda_2|} \tag{2.29}$$

Other phase profilometers dispose of the measurement ambiguity by combining progressive shift interferometry with coherence-peak sensing [64]. The implementation of this type of apparatus consists of comparing the calculated phase values picked up from the interferograms, first in the position of the best contrast and then in the position of the correlation peak. Nonetheless, the main components of these optical systems such as the high-quality objective and the PZT motor with its feeding equipment are costly. At the price of several tens of thousands of euros in the current instruments market, there is a range of phase-shift profilometers proposed, for example, in [65], in [66] "Veeco Instruments Inc." and in [67] "Zygo".

➢ Tilted wave interferometry

Tilted-wave interferometry is a flexible method to characterize complex aspherical and free-form surfaces [68]. Using a polarizing beam splitter, a coherent light source will be divided into a test and a reference wave.

A combination of micro lens array and pinhole array will be illuminated by the test wave. This combination can be considered as an array of point sources for the test wavefronts. Passing the beam splitter and a collimated optic, the wave fronts resulting are a set of plane wavefronts with different tilt. To compensate the complex spherical form of the test object, the tilted resulting wavefronts are transformed to spherical wavefronts by spherical optics. After being reflected by the test objects, the wavefronts propagate back to the beam splitter, where a part of this reflection is reflected to the camera arm of the interferometer. In the Fourier plane of the imaging system, an aperture stop is located to block high frequency light that would generate fringes with a density higher than the Nyquist criterion. This light interferes with the reference wave on the camera plane. A more detailed description of the measurement principal and the setup can be found in [69-75].

- Null method

In the null element measurement method, a compensating element is used. The null element transforms a spherical or a plane wavefront into one that exactly corresponds to the aspheric surface that is being tested. When the wavefront is reflected from the tested surface, it follows its path. If the surface is perfect then a perfect spherical or plane wavefront will appear, which can be easily evaluated with high accuracy conventional method. This method can be Fizeau interferometer type or Twyman-Green type. The deviation from the desired aspheric shape can be measured. The null element can have various forms. In the following, 3 famous types are shown:

- ✓ Reflective or refractive optics [76].
- ✓ Holographic null optics (computer generated hologram) [77-81].
- ✓ A combination of conventional null optics and computer-generated hologram [82].

- Phase Retrieval

As well as conventional interferometry, the free propagation of the unknown wave can be used to detect its phase coded in the diffraction fringes. The scalar propagation theory of light determines the exact distribution of the complex field of a diffracted wave circulating between two arbitrary planes of the medium. Knowing the initial shape of its amplitude and phase, their distributions at any point of the starting point are found with the calculation of an integral of Kirchhoff [83]. Reverse propagation to the original plane is a deconvolution, being from a mathematical point of view an inverse operation of the convolution between the initial wavefront and the Fresnel nucleus of the medium. According to the adopted approximation, the propagation law takes the form either of the Fresnel transform valid for a near field or of the Fourier transform subjected to Fraunhofer conditions and applicable to a far field. In the characteristic circumstances of quadratic detection where the manipulated light is only known by its intensity, it can be backpropagated based on an estimate of its unknown phase.

Indeed, the size and the geometry of its diffraction fringes implicitly comprise all the information on the original wavefront, necessary to reconstruct it. Contrary to interferometric instruments, diffractive systems are generally not very demanding in sophisticated materials but rely heavily on algorithms of high intellectual value and perform a large amount of calculations. Although these algorithms can consume significant computing resources, thanks to the evolution of the performances of the modern computers, their execution time is becoming increasingly shorter. The typical scope of these techniques is wide. It covers laser beam analysis, aberration and atmospheric turbulence analysis for astronomy telescopes, the determination of the optical properties of an eye, the surfaces of the samples, etc.

- Pyramid wavefront sensors

In 1996, an alternative to the Shack Hartmann wavefront sensor (SHWFS) called pyramid wavefront sensor (PWFS) was proposed. The special feature of the new sensor is the better performance regarding the sensitivity compared with the SHWFS [84,85]. The PWFS consists of a glass pyramid placed in the image plane of the optical system, with the spot focused on the pyramid´s surface. The light is divided into four quadrants and will be imaged on a detector. Hence, all four-sub apertures contain information about the incoming wavefront [86]. The requirements in the design specifications of a pyramid are high. All four surfaces of the pyramid must have the same angle and a good surface flatness. Most importantly, the edges need to be thin and straight. This can therefore be a challenge for manufacturers. The D-PWFS [87] uses two glass pyramids glued back-to-back so that the beam enters the four-facet side and passed through a four-facet. This makes the system less sensitive against the angle tolerances [88] and allows for the best match between the two pyramids to reach an optimal performance. The pyramids are made from different materials, so that the second one can correct the chromatic aberration from the first one. This is done by carefully choosing the indices of refraction for the two pyramids.

- Confocal microscopy

Confocal microscopy is a particular type of optical microscopy where one point of the sample is seen at the same angle by the condenser and the lens. In conventional optical microscopy, for an image to be sharp, the object must be in the focal plane of the optical system. When an object is thick, has a significant relief, or is inclined with respect to the objective, only a part of the object is sharp in the image. To solve this problem, the surface should no longer be illuminated by a beam of white light, but by a laser beam, focused by an objective. The essential principle [89] lies on the presence of the "pinhole" diaphragm in front of the detector conjugated to the focal plane of the objective (confocal planes). This diaphragm having an opening corresponding to the first Airy spot (lateral resolution $\delta x, y = 0.46\lambda / \mathrm{NA}$ [90]) allows the detection of reflectivity signals originating only from the focal plane. The light from the other planes is then blocked. In this way, the images obtained have a very shallow depth of field (of the order of $0.6\ \mu m$ under the best conditions) which can be qualified as optical sections.

The image is constituted point by point by varying step by step the focus in the direction of the z axis and by ensuring the lateral displacement of the laser beam on the sample (scanning system or Nipkow disc). The resolution in z is of the order of 600nm in confocal microscopy. The positioning of the spot in the depth of the sample is generally obtained by moving along the z axis the objective, using a piezoelectric quartz in steps successively from $200 - 300\text{nm}$. The mechanical z-scan required in confocal microscopy can be avoided in chromatic confocal systems [91-93]. For this purpose, the microscope objective is replaced with a hyperchromatic lens that has a well-defined amount of longitudinal chromatic aberration.

- Digital holographic microscopy

Digital holographic microscopy (DHM), based on the direct recording and numerical reconstruction of hologram, is another technique for testing reflection/transmission refractive optics [94- 97]. The recorded hologram at the CCD plane consists of an object wave (O) and a reference wave (R). Both superimpose with an angle q. The recorded hologram is processed numerically and a wrapped phase image can be acquired.
The important object information can be calculated by unwrapping the phase images using mathematical method [97].

- Deflectometry

In order to measure reflective surfaces, the method of deflectometry can be used. It is a simple but powerful measuring method, where the reflection angles of a test surface show local slopes and thus local errors. The slope data can be converted into curvature data, so that sensitivities in the nm range are possible [98-106]. The greatest advantage of the deflectometry is that, with proper experimental setting, there is no retrace error. However, it has a significant challenge regarding the coherent noise.

- Autofocus sensing

Autofocus sensing is a measurement method used in the characterization of free-form surfaces [107]. A focused light spot is illuminated to test the surface mounted on a XY linear stage. A condenser lens is used and displaced along the axis of the incident light, by a piezoelectric actuator, to keep the test surface in focus. The 3D profile coordinates can be obtained from the position's information recorded by the PZT and the linear stage [108-110].

- Scanning probe microscope-based systems

The scanning tunneling microscope (STM), the atomic force microscope (AFM) and the development of other different scanning probe microscopes (SPM), for example the electrostatic force microscope (EFM), the near field microscope (NFOM), the magnetic force microscope (MFM) helped the science and the researchers to explore the Nano world due to its approximate atomic resolution [111-117].

In order to be able to characterize freeform surfaces with large dimensions, a linear stage with high accuracy is usually applied. Therefore, it is very important to minimize the displacement errors of the probe tip in the Z direction and the inclination errors of the XY movement. The inclination and displacement errors are conventionally compensated by using a capacitance sensor [118] and a laser interferometer [119]. The tilt compensation of the linear stage can be done with angle sensors [120]. By a collaboration between Technische Universität Ilmenau and Physikalische Technische Bundesanstalt (PTB), a large-area scanning force microscope (LR-SFM), which is integrated in nano machine (NMM), was developed. It has a maximum measuring volume of $25\ \mathrm{mm}\ \mathrm{x}\ 25\ \mathrm{mm}\ \mathrm{x}\ 5\ \mathrm{mm}$ [121]. In order to minimize the errors in a large range, three interferometers and two angle sensors were integrated into the NMM to scan all six degrees of freedom of the movement stage.

- Mechanical stylus profiling systems

The first mechanical stylus profile system was presented by Schmaltz in 1936 [122]. Mechanical stylus profile systems are more robust and not too sensitive compared to other optical measuring methods. Thanks to these advantages, the industrial sectors still use this method for the characterization of geometrical components [123]. In micro-optics, the mechanical stylus profile systems are in use to detect the surface structures of micro lenses and micro lens arrays [124, 125]. A conventional mechanical stylus profiler system consists of a stylus attached to a cantilever. A linear stage unit along the measured surface moves the tip of the stylus mechanically. Shape variations of the sample move the stylus in the vertical direction. These movements are recorded at the end of the cantilever and are proportional to the z information of the tested object. For the measurement of micro lenses with a photoresist layer, the mechanical stylus could damage the surface [126-133].

2.5 Summary

In summary, no method suitable for measurements in transmission and reflection mode simultaneously is available. For the measurement of reflective surfaces, a beam splitter or a laterally incident illumination has to be used. The overall dimensions of the required measurement setups are, therefore, large and as a result, a high adjustment effort is necessary. Moreover, additional unwanted effects such as multiple propagation and reflection at and between the surfaces of the beam splitters may occur. Besides, the cost of high-quality beam splitters is often very high. All these disadvantages and the high demands on a low-noise environment (mechanical vibrations, temperature stability) make it difficult to directly integrate the presented measuring methods in current production processes, e.g. with a CNC machine.

III. Modified Talbot wavefront sensor

The aim of this dissertation is the introduction of a metrological method for the characterization of freeform surfaces. This method must be able to measure and characterize the optical element in transmission and in reflection without significant modification of the experimental setup. This chapter introduces the measurement concept and the theory of the novel measurement configuration. This theory is based on diffraction and Fourier analysis with a modified angular spectrum propagator. In fact, we observe the propagation of a wavefront behind a two-dimensional grating and present a universal method for extracting the phase gradient directly from a recorded intensity image. For this purpose, the intensity distribution in the spectral range is analyzed and the processing is simplified by a corresponding decomposition of the propagator core. This method works for any known distance behind the grating. In the following, the derivation of the new wavefront measurement principle in transmission is described. By additionally positioning a point light source in the measurement setup, the same theory and arrangement can also be used for reflective surfaces.

3.1 Principle of the modified talbot wavefront sensor

The basic principle of the suggested wavefront sensor in transmission mode is shown schematically in Fig.3.1. An optically transparent freeform object is illuminated with a well-defined planar, partially coherent wavefront. The transmitted wavefront contains information about the shape of the test object and its position relative to the illumination as well as the material properties. This wavefront reaches a binary cross grating. The grating diffracts the wavefront into various diffraction orders. The diffractive element is positioned at a distance $\mathbf{z}$ in front of a $\mathbf{2D}$ detector.

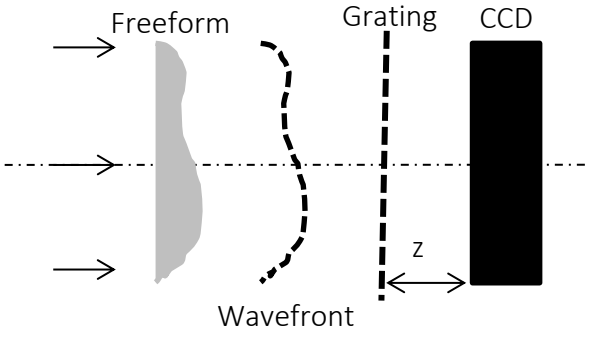

Fig.3.1 Schematic representation of the suggested wavefront sensor.

The used diffractive binary cross-grating has grating periods $\mathrm{d_x}$, and $\mathrm{d_y}$, in the x and y directions, respectively.

In the first step, we define the transparency function $\tau\,(x, y)$ of this optical element:

$$\tau(x,y) = \frac{1}{(2M+1)(2N+1)d_x d_y}\,\mathrm{rect}\left(\frac{x}{(2M+1)d_x}, \frac{y}{(2N+1)d_y}\right) \cdot \frac{4}{d_x d_y}\,\mathrm{rect}\left(\frac{x}{\frac{d_x}{2}}, \frac{y}{\frac{d_y}{2}}\right) \otimes \sum_{l_y=-N}^{+N} \sum_{l_x=-M}^{+M} \delta\left(x - l_x d_x, y - l_y d_y\right) \tag{3.1}$$

$2M$ and $2N$ are integer numbers of the grating periods. The variables I_x and I_y are running integers in the x and y directions, respectively. The first $rect$ term describes spatial observation window with a dimension of $(2M+1)d_x \cdot (2N+1)d_y$. The second $rect$ term in the formula illustrates the width of a single grating structure element of half the size of the grating period $\frac{d_x}{2}$ and $\frac{d_y}{2}$. In order to reproduce the repeating rectangular pattern, this structure element is convolved by a two-dimensional comb function. The spectrum of the transparency function can be described as following:

$$\boldsymbol{\tau}\left(\boldsymbol{\omega_x}, \boldsymbol{\omega_y}\right) = \mathbf{sinc}\left(\frac{(2M+1)\boldsymbol{\omega_x}}{\boldsymbol{\omega_{x0}}}, \frac{(2N+1)\boldsymbol{\omega_y}}{\boldsymbol{\omega_{y0}}}\right) \otimes \mathbf{sinc}\left(\frac{2\boldsymbol{\omega_x}}{\boldsymbol{\omega_{x0}}}, \frac{2\boldsymbol{\omega_y}}{\boldsymbol{\omega_{y0}}}\right) \sum_{q_y=-N}^{N} \sum_{q_x=-M}^{M} \boldsymbol{\delta}\left(\boldsymbol{\omega_x} - \mathbf{q_x}\boldsymbol{\omega_{x0}}, \boldsymbol{\omega_y} - \mathbf{q_y}\boldsymbol{\omega_{y0}}\right) \tag{3.2}$$

With $\omega_{x,y}$ as spatial frequencies, $\omega_{x_0} = 2\pi/dx$ and $\omega_{y_0} = 2\pi/dy$.

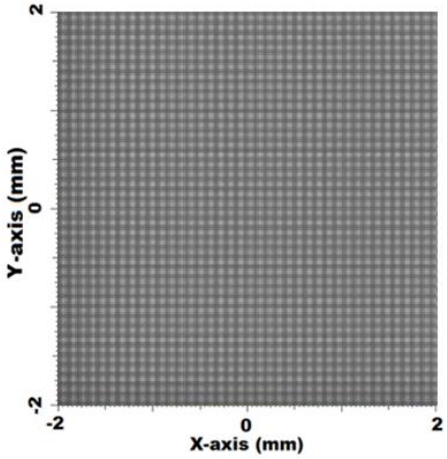

Fig.3.2 Intensity distribution behind the grating at the Talbot distances using Plane Wavefront.

In spectral domain, the binary cross grating produces several spectral dirac pulses. These pulses are spaced by the grating frequencies of ω_{x_0} and ω_{y_0}. The Fourier transform of the spatial window function caused the first sinc term, where M, N are normally too large. Due to this, the function in the

first term becomes very narrow compared to the following terms. Therefore, this term is negligible and can be considered as a dirac pulse. The second $sinc$ term represents the transform of the binary spatial grating. This spectral envelope follows a two-dimensional $sinc$ function of twice the grating frequency so that each dirac pulse is weighted by the corresponding local maxima of the sinc component. The spectrum of the grating transfer function can be simplified to Eq.4.3:

$$\tilde{\tau}(\omega_x, \omega_y) = \sum_{q_y=-N}^{N} \sum_{q_x=-M}^{M} \mathrm{sinc}(2q_x, 2q_y) \cdot \delta(\omega_x - q_x\omega_{x0}, \omega_y - q_y\omega_{y0}) \quad (3.3)$$

The Spectrum of the transmitted signal $\tilde{S}_g(\omega_x, \omega_y)$ behind the amplitude diffraction grating [Fig.3.3] is a convolution of the wavefront signal $\tilde{S}(\omega_x, \omega_y)$ and the grating transfer function $\tilde{\tau}(\omega_x, \omega_y)$ and can be described as follows:

$$\tilde{\mathbf{S}}_g(\boldsymbol{\omega}_x, \boldsymbol{\omega}_y) = \tilde{\mathbf{S}}(\boldsymbol{\omega}_x, \boldsymbol{\omega}_y) \otimes \tilde{\boldsymbol{\tau}}(\boldsymbol{\omega}_x, \boldsymbol{\omega}_y) \quad (3.4)$$

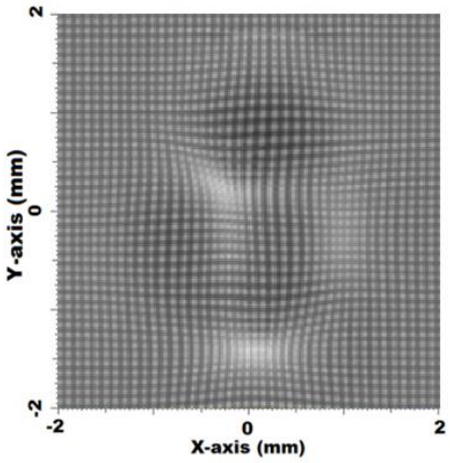

Fig.3.3 Intensity distribution behind the grating at the Talbot distances using Freeform Wavefront.

Due to the convolution with dirac pulses introduced by $\tilde{\boldsymbol{\tau}}(\boldsymbol{\omega}_x, \boldsymbol{\omega}_y)$, the resulting signal spectrum $\tilde{\mathbf{S}}_g(\boldsymbol{\omega}_x, \boldsymbol{\omega}_y)$ is represented by shifted and replicated spectral components of $\tilde{\mathbf{S}}(\boldsymbol{\omega}_x, \boldsymbol{\omega}_y)$ corresponding to Eq 4.2. After the grating, the modulated signal propagates in the direction of the illumination. A goal of this work is the extraction of the wavefront at any positions behind the diffraction element. For that, the numerical propagation is expressed by the angular spectrum method [134-145]. This propagation formulation consists of the multiplication of the spectrum of the modulated signal with the propagation kernel $\widetilde{\mathbf{P}}_z$ (Eq 3.5) in spectral domain:

$$\widetilde{\mathbf{P}}_z(\boldsymbol{\omega}_x, \boldsymbol{\omega}_y) = \exp\left(\mathbf{i}\, \boldsymbol{\varphi}_z(\boldsymbol{\omega}_x, \boldsymbol{\omega}_y)\right) \quad (3.5)$$

where the phase is represented by $\varphi_z(\omega_x, \omega_y) = z\sqrt{k^2 - \omega_x^2 - \omega_y^2}$ with the wave number $k = 2\pi/\lambda$ and λ as the illumination wavelength.

The two-dimensional function $\widetilde{P}_z(\omega_x, \omega_y)$ can be imagined as the upper half of a three-dimensional ellipsoid on a circular ground of spatial frequencies $\omega(\omega_x, \omega_y)$. The actual relationship between the propagation phase and the signal spectrum behind the grating is schematically shown in Fig.3.4.
For $q_x = \pm 1$ and $q_y = 0$, the $-1^{st}, 0$ and $+1^{st}$ orders (replicas) are modulated by different sections of the propagation phase function shown in different colors in Fig. 3.4.

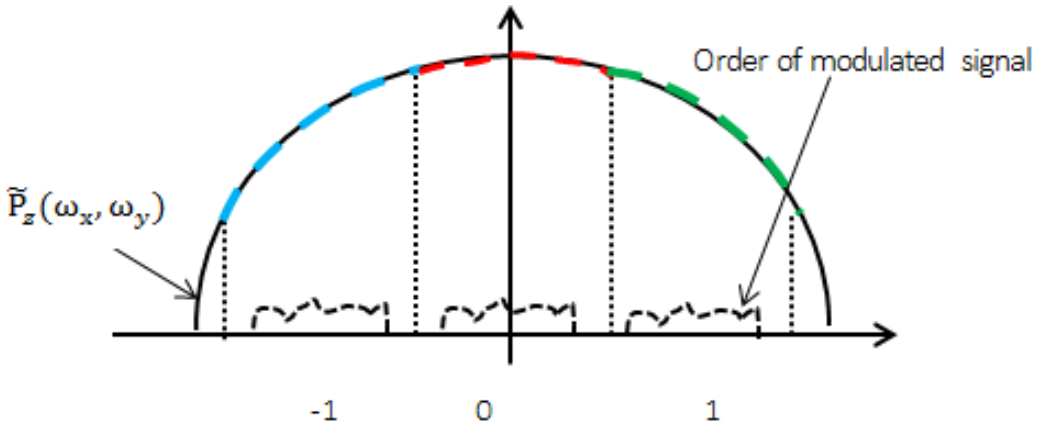

Fig.3.4 Illustration of the cross section of the propagator kernel along the ω_x axis including $-1^{st}, 0$ and $+1^{st}$ orders of the signal spectrum behind the grating. Each replica is modulated by a certain part of the propagator kernel after the propagation operation.

Each replica contains all information of the test signal. However, they differ in the phase introduced by the propagation function. In order to simplify the subsequent signal evaluation, the propagator is represented from the perspective of the spectral replica. The formalism of the actual propagator phase φ_z is simplified by decomposing it as follows:

$$\varphi_z(\omega_x, \omega_y)_{q_x\omega_{x0}, q_y\omega_{y0}} \approx \varphi_{z0} + \varphi_{zq} + \varphi_t \cdot \omega(\omega_x, \omega_y) \tag{3.6}$$

into

- ✓ a term of φ_{z0} which corresponds to the spherical propagator phase near the origin, i.e. at the zero-order replica or without using a cross grating:

$$\varphi_{z0}(\omega_x, \omega_y) = \varphi_z(\omega_x - q_x\omega_{x0}, \omega_y - q_y\omega_{y0}) = \varphi_z(\Delta\omega_x, \Delta\omega_y) \tag{3.7}$$

- ✓ an additive offset of φ_{zq} at the replica frequencies of $q_x\omega_{x0}, q_y\omega_{y0}$:

$$\varphi_{zq}(\omega_x, \omega_y) = \varphi_z(q_x\omega_{x0}, q_y\omega_{y0}) \tag{3.8}$$

- ✓ and a linear (tangential) term having a slope of φ_t.

The significance of these individual portions of the propagator is illustrated in Fig.3.5.

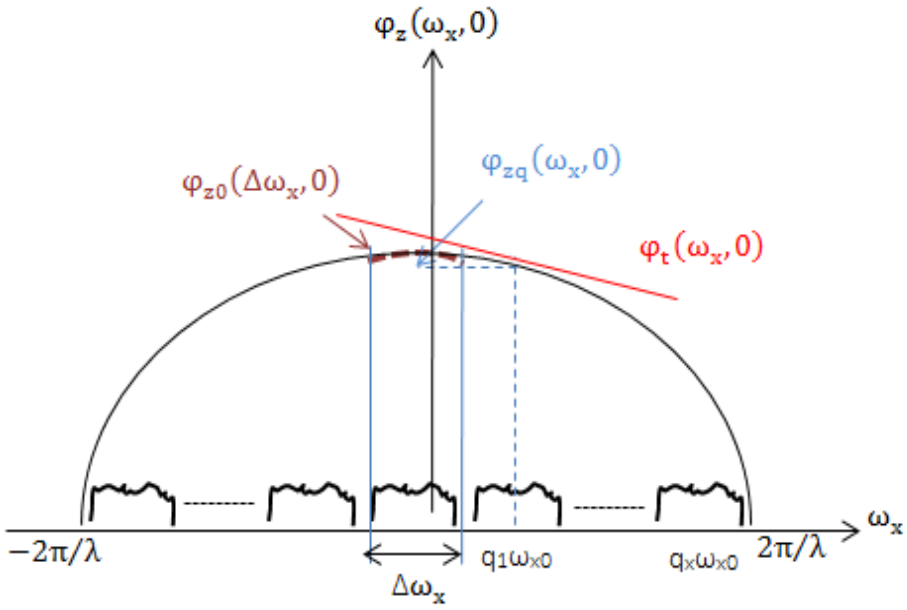

Fig..3.5 Illustration of the decomposition of the propagator phase φ_z along the ω_x axis, φ_{z0} corresponds to the spherical propagator phase part near the origin, additive offset of φ_{zq} at the replica frequencies of $q_x\omega_{x0}$, $\varphi_{t(\omega_x,0)}$ is the tangential plane of the propagator kernel at the spectral coordinate ω_x.

The partial derivation of the propagator kernel results in the tilt of $\varphi_t(\omega_x, \omega_y)$. The tangential plane $\varphi_t(\omega_x, \omega_y)$ is generally expressed for any arbitrary replica $(q_x\omega_{x0}, q_y\omega_{y0})$ by Eq.3.9:

$$\varphi_t(q_x\omega_{x0}, q_y\omega_{y0}) = \left(\frac{\partial\varphi_z}{\partial\omega_x}, \frac{\partial\varphi_z}{\partial\omega_y}\right) = -\frac{z\cdot\omega(q_x\omega_{x0}, q_y\omega_{y0})}{\sqrt{k^2-(q_x\omega_{x0})^2-(q_y\omega_{x0})^2}} = -\frac{z\lambda\cdot(q_xd_y, q_xd_y)}{\sqrt{(d_xd_y)^2-(q_x\lambda d_y)^2-(q_y\lambda d_x)^2}} \quad (3.9)$$

Here, ω_x and ω_y represent the spectral coordinates in x and y directions, respectively. The propagator decomposition to $(q_x, q_y) = (+1, 0)$ is applied and results in $q_x\omega_{x0} = q_x\omega_{x0} = 2\pi/d_x$ and $q_y\omega_{y0} = 0$. The corresponding tilt of the tangential plane at $\omega_{x0} = +2\pi/d_x$; $\omega_{y0} = 0$ is written in Eq. 3.10:

$$\varphi_t(\omega_{x0}, 0) = -\frac{z\lambda}{\sqrt{d_x^2-\lambda^2}} \quad (3.10)$$

In order to evaluate the validity of the introduced approximation, the propagation kernel is simulated using MATLAB(TM). The results are illustrated in Fig.3.6 and Fig.3.7 for an example of a grating with a

period of $d_x = 25\mu m$ illuminated by coherent light of $633nm$ wavelength at 3 different distances $z_1 = 200\mu m$, $z_2 = 700\mu m$ and $z_3 = 2000\mu m$. First, the phase tilt of the kernel propagation is extracted at the position ω_{x0}. Then, the simulated kernel is shifted by $\omega_{x0} = 180rad/mm$. Thereafter, the shifted kernel propagation is multiplied by the extracted phase tilt.

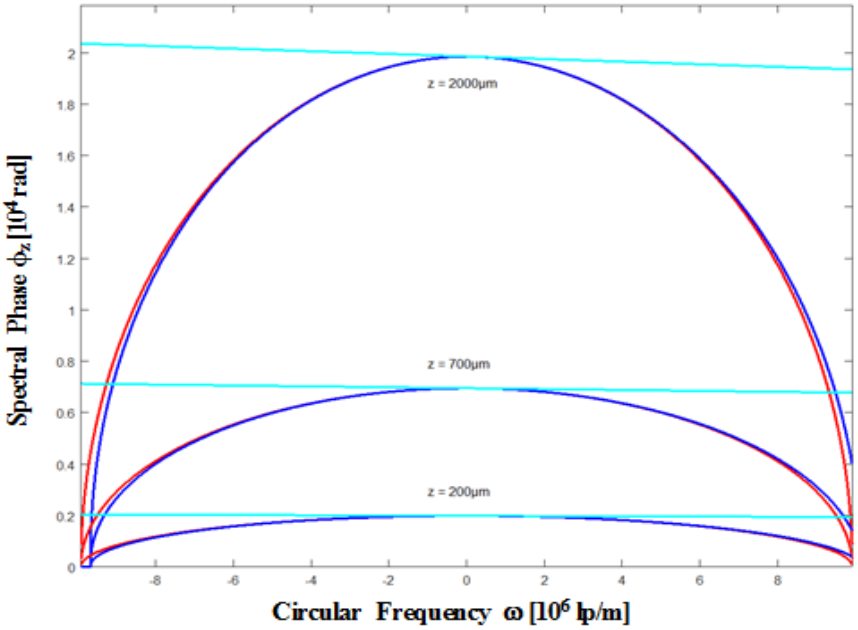

Fig.3.6 Evaluation example ($q_x = 1$) of the introduced linear approximation of the propagator phase ϕ_z for three z positions behind the grating propagator phase, absolute (red), approximated (blue).

The simulation of our example shows that the peak-to-valley deviation between the standard propagation function and the linearly approximated one is at a propagation distance of 200µm less than 0,2mrad, while the absolute phase value at the shifted spectral position exceeds 1800rad. This means a relative deviation of less than 0,00001%.

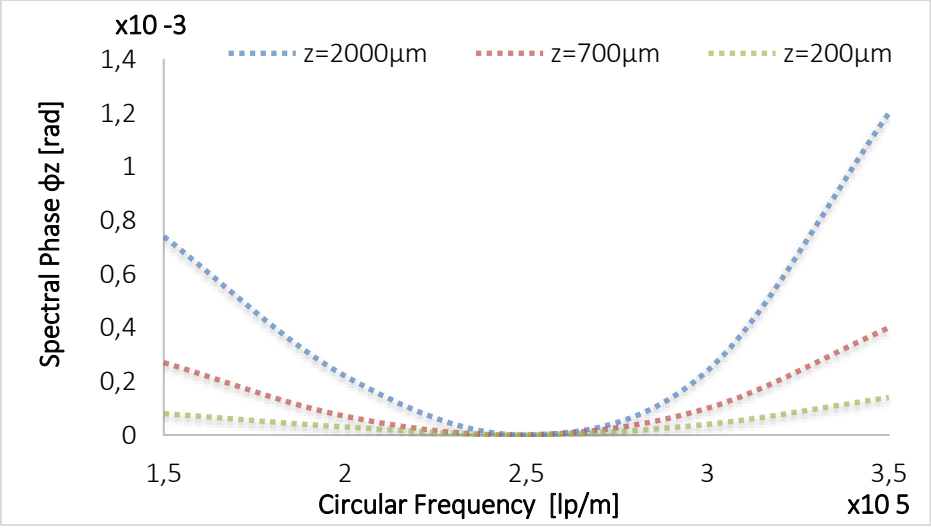

Fig.3.7 Difference between the used approximation and the real phase propagator: Difference in zoomed region of $\Delta\omega_x$ around ω_{x0} at positions z of 200, 700 and 2000µm.

For more investigations, the approximations for three different grating periods at different distances behind the gratings are simulated. The results are shown in Fig.3.8. The distance to the Talbot length which corresponds to grating periods of 25µm, 35µm and 45µm to 1975µm, 3870µm and 6398µm, respectively is normalized. An increase of the deviation is registered when the grating period is reduced However, the maximum resulting phase deviation for all gratings is less than 1,6 mrad.
The deviation between the ideal phase and the under approximation is very small and can be neglected. This shows that the approximation can be used for next step of the theory of gradient extraction.

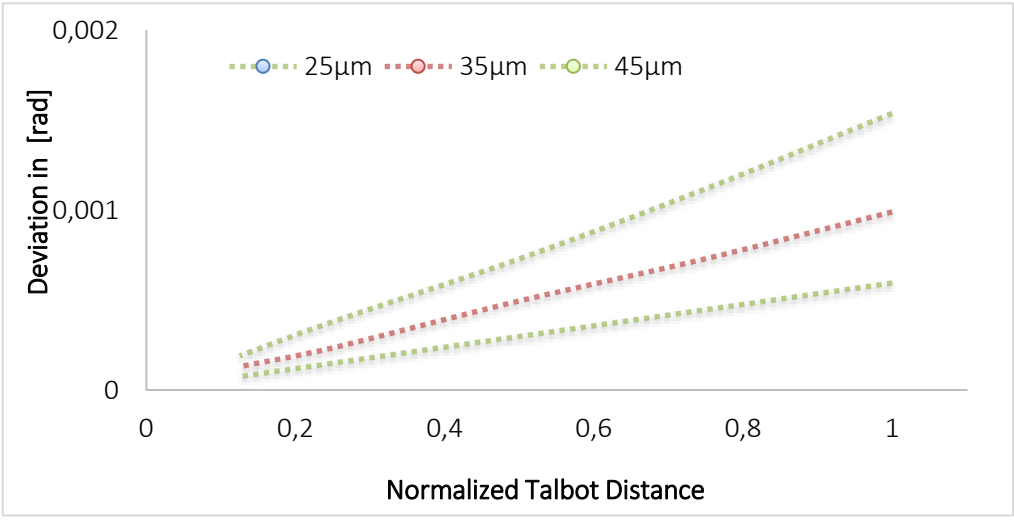

Fig.3.8 Illustration of the deviation between the actual propagation phase and the presented linear approximation at different distances behind the grating.

The spectrum of the transfer function of the cross grating as a two-dimensional sum of spectral orders is as follows

$$\tilde{\tau}(\omega_x, \omega_y) = \sum_{q_y=-N}^{+N} \sum_{q_x=-M}^{+M} \mathrm{sinc}(2q_x, 2q_y) \cdot \delta(\omega_x - q_x\omega_{x0}, \omega_y - q_y\omega_{y0}) \tag{3.11}$$

The indices of q_x, and q_y stand for the number of the spectral order (replica) in ω_x and $\omega_y$directions, respectively. The spectrum of the propagated signal after the grating $\tilde{S}_C(\omega_x, \omega_y)$ equals to the convolution of the initial signal spectrum and the grating transfer function followed by multiplication with the propagator as shown in Eq. (3.12).

$$\begin{aligned}\tilde{S}_C(\omega_x, \omega_y) &= \tilde{S}(\omega_x, \omega_y) \otimes \tilde{\tau}(\omega_x, \omega_y) \cdot \tilde{P}_z(\omega_x, \omega_y) = \tilde{\tau}(\omega_x, \omega_y) \otimes \tilde{S}(\omega_x, \omega_y) \cdot \tilde{P}_z(\omega_x, \omega_y) \\ &= \tilde{\tau}(\omega_x, \omega_y) \otimes \tilde{S}_z(\omega_x, \omega_y)\end{aligned} \tag{3.12}$$

where $\tilde{S}_z(\omega_x, \omega_y) = \tilde{S}(\omega_x, \omega_y) \cdot \tilde{P}_z(\omega_x, \omega_y)$

Now, the Spectrum of the propagated signal is reformulated as follows:

$$\begin{aligned}\tilde{S}_C(\omega_x,\omega_y) = & \sum_{q_y=-N}^{+N}\sum_{q_x=-M}^{+M}\tilde{S}_0(\omega_x - q_x\omega_{x0}, \omega_y - q_y\omega_{y0}) \\ & \cdot \exp\left(i\, z\left[\sqrt{k^2-(\omega_x - q_x\omega_{x0})^2-\left(\omega_y - q_y\omega_{y0}\right)^2}\right.\right. \\ & \left.\left. + \sqrt{k^2-(q_x\omega_{x0})^2-\left(q_y\omega_{y0}\right)^2} - \frac{(q_x\omega_{x0}, q_y\omega_{y0})\cdot\omega(\omega_x,\omega_y)}{\sqrt{k^2-(q_x\omega_{x0})^2-\left(q_y\omega_{x0}\right)^2}}\right]\right) \\ = & \sum_{q_y=-N}^{+N}\sum_{q_x=-M}^{+M}\tilde{S}_{z0}(\Delta\omega_x,\Delta\omega_y)\otimes\delta(\omega_x - q_x\omega_{x0}, \omega_y - q_y\omega_{y0}) \\ & \cdot \exp\left(iz\sqrt{k^2-(q_x\omega_{x0})^2-\left(q_y\omega_{y0}\right)^2}\right) \\ & \cdot \exp\left(-iz\left[\frac{(q_x\omega_{x0}, q_y\omega_{y0})\cdot\omega(\omega_x,\omega_y)}{\sqrt{k^2-{\omega_{x0}}^2-{\omega_{y0}}^2}}\right]\right) \\ = & \sum_{q_y=-N}^{+N}\sum_{q_x=-M}^{+M}\tilde{S}_{z0}(\Delta\omega_x,\Delta\omega_y)\otimes\delta(\omega_x - q_x\omega_{x0}, \omega_y - q_y\omega_{y0}) \\ & \cdot \exp\left(i\left[\varphi_{zq}(q_x\omega_{x0}, q_y\omega_{y0}) + \varphi_t(q_x\omega_{x0}, q_y\omega_{y0})(\omega_x+\omega_y)\right]\right)\end{aligned} \tag{3.13}$$

The spectrum of $\tilde{S}_C(\omega_x,\omega_y)$ consists of $(2M+1)\times(2N+1)$ spectral replicas of $\tilde{S}_{z0}(\Delta\omega_x,\Delta\omega_y)$ spaced by the circular grating frequencies of ω_{xy}. Each replica is multiplied by a different phase depending on its order q_x, and q_y, represented by linear phase term and an offset.

The image sensor registers the intensity of the propagated wave. Its Fourier transform $\tilde{I}_C(\omega_x,\omega_y)$ is expressed by the convolution of their complex spectral amplitude with its conjugate Eq. (3.14):

$$\begin{aligned}\tilde{I}_C(\omega_x,\omega_y) &= \tilde{S}_C(\omega_x,\omega_y)\otimes\tilde{S}_C^*(-\omega_x,-\omega_y) \\ &= \tilde{\tau}(\omega_x,\omega_y)\otimes\tilde{S}_{z0}(\Delta\omega_x,\Delta\omega_y)\otimes\tilde{\tau}^*(-\omega_x,-\omega_y)\otimes\tilde{S}_{z0}^*(-\Delta\omega_x,-\Delta\omega_y) \\ &= \tilde{\tau}(\omega_x,\omega_y)\otimes\tilde{\tau}^*(-\omega_x,-\omega_y)\otimes\tilde{S}_{z0}(\Delta\omega_x,\Delta\omega_y)\otimes\tilde{S}_{z0}^*(-\Delta\omega_x,-\Delta\omega_y) \\ &= \sum_{q_y=-2N}^{+2N}\sum_{q_x=-2M}^{+2M}\tilde{I}_{qx,qy}(q_x\omega_{x0}, q_y\omega_y)\end{aligned} \tag{3.14}$$

Due to the convolution operation, each replica represents the same spectrum of the convolved signal $\tilde{S}_{z0}(\Delta\omega_x, \Delta\omega_y) \otimes \tilde{S}^*_{z0}(-\Delta\omega_x, -\Delta\omega_y)$ after the propagation. They only differ in its phase term. The replica of $q_x = 2, q_y = 0$, i.e., $\tilde{I}_{2,0}(2\omega_x, 0)$ is chosen for the further analysis

$$\tilde{I}_{2,0}(2\omega_{x0}, 0) = \frac{1}{16}\left\{\tilde{S}_c\left(\omega_x - \frac{2\pi}{d_x}, \omega_y\right) \cdot \exp\left(i\left[\varphi_t(\omega_{x0}, 0) \cdot \omega_x + \varphi_{zq}(\omega_{x0}, 0)\right]\right)\right\} \otimes \left\{\tilde{S}^*_c\left(-\omega_x + \frac{2\pi}{d_x}, -\omega_y\right) \cdot \exp\left(i\left[-\varphi_t(-\omega_{x0}, 0) \cdot \omega_x + \varphi_{zq}(-\omega_{x0}, 0)\right]\right)\right\}$$

(3.15)

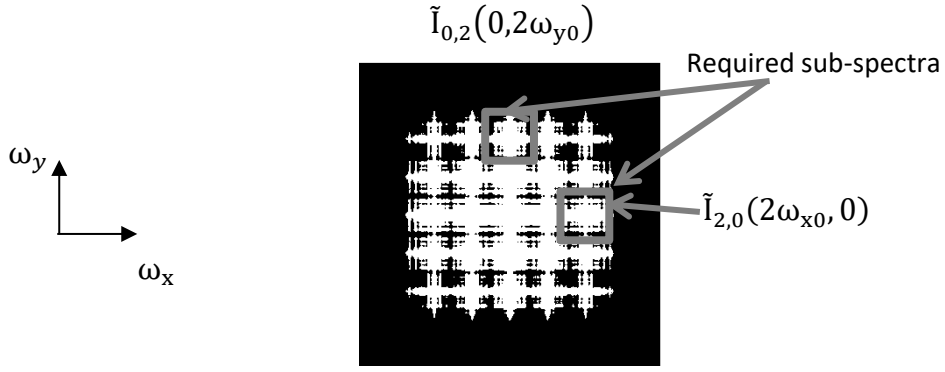

Fig.3.9 Illustration of the spectrum of the intensity captured behind the grating.

Because $\varphi_{zq}(\omega_{x0}, 0) = \varphi_{zq}(-\omega_{x0}, 0)$, this constant phase term can be neglected. After filtering $\tilde{I}_{2,0}(2\omega_{x0}, 0)$, the latter is inversely transformed into the spatial domain to get then $I_{2,0}(x, y)$ as follows:

$$I_{2,0}(x, y) = \frac{1}{16}\left\{S_c(x, y) \exp\left(i\frac{2\pi}{d_x}x\right) \otimes \delta\left(\varphi_t(\omega_{x0}, 0)\right)\right\} \cdot \left\{S^*_c(x, y) \exp\left(i\frac{2\pi}{d_x}x\right) \otimes \delta\left(\varphi_t(-\omega_{x0}, 0)\right)\right\}$$

$$I_{2,0}(x, y) = \frac{1}{16}\left\{S_c(x, y) \exp\left(i\frac{2\pi}{d_x}x\right) \otimes \delta(\varphi_t)\right\} \cdot \left\{S^*_c(x, y) \exp\left(i\frac{2\pi}{d_x}x\right) \otimes \delta(-\varphi_t)\right\}$$

$$I_{2,0}(x, y) = \frac{1}{16}\left\{S_c(x - \varphi_t, y) \exp\left(i\frac{2\pi}{d_x}(x - \varphi_t)\right)\right\} \cdot \left\{S^*_c(x + \varphi_t, y) \exp\left(i\frac{2\pi}{d_x}(x + \varphi_t)\right)\right\}$$

$$I_{2,0}(x, y) = \frac{1}{16} S_c(x - \varphi_t, y) \cdot S^*_c(x + \varphi_t, y) \exp\left(i\frac{4\pi}{d_x}x\right)$$

(3.16)

The term $\exp\left(i\frac{4\pi}{d_x}x\right)$ corresponds to a multiplication by harmonic oscillation of twice the grating frequency $2\omega_{x0} = 4\pi/d_x$ in x and does not contain any information about the wavefront. It can be eliminated either in spectral domain by shifting the spectral replica of $\tilde{I}_{2,0}(2\omega_{x0}, 0)$ to the origin or by demodulation in spatial domain (Eq. 3.17) [30].

$$I_{2,0}(x,y) = \frac{1}{16} S_c(x-\varphi_t, y) \cdot S_c^*(x+\varphi_t, y) \tag{3.17}$$

Since $S_{c(x,y)}$ is complex, i.e. $S_{c(x,y)} = A(x,y) \cdot \exp(i\varphi(x,y))$, the previous equation is expressed by Eq.(3.18):

$$I_{2,0}(x,y) = \frac{1}{16} A(x-\varphi_t, y) \cdot A(x+\varphi_t, y) \cdot \exp(i[\varphi(x-\varphi_t, y) - \varphi(x+\varphi_t, y)]) \tag{3.18}$$

The argument of $I_{2,0}(x,y)$ corresponds to:

$$\Delta\varphi_x(x,y) = \varphi(x-\varphi_t, y) - \varphi(x+\varphi_t, y) = \arg(I_{2,0}(x,y)) \tag{3.19}$$

The gradient in x direction can be derived from the differential quotient

$$\frac{\delta\varphi(x,y)}{\delta x} = \lim_{\varphi_t \to 0} \frac{\varphi(x-\varphi_t, y) - \varphi(x+\varphi_t, y)}{2\varphi_t} \approx -\frac{\sqrt{d_x^2 - \lambda^2}}{2z\lambda} \arg(I_{2,0}(x,y)) \tag{3.20}$$

The derivation of the gradient in y direction based on the spectral replica is as follows

$$\frac{\delta\varphi(x,y)}{\delta y} = \lim_{\varphi_t \to 0} \frac{\varphi(x, y-\varphi_t) - \varphi(x, y+\varphi_t)}{2\varphi_t} \approx -\frac{\sqrt{d_y^2 - \lambda^2}}{2z\lambda} \arg(I_{0,2}(x,y)) \tag{3.21}$$

The approximation of the difference quotient requires a small value of φ_t. Fig.3.10 shows schematically the reason of this approximation.

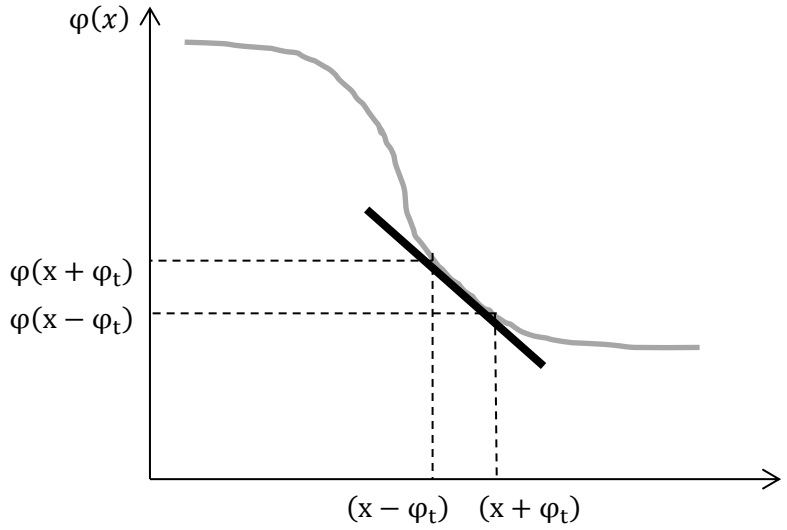

Fig.3.10 Schematic linear approximation of the difference quotient (black) referred to the phase (gray).

Indeed, this criterion is fulfilled by working at small propagation distances using smaller wavelengths and bigger grating periods. Fig.3.11 shows this dependency. The diagram demonstrates that the φ_t function near the grating is less than a micron. Therefore, this approximation might be considered as good. The influence of this approximation on the quality of the reconstruction is discussed more intensively in the simulation section.

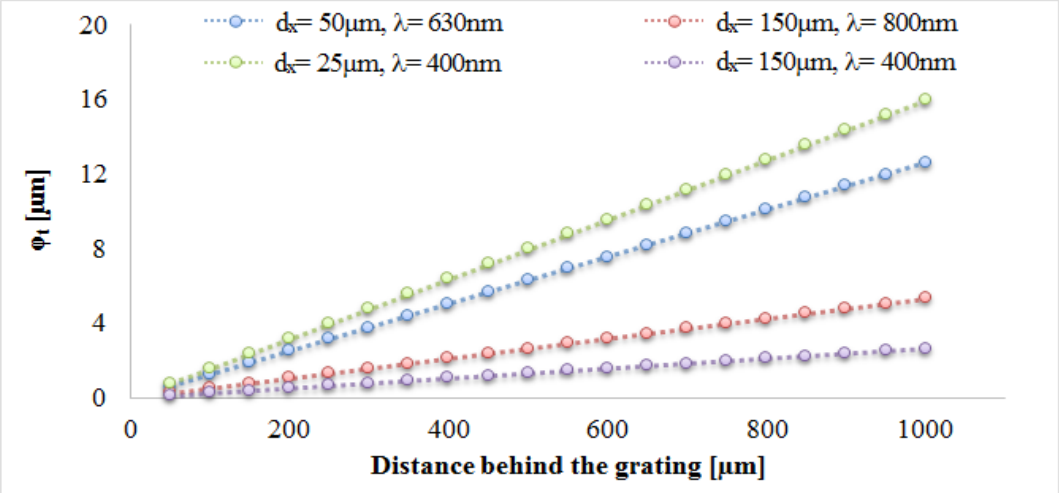

Fig.3.11 φ_t depending on the distance to the grating for different grating periods and wavelengths.

The goal of this dissertation is the characterization and the reconstruction of freeform surfaces full wavefront. After the extraction of the wavefront gradients, the full wavefront can be reconverted from the gradient by a 2D integration. For the integration in the present work, the Frankot & Chellappa integration method is used [146].

3.2 Enhancement of signal-to-noise ratio using spatial filtering

In the theory of the modified Talbot wavefront sensor, it has been shown that only a few of the spectral replica of the intensity Fourier transform is required to reconstruct the wavefront gradients. A major challenge is to separate the appropriate replica properly, with the least numerical processing to increase the signal-to-noise ratio. Until now, it has been assumed that the image sensor is positioned directly at the position z close to the grating. Due to the housing of the CCD sensors, it is not possible to place it close to the grating. To avoid this challenge, a 4f imaging system has been introduced as shown in Figure 3.12. After the diffractive grating, the wavefront propagates through the telescopic 4f system. The distribution in the focal planes of the 1st (rear) as well as the 2nd (front) lens relates to the wavefront by a Fourier transform. This relation is exploited to introduce spectral filters of specific geometries, so that only specific spectral parts of our signal pass the optics. Using this imaging system, the signal-to-noise ratio can be increased by making the separation of the sub spectra easy.

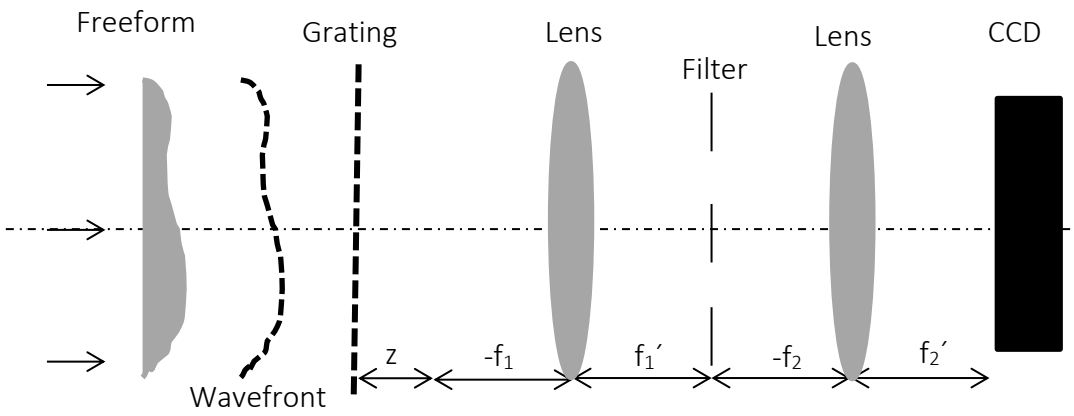

Fig.3.12 The schematic of the proposed wave front sensor with spatial filter.

In fact, the spatial filter blocks the undesired light. It is installed in the corresponding Fourier plane of a 4f optical system. The diffraction orders are divided into the angular spectrum following the grating equation:

$$\sin(\theta) = \frac{q\lambda}{d} \tag{3.22}$$

with θ as the diffraction angle, λ the wavelength, q the integer number of diffraction order and d the grating period. In the Fourier plane the diffraction orders are laterally positioned at ρ by:

$$\rho = f \cdot \tan(\theta) \tag{3.23}$$

The angular bandwidth of each spectral replica of the signal has to be limited to prevent aliasing. For small values of θ we set $\sin(\theta) \approx \tan(\theta)$ and define the lateral interval of a desired filter structure which is given by:

$$\left(q - \frac{1}{2}\right)\frac{\lambda f}{d} \leq q\frac{\lambda f}{d} \leq \left(q + \frac{1}{2}\right)\frac{\lambda f}{d} \tag{3.24}$$

Indeed, neglecting the remaining replica makes the following analysis easier. A $(2M+1) \times (2N+1)$ matrix of replica coefficients $A_{qy,qx}$ is introduced at the Fourier plane of the first lens of the 4f system to implement this spectral filtering into the spectrum of the cross grating transfer function Eq.(3.25):

$$\tilde{\tau}_f(\omega_x, \omega_y) = \sum_{q_y=-N}^{+N} \sum_{q_x=-M}^{+M} A_{qy,qx} \cdot \mathrm{sinc}(2q_x, 2q_y) \cdot \delta(\omega_x - q_x\omega_{x0}, \omega_y - q_y\omega_{y0}) \tag{3.25}$$

Note that the first matrix element is addressed in the first row and the first column as the position (q_y = -1, q_x = -1) and for the first row and the second column as (q_y = -1, q_x = 0) and so on.

In order to obtain the spectrum of the captured intensity at the camera plane, $\tilde{\tau}_f \otimes \tilde{\tau}_f^*$ has to be convolved:

$$\tilde{\tau}_f(\omega_x, \omega_y) \otimes \tilde{\tau}_f^*(-\omega_x, -\omega_y) = \sum_{q_y=-2}^{+2} \sum_{q_x=-2}^{+2} \mathrm{sinc}^2(2,2) \cdot B_{qy,qx} \cdot \delta(\omega_x - q_x\omega_{x0}, \omega_y - q_y\omega_{y0}) \tag{3.26}$$

$B_{f\,qy,qx}$ is the new coefficient matrix:

$$B_{f\,qy,qx} = A_{f\,qy,qx} \otimes A^*_{f\,qy,qx} \tag{3.27}$$

Previously, the need of extraction of determined replica in the spectral domain was demonstrated. Apparently, it should be sufficient to block the unused replica by an appropriate spatial filter. Now, it is demonstrated that it is worth to further discuss the application of different positions/arrangements of spatial filter structures in order to improve the selection of needed replicas corresponding to the description above. There, it is only needed to consider the processing of the 0 and ±1st as well as its mixed replica orders. First, a spatial filter is needed that allows all these replicas to pass.

3.2.1 All replicas of 0 and ±1st order pass the spatial filter

The contribution of the spatial filter structure as a part of the transfer function $\tilde{\tau}_f(\omega_x, \omega_y)$ is expressed in Eq.3.25 by the factor of $A_{f\,qy,qx}$. The necessary convolution (The camera only captures the intensity distribution) results in a spectral distribution of replicas following the coefficients of $B_{f\,qy,qx}$. It is sufficient to consider the behavior of matrix arrangements of $A_{fqy,qx}$ related to the result of $B_{f\,qy,qx}$ after the convolution. Furthermore, the bandwidth of spatial frequencies of our signal is assumed to be reduced, so that the overlapping of subsequent replicas is significantly decreasing. Such a spatial filter is expressed by:

$$A_{f\,qy,qx} = \frac{1}{9}\begin{pmatrix} 1 & 1 & 1 \\ 1 & 1 & 1 \\ 1 & 1 & 1 \end{pmatrix} \tag{3.28}$$

The index value of "1" stands for a passing and the "0" for a blocked spectral order. The position of indices for the integer replica order is starting with an index pair of $[q_x,q_y] = [-1,-1]$ at the upper left matrix position. The normalization constant of 1/9 sets the entire energy content to 1 as a reference. The spectral convolution yields the intensity transfer function $B_{f\,qx,,qy}$ as:

$$B_{f\,qy,qx} = A_{f\,qy,qx} \otimes A^*_{f\,qy,qx} = \frac{1}{81}\begin{pmatrix} 1 & 2 & 3 & 2 & 1 \\ 2 & 4 & 6 & 4 & 2 \\ 3 & 6 & 9 & 6 & 3 \\ 2 & 4 & 6 & 4 & 2 \\ 1 & 2 & 3 & 2 & 1 \end{pmatrix} \tag{3.29}$$

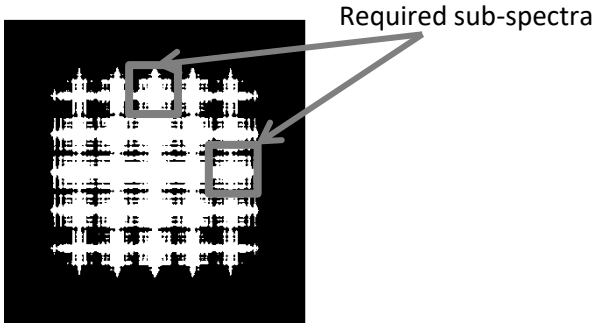

Fig.3.13 Illustration of the intensity spectrum captured behind the grating passing all replicas (0^{th}, $\pm1^{st}$ and their mixed orders) in Fourier domain.

In this case there appear 25 spectral replicas in Fourier domain. The energy of the sub-spectra of our interest is 3/81 related to the total power which passes the filter. Each of these sub-spectra is surrounded by five other sub-spectra (Fig.3.13). Two adjacent sub-spectra have 2/81 of the total energy. Another two sub-spectra have 4/81 of the total energy and a direct neighbor contains 6/81 of the total energy. This situation is dangerous for the overlapping of numerous and stronger neighbor replicas.

3.2.2 Suppressing of determined replica

We consider now the case of blocking of replica orders as suggested in the following Eq.3.30:

$$\mathrm{A_{f\,qy,qx}} = \frac{1}{9}\begin{pmatrix} 0 & 1 & 0 \\ 1 & 0 & 1 \\ 0 & 1 & 0 \end{pmatrix} \tag{3.30}$$

With the filtering, the intensity transfer function $B_{f\,qx,,qy}$ changes to:

$$\mathrm{B_{f\,qy,qx}} = \mathrm{A_{f\,qy,qx}} \otimes \mathrm{A^{*}_{f\,qy,qx}} = \frac{1}{81}\begin{pmatrix} 0 & 0 & 1 & 0 & 0 \\ 0 & 2 & 0 & 2 & 0 \\ 1 & 0 & 4 & 0 & 1 \\ 0 & 2 & 0 & 2 & 0 \\ 0 & 0 & 1 & 0 & 0 \end{pmatrix} \tag{3.31}$$

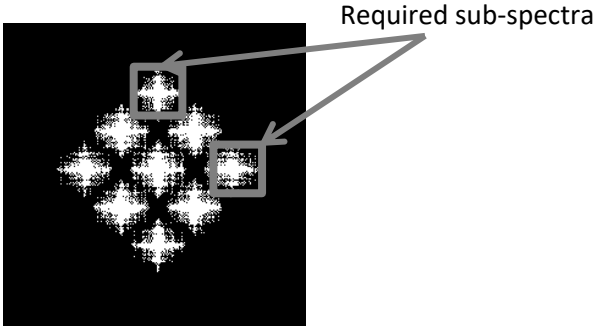

Fig.3.14 Illustration of the intensity spectrum captured behind the grating with suppression of some replicas following Eq.3.30.

This suppression of replicas results in a convenient distribution in Fourier plane. Some replicas do not appear anymore. Indeed, instead of 25 replicas we only register 9. This gives more space for the remaining spectral orders, the tendency of interferences decreases significantly. There are only two close neighbors near our replica of interest. In comparison to the previous case, the signal to noise ratio of our desired replica is increased. Additionally, it is also possible to improve the lateral resolution. This is described later in section 3.3.2.1. Of course, the energy of our needed replica is reduced to 1/81 compared to 4/81 of the previous scenario. However, this can be compensated by increasing the exposure time of the camera.

3.2.3 Alternative spatial filter

An alternative spatial filter arrangement is written in Eq.3.32:

$$\mathrm{A_{f\,qy,qx}} = \frac{1}{9}\begin{pmatrix} 1 & 0 & 1 \\ 0 & 0 & 0 \\ 1 & 0 & 1 \end{pmatrix} \tag{3.32}$$

Now, the intensity transfer function $B_{f\ qx,qy}$ yields:

$$\mathrm{B_{f\,qy,qx}} = \mathrm{A_{f\,qy,qx}} \otimes \mathrm{A^{*}_{f\,qy,qx}} = \frac{1}{81}\begin{pmatrix} 1 & 0 & 2 & 0 & 1 \\ 0 & 0 & 0 & 0 & 0 \\ 2 & 0 & 4 & 0 & 2 \\ 0 & 0 & 0 & 0 & 0 \\ 1 & 0 & 2 & 0 & 1 \end{pmatrix} \tag{3.33}$$

The same advantages described in the previous paragraph are registered. Stronger replica of 2/81 instead of 1/81 are nevertheless obtained and the adjacent replicas are farther away from our required sub-spectra. This should be the best structure for our purpose. However, this spatial filter arrangement was not applied because of the post processing. There, the required replicas are calculated in order to get a phase gradient map, followed by an integration operation of Frankot and Chellappa algorithm. Due to the shifting theorem (lateral shift in spectral domain corresponds to phase shift in spatial domain), the replicas in the corners of the Fourier plane contain the information in xy- as well as in yx-directions. The revealed phase gradient map in spatial domain must be integrated along these skewed xy- and yx- directions based on a x- and y- cartesian coordinate system. This leads to a reduced number of sample points which can be taken into account (loss of information, reduction of resolution) and introduces additional errors (rotation operation, rounding errors, not equal integration intervals along all rows and columns). So, the spatial filter structure corresponding Eq.3.30 is preferred.

3.3 Theoretical analysis

In this Section, important theoretical properties of these methods are derived. The main theory uses only a binary grating and a CCD camera. Therefore, first the properties of this simple arrangement are analyzed. The use of a spatial filtering promises an increase in the signal-to-noise ratio, the lateral resolution and the dynamic range. This improvement is also explained later.

3.3.1 System without spatial filtering:

3.3.1.1 Lateral resolution

The lateral resolution is an important feature of any measurement method. The smallest measurable structure from the wavefront represents the lateral resolution. Due to the setup and the signal processing, some restrictions exist. The wavefront passes a sampling grating and the camera can only capture intensity distributions. The modulation behind the grating in spatial domain corresponds to a convolution between the signal spectrum ω_{sig} and the spectrum of the grating in the spectral domain $\omega_{xgrating}$. A binary grating generates an infinite train of Dirac pulses. Here we take only the $\pm 1^{st}$ and 0 replica into account. The spectrum of the intensity of this modulation is expressed by the convolution of the complex spectral amplitude of the modulation with its conjugate.
Due to this operation, the extent of the spectral domain is divided into 5 equal parts. Additionally, each individual signal spectrum ω_{sig} broadens to ω_{sub}. In order to prevent aliasing, the subspectra of the intensity must be clearly separated. From this follows that the maximum (convolved) spatial signal frequency ω_{sub} corresponding to the smallest measurable structure can only be half the distance between the subspectra ω_{xmax}. This corresponds to the spatial grating frequency $\omega_{grating}$. This means for the general case (without spatial filtering) that the spectral width of the smallest lateral resolution of the signal is 10 times smaller than the whole spectral domain of the used cameras. Back transformed to spatial domain, this corresponds to a structure resolution of 10 spatial pixel size of the camera. Alternatively, one could improve the resolution with a multi camera setup and an appropriate optical configuration. Fig.3.15 shows the dependence of the lateral resolution on the pixel size.

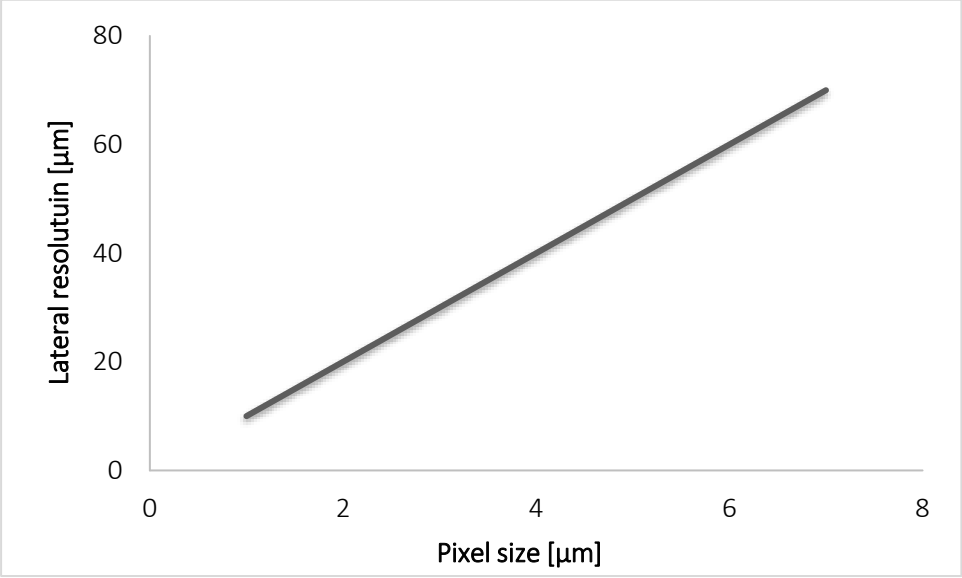

Fig.3.15 Lateral resolution vs Pixel size.

3.3.1.2 Angular step width

The angular step width represents the precision of the wavefront measurement and corresponds to the smallest possible measurable slope of the wavefront. This bandwidth relates inversely to the size of the camera pixel (Fig.3.16). Furthermore, the Nyquist criterion has to be obeyed in order to be able to reconstruct the signal without artefacts. The maximum spatial frequency along one dimension of the used camera can be calculated as follows:

$$\omega_{max} = \frac{2\pi}{2a_x} = \frac{\pi}{a_x} \tag{3.33}$$

With ω_{max} the maximum spatial frequency, λ the wavelength and a_x the pixel size.

$$\theta_{max} = 2 * \sin^{-1}\left(\frac{\lambda}{g_{cam}}\right) \approx \frac{2*\lambda}{g_{cam}} \approx \frac{\lambda}{a_x} \tag{3.34}$$

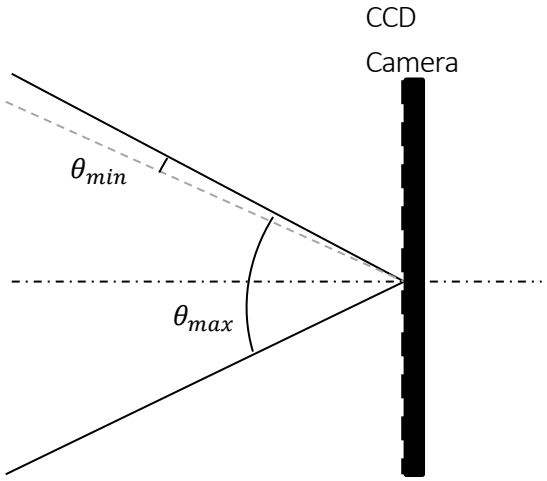

Fig.3.16 Angular step width of camera grating structure. The smallest period (twice pixel pitch a_x) causes the angular range of θ_{max}, the extent (number of spatial replica of periods) the smallest resolvable angle θ_{min}.

Indeed, the smallest (basic) frequency of the grating is:

$$\omega_{min} = \frac{2\pi}{Ma_x} = \frac{2\omega_{max}}{M} \tag{3.35}$$

Besides, the smallest angular step width can be calculated by dividing the maximum acceptance angle of the camera by the number of camera pixels.

$$\theta_{min} = \mathrm{asin}(\frac{\omega_{min}}{k}) \approx \frac{\lambda}{Ma_x} \tag{3.36}$$

Thereafter, a graphical representation of some values of angular resolution depending wave length and camera pixel size is reported in Fig3.17.

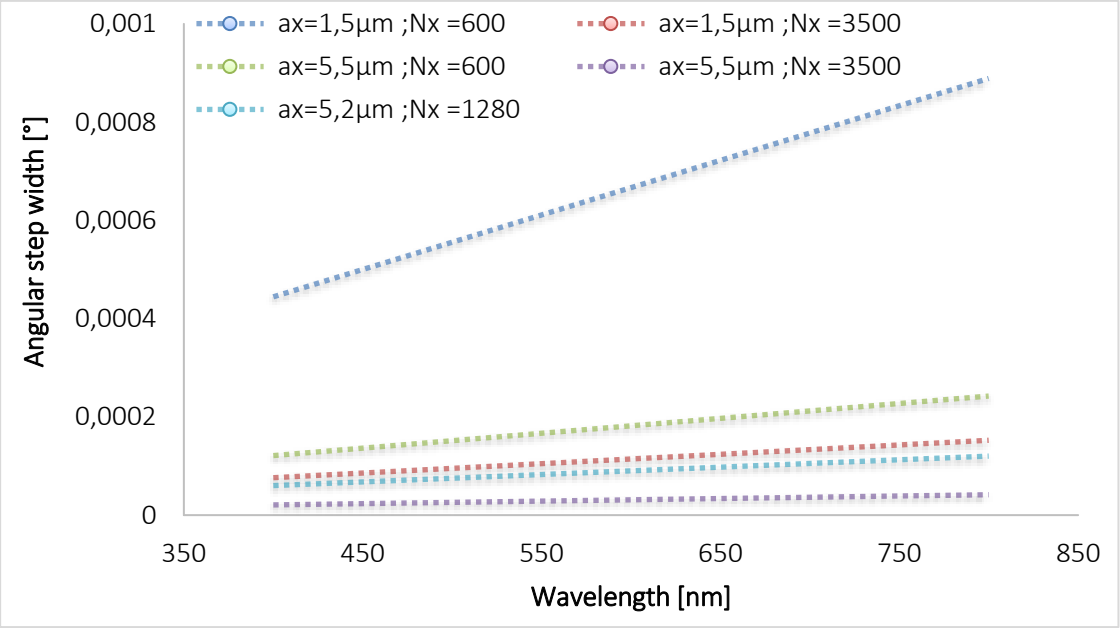

Fig.3.17 Angular step width vs. wavelength at different parameters of pixel pitch a_x and number of pixels N_x

3.3.1.3 Dynamic range

As a dynamic range, it is referred to a range within the slope of the measured electromagnetic wavefront, which can be varied in order to perform reliable reconstruction using a measuring method. Measurements above the dynamic range can lead to errors such as aliasing. The latter can cause disturbing artefacts in the retrieved object signal. The dynamic range refers to the maximum possible spectral extent of the measured signal. In addition, the dynamic range is defined as minimum and maximum angles that are equal in magnitude and differ in sign. In other words, the limits of the measured angular range are symmetrically relative to the plane object wave propagating along the optical axis of the system. The dimension of the outer orders in the spectrum of the recorded intensity need to be kept within 1/5th of the entire spectral range of the camera. The extension of these orders is a doubled spectral expansion of the measured object signal, which causes a limitation of the spectral extension of the object signal to 1/10th of the spectral camera range. As it can be seen, the dynamic range depends on the spectrum of the bandwidth of spatial frequencies accepted by the camera. The maximum bandwidth of spatial frequencies accepted by the camera is shown in equation (3.36). It means that the maximum dynamic range can be described as follows

$$\alpha_{max} = \arcsin\left(\frac{\omega_{max}}{5k}\right) = \arcsin\left(\frac{\lambda\pi}{5\cdot 2\pi a_x}\right) = \arcsin\left(\frac{\lambda}{10a_x}\right) \qquad (3.36)$$

Fig.3.18 displays the dependency of the Dynamic range on the wavelength and the pixel size of camera.

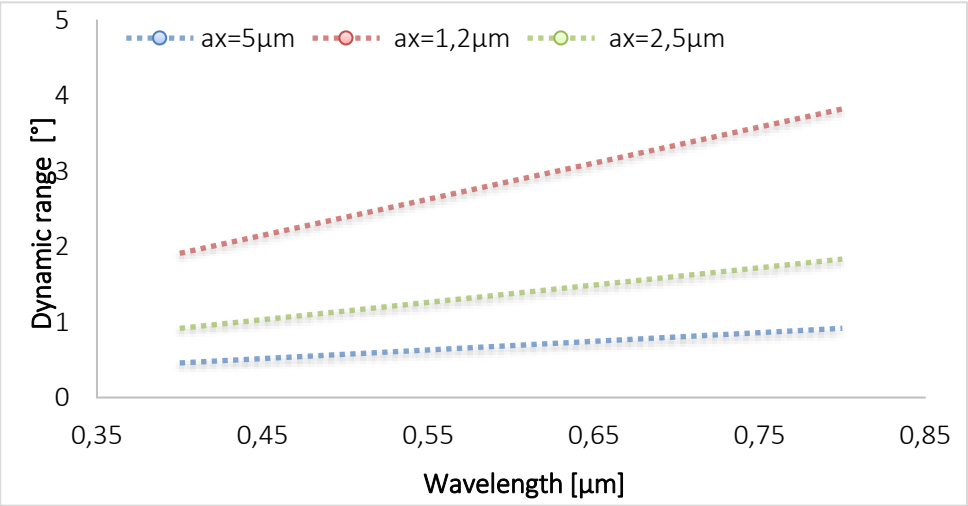

Fig.3.18 Dynamic range of the camera depending on the wavelength and camera pixel size.

3.3.2 System with spatial filtering

3.3.2.1 Lateral resolution

The application of a spatial filter in Fourier plane behind the grating causes an increase of the maximum signal frequency without causing any possible aliasing effect. When the spatial filter is used as mentioned in the previous section 3.2.2, replica can be blocked following the Eq. 3.30. The missing replica offers additional space which allows the expansion of the remaining replica. Applying the proposed filtering following Eq. 3.30 results in the transmission of only 3 spectral replicas instead of 5 along one coordinate. It means that the highest spatial frequency can be increased to 1/6 of the total spectrum. Therefore, the smallest resolvable structure based on the presented measuring methods can be reduced from 10 to 6 camera pixels by spatial filtering. In Fig 3.19 a comparison of achievable lateral resolution without and with spatial filtering is presented.

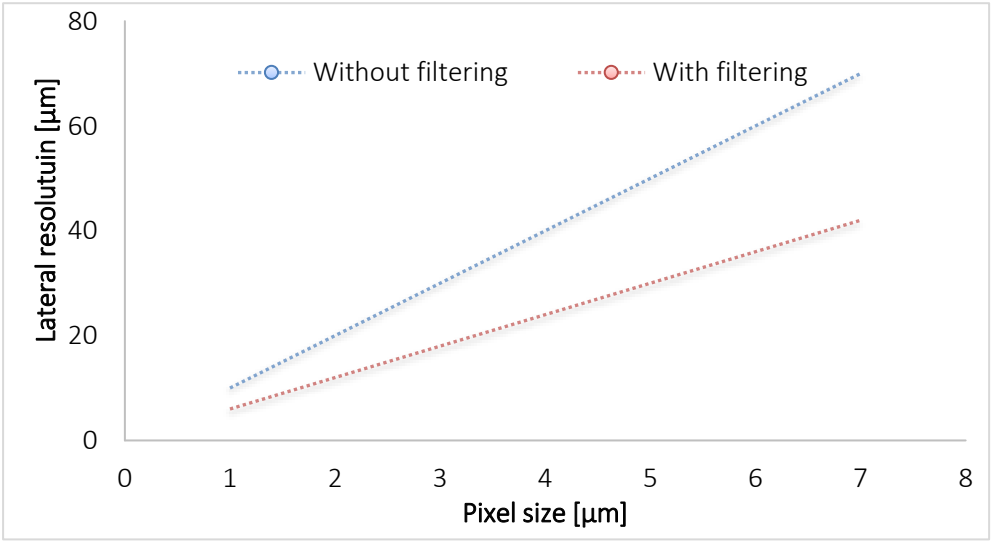

Fig. 3.19 Comparison of the achievable lateral resolution without and with spatial filtering

3.3.2.2 Angular step width

It was shown in the previous section that the smallest possible measurable slope of the test wavefront depends only on the wavelength, the number and the size of the camera-pixel. This means that the filtering has no influence on the angular step width.

3.3.2.3 Dynamic range

By applying the filtering, the dynamic range of the method has increased. The maximum frequency of the tested signal, and therefore the large measurable gradient, is 1/6 of the bandwidth of spatial frequencies accepted by the camera. Fig.3.20 reports the dependency of the dynamic range in the case of spatial filtering on the wavelength and the camera pixel size.

$$\sin \alpha_{max} = \frac{\lambda}{6*a_x} \rightarrow \alpha_{max} = \arcsin \frac{\lambda}{6*a_x} \tag{3.37}$$

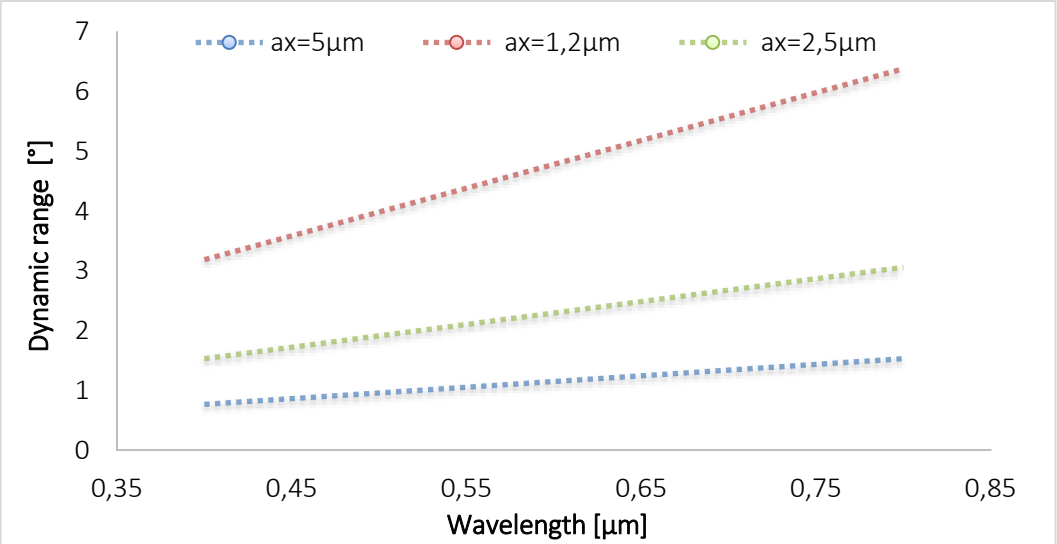

Fig.3.20 Dynamic range vs. wavelength for different size of camera pixel.

3.4 Extension of the theory for reflection application

The measurement methods based on optical non-contact principles, such as interferometry, deflectometry, etc. use the properties of light. The test object is illuminated with a well-defined electromagnetic wave and the reflected or transmitted light is recorded and analyzed. When measuring in reflection, new challenges arise. Components in the beam path block the illumination beam path. They cast a shadow over the object as shown in Fig.3.21.a. This challenge can be overcome in practice by using beam splitters or tilted illumination of the reflective test object as depicted in Fig.3.21.b. This leads to an increased complexity and size of the measuring devices. This section will serve to adapt the presented theory to be able to characterize surfaces in reflection as well as in transmission and to solve the challenge of other optical measuring methods.

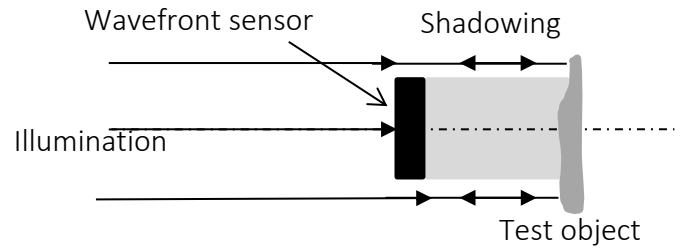

(a)

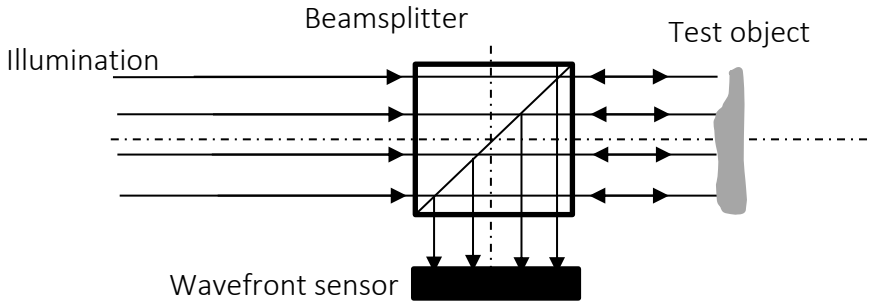

(b)

Fig.3.21 (a) Schematic representation of the challenge, (b) Conventional solution using beam splitter.

A non-requirement of the classic optical beam splitter should be a key feature of the measurement process, therefore all optical components are located on a common optical axis. This leads to a compact and stable measurement setup. As in the previous theory (transmission), a partially coherent monochromatic light source is used. The emitted light from an LED actually has an area of less than one square millimeter. This allows the construction of complex lighting systems of high quality in a small volume. Therefore, there is no problem to integrate a small LED into the existing test setup without much effort. The basic idea is divided into two parts. In the first part, the illumination path from the light source to the test object is described. The reflection path from the test object to the detector is shown in the second part.

3.4.1 Illumination path

The illumination and the measuring system should be on-axis. Therefore, the illumination concept is an important part of the presented idea. This illumination scheme is shown in Fig. 3.22. A partially coherent light source (LED), is positioned directly in front of a pinhole. The resulting component between the pinhole and the LED is considered as a point source. The latter is located in the object-side focal length of a collimating optical element. A two-dimensional amplitude cross grating is positioned at a distance L = f + s, where f is the focal length of this collimating optics and s is a small arbitrary distance (up to

several hundred microns). When passing through the grating, the light is diffracted into different diffraction orders.

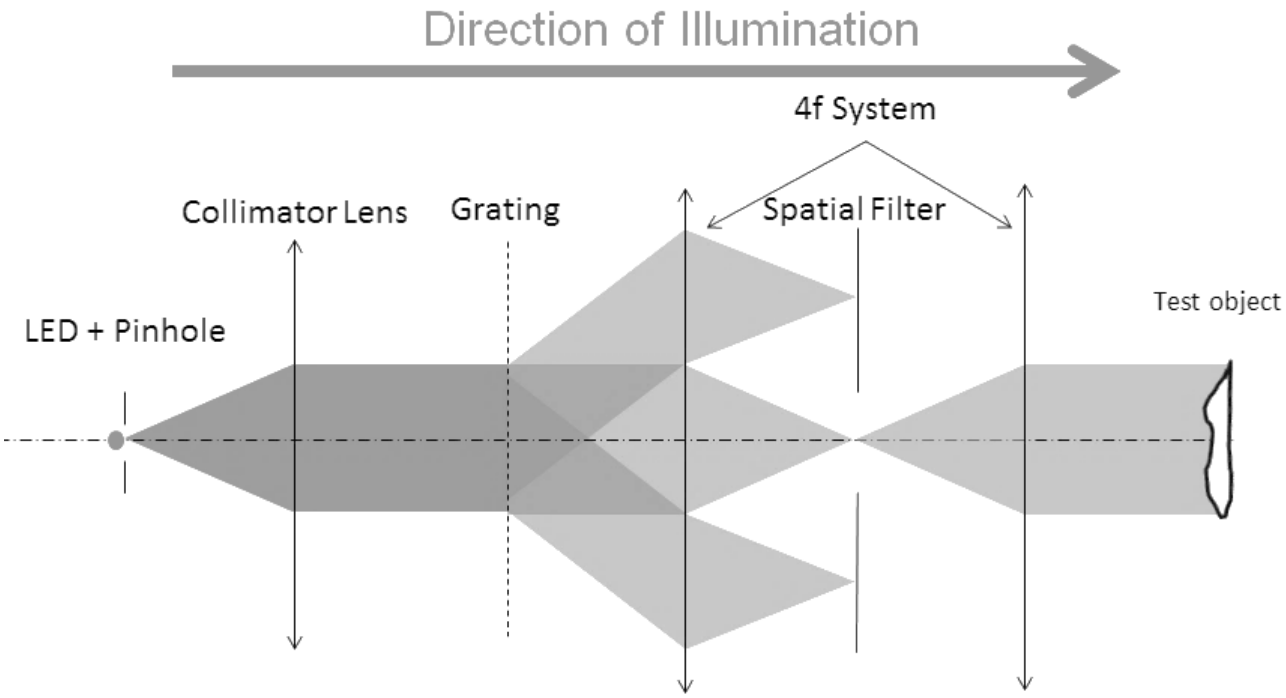

Fig. 3.22 Illumination path.

The amplitude cross grating, the LED, the pinhole and the collimator lens are used in one direction to perform the illumination of the test object. The cross grating is imaged onto the object to be characterized via a 4f imaging system. The latter consists of two optical lenses. In the corresponding Fourier plane of the 4f system, a spatial filter is aligned. This filter removes all diffraction orders caused by the grating from the beam path except the 0 order. This order serves as the origin of a collimated plane wave illuminating the object.

3.4.2 Signal path in reflection

The incident plane illumination wave is reflected at the reflective test object. The path of the reflected light to the recording sensor is shown schematically in Fig.3.23. The reflected light passes back through the 4f imaging system in the reverse direction. The spatial filter selects the maximum range of the angular spectrum of the test sample. This low-pass filtered light is diffracted at the grating. A second 4f system consisting of two collimated lenses is used to image a plane s behind the grating onto a CCD chip. The position of the Fourier plane of the second imaging system coincides with the illumination pinhole and an additional spatial filter component. Here the ± 1^{st} orders of diffraction, which carry the measurement signal, pass through the filter. The rest, especially the 0 order, is blocked. These ± 1^{st} diffraction orders reach the camera sensor. In summary, the reflective setup consists of a grating, two 4f imaging systems including optimized spatial filters separated by the small propagation distance of s and a recording sensor.

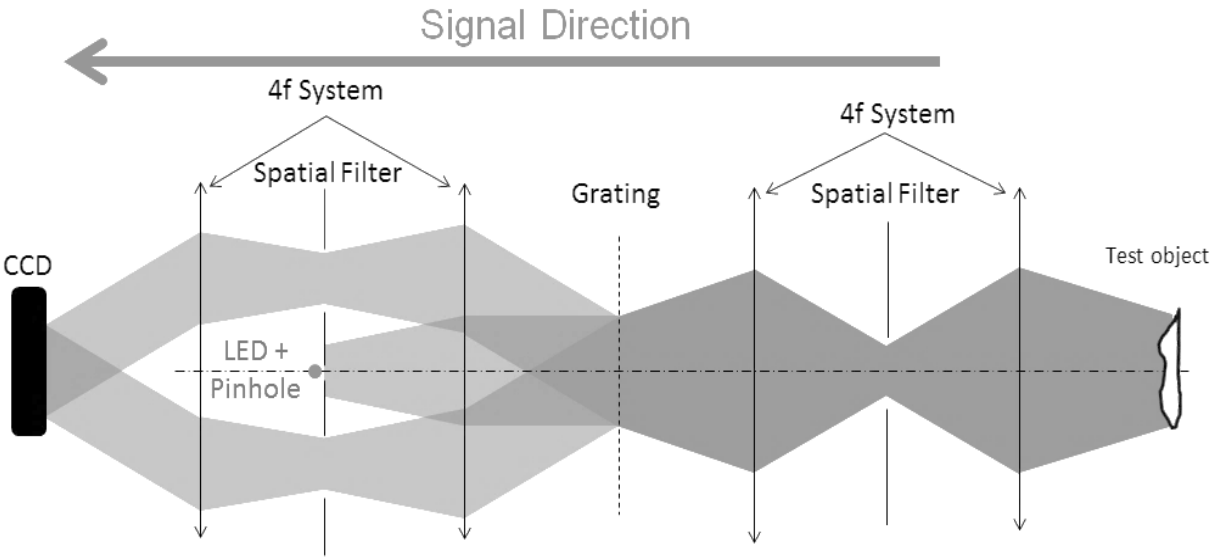

Fig.3.23 Reflection path.

3.4.3 System design

The presented measurement setup is based on a simple and robust experimental setup. However, there are various challenges that need to be explored in this measurement configuration. i) In order to collect enough light from the test object and to project it onto the camera; and ii) to optimize the information content in the measurement signal on the CCD sensor. For this analysis, we will focus on the energy content of the discrete diffraction orders q_x and q_y and represent the spectral transfer function of $\tilde{\tau}(\omega_x, \omega_y)$ as a decomposition of Fourier coefficients of:

$$\tilde{\tau}(q_x, q_y) = \frac{1}{4}\,\mathrm{sinc}\left(\frac{q_x}{2}, \frac{q_y}{2}\right) \tag{3.38}$$

The efficiency of each diffraction order $\eta(q_x,q_y)$ related to its total energy can be estimated as:

$$\eta(q_x, q_y) = \tilde{\tau}(q_x, q_y) \cdot \tilde{\tau}^*(q_x, q_y) = \left|\tilde{\tau}(q_x, q_y)\right|^2 \tag{3.39}$$

In Table 1 the contributions of various (0 and/or $\pm 1^{st}$) diffraction orders are listed for a duty cycle of (width/grating period) = ½ which is used in this work:

Table 3.1. Contributions of applied diffraction orders.

Diffraction order	η(0,0)	η(±1,0), η(0,±1)	η(±1,±1)
Contribution	6.25%	2.53%	1.03%

In this application a 2-dimensional analysis is performed. Due to the subsequent signal processing step described in the theory part of transmission, it is interesting to study the diffraction orders along the x- and y- axis, i.e. the four mixed orders of (±1,0) and (0,±1).

The properties for the experimental configuration will be presented in following.

As mentioned before, each of the optical components introduces light losses due to absorption, reflection (scattering), filtering and functional distribution (diffraction). Now, the energetic distribution of the light along the setup is considered.

The behavior of any optical component is given by 3 phenomena: absorption α, reflection ρ and transmission τ. The normalized balance is referred to by:

$$\alpha + \rho + \tau = 1 \tag{3.40}$$

Here, our focus is on the main influence due to the reflection at the amplitude grating (Fig.3.24).

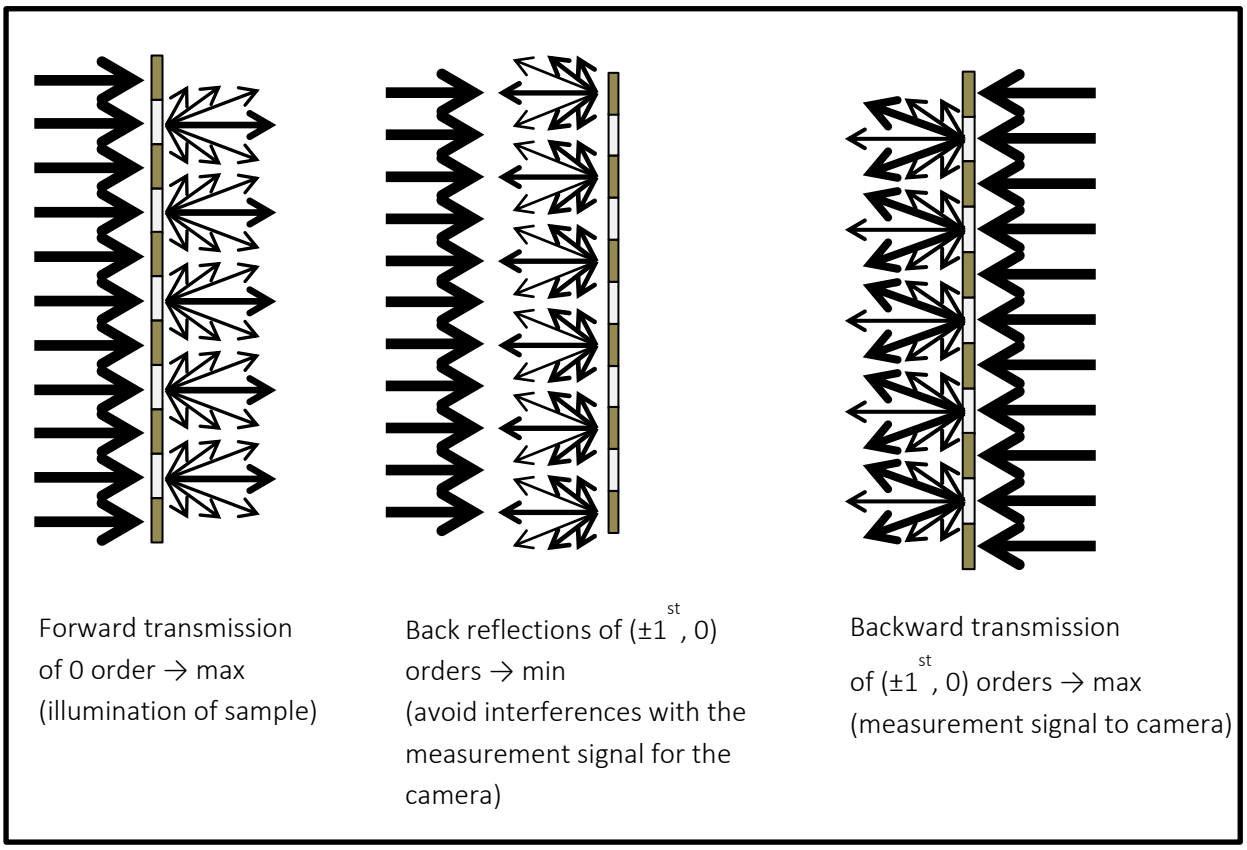

Fig.3.24 The behaviour in forward and backward illumination of an amplitude grating.

The amplitude grating is considered as a thin optical component realized on a glass substrate. The light passes this grating structure and is blocked at the spatially structured opaque layer. Those layers can be made of chromium or black silicon. The latter is a type of porous silicon materials consisting of nano pores or nanowires on a Si wafer surface. [147, 148] show as well a low reflectivity and correspondingly a high absorption of visible light, regardless of the incident light angle and wavelength [149, 150]. This results from the phenomena of reflection or absorption, i.e. $\alpha_{opaque} + \rho_{opaque} = 1$. With $\tau_{opaque} = 0$, on the transmissive (glass) structure, only reflection and transmission occur. Here we consider $\rho_{glass} + \tau_{glass} = 1$ with $\alpha_{glass} = 0$. Glass has a value of $\rho_{glass} \approx 0.04$ and $\tau_{glass} \approx 0.96$, for instance.

If the illumination is uniform and the light is collimated, the performance of the grating structure is estimated as:

$$(\rho_{\mathrm{opaque}} + \alpha_{\mathrm{opaque}}) \cdot \tfrac{1}{2} + (\rho_{\mathrm{glass}} + \tau_{\mathrm{glass}}) \cdot \tfrac{1}{2} = 1 \tag{3.41}$$

Due to the actual duty cycle of 1 : 2, the opaque material covers in summary 50% of the grating area. The transparent glass material affects the remaining part. Therefore, a weighting factor of ½ for opaque and glass structure is introduced. The grating structure splits the light into diffraction orders corresponding to the relationship of diffraction efficiencies of $\eta(q_x,q_y)$ as mentioned above:

$$\eta(q_x, q_y) = \left|\tilde{\tau}(q_x, q_y)\right|^2 = \left(\tfrac{1}{4}\,\mathrm{sinc}\left\{\tfrac{q_x}{2}, \tfrac{q_y}{2}\right\}\right)^2 \tag{3.42}$$

For our analysis, it is necessary to consider the behavior in forward and backwards directions. The forward transmission of the incident light can be estimated by:

$$\tau_{\mathrm{grating}}(q_x, q_y) = \tau_{\mathrm{glass}} \cdot \tfrac{1}{2} \cdot \eta(q_x, q_y) \tag{3.43}$$

Regarding the equation for the definition of the diffraction orders $\eta(q_x,q_y)$, the 0 order component $\tau_{grating}(0,0)$ serves as sample illumination:

$$\tau_{\mathrm{grating}}(0,0) = \tau_{\mathrm{glass}} \cdot \tfrac{1}{2} \cdot \eta(0,0) \tag{3.44}$$

Other orders are blocked by the spatial filter component. Now the behavior of disturbing reflected light components $\rho_{grating}$ of the ($\pm1^{st}$,0) orders is considered. They travel back from the grating to the camera sensor and interfere with the orders carrying the measurement information. 3 cases must be considered depending on the reflection of the transparent and non-transparent sections of the grating in order to estimate the back reflections:

- ✓ $\rho_{opaque} > \rho_{glass}$ (high back reflecting material, ~chromium, see cases (a) and (b) in Fig. 3.25)

$$\rho_{\mathrm{grating}}(q_x, q_y) = (\rho_{\mathrm{opaque}} - \rho_{\mathrm{glass}}) \cdot \tfrac{1}{2} \cdot \eta(q_x, q_y) \cdots \\ +\rho_{\mathrm{glass}} \cdot \frac{1}{2} \cdot \delta(q_x = 0, q_y = 0) \tag{3.45}$$

- ✓ $\rho_{opaque} = \rho_{glass}$ (no effect of the grid structure, see case (c) in Fig. 3.25)

- ✓ $\rho_{opaque} < \rho_{glass}$ (high absorption media, ~black silicon, see case (d) in Fig. 3.25)

$$\rho_{\mathrm{grating}}(q_x, q_y) = (\rho_{\mathrm{glass}} - \rho_{\mathrm{opaque}}) \cdot \tfrac{1}{2} \cdot \eta(q_x, q_y) \cdots \\ +\rho_{\mathrm{opaque}} \cdot \frac{1}{2} \cdot \delta(q_x = 0, q_y = 0) \tag{3.46}$$

The dirac pulse expresses the appearance of the 0-diffraction order. All the 4 diffraction orders (~ replicas in the angular spectrum) should be taken into account.

Fig. 3.26 illustrates the grating performance depending on the absorption of the light blocking grating material. It should be noted that for $\rho_{opaque} = \rho_{glass}$ or $(1 - \alpha_{opaque}) = \rho_{glass}$, the characteristics of the grating disappear. This would be the best option to completely avoid the back reflections overlapping with the signal diffraction orders. The actual relationship between the back reflections due to the opaque material and the transmitted signal (of a fully reflecting flat mirror as sample) is illustrated in Fig.3.26.

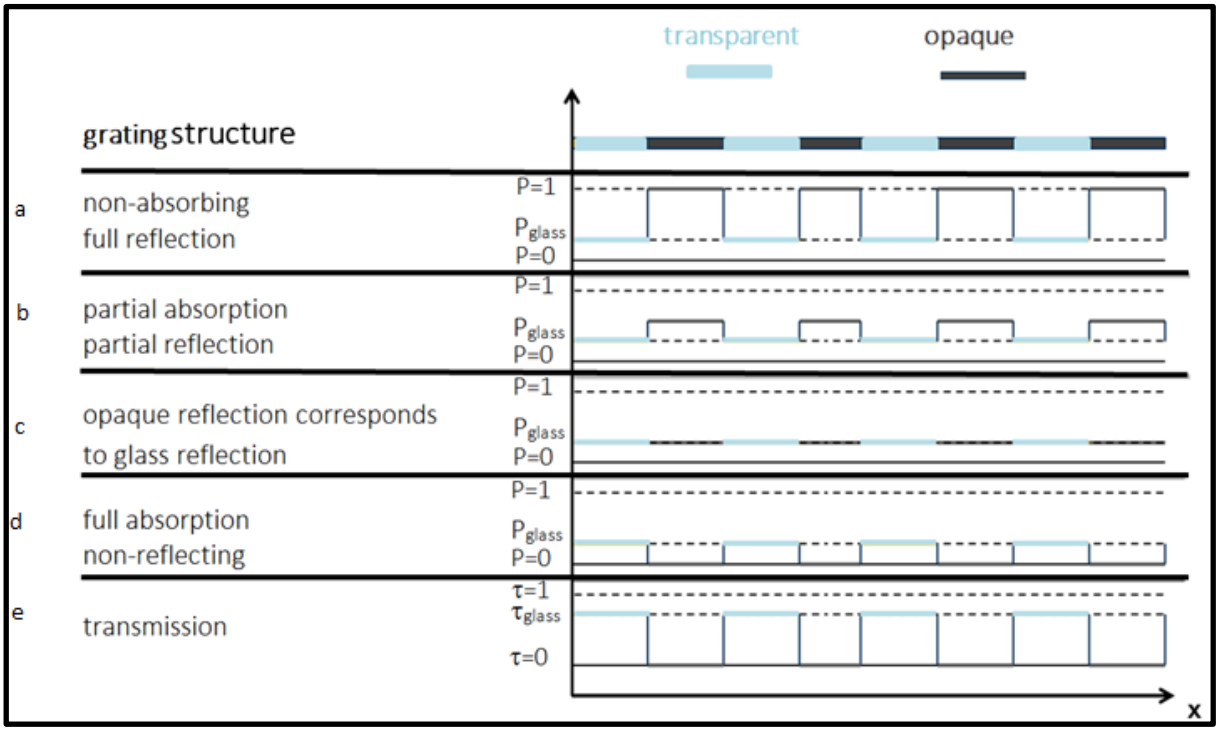

Fig.3.25 Grating functionality versus absorption (or back reflection) property of the grating material. The appearance of the changes depending on the absorption/reflection of the opaque media is illustrated as follows: (a) no absorption, high reflection (mirror case, corresponds to chromium mask), (b) increased absorption, reduced reflection, (c) reflection of opaque media = reflection of substrate media (glass), (d) high absorption, no reflection of opaque media corresponding to black silicon. In (d) the grating characteristics occur at higher absorption and results in the same performance of back reflections as before. The transmission of the grating is shown in (e) as reference.

It is important to emphasize that these characteristics are independent of the wavelength. In this approach, the wavelength determines only the spectral angle and/or lateral position of the diffraction orders.

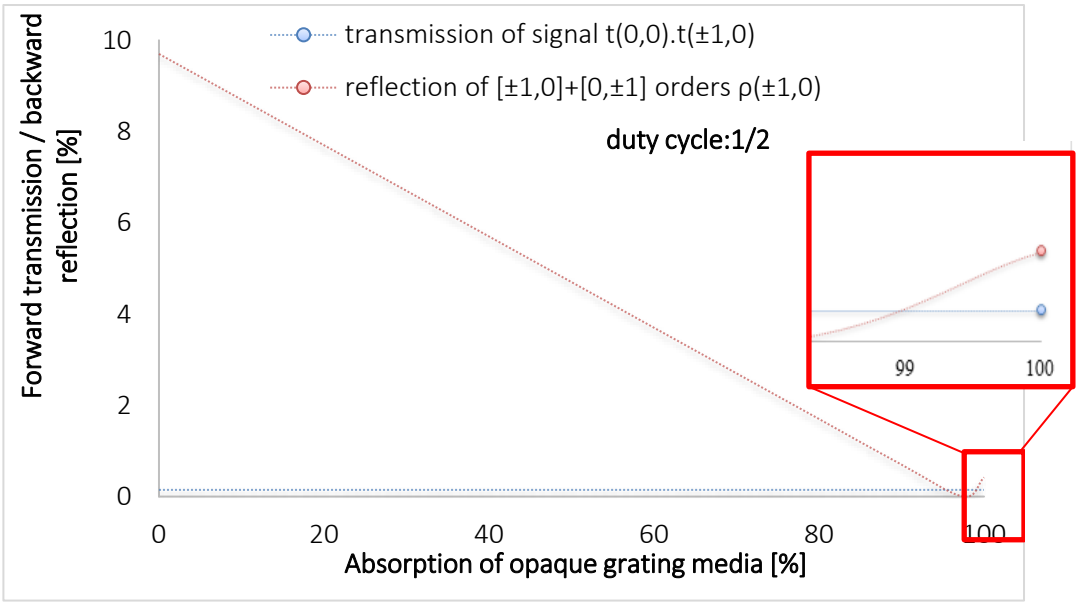

Fig.3.26 Grating performance for duty cycle of ½. Only 3% of the incident light is transmitted to the sample. The reflected light from the sample (ideal mirror) passes this grating once again so that 0.147% will finally reach the camera sensor. Depending on the absorption of the opaque medium, between 0% and 9.7% are reflected back for highly absorbing (~black silicon) and non-absorbing (~chromium) materials. The changing characteristic of the grating for high absorption of the opaque medium is clearly visible. The back reflections should be less than the signal light for our measurements.

In summary, the following parameters influence the strength of the illuminating and disturbing light components:

- ✓ diffraction efficiency of 0 and ±1st orders,
- ✓ geometrical parameter of the duty cycle,
- ✓ material parameter: absorbance, reflectance of the opaque amplitude grid structure.

Only the 0 order passes the spatial filter. This corresponds to the grating transmission for the illuminating 0 order of $\tau_{grating}(0,0)$. The incoming light on the test sample is reflected back by a factor of $\rho_P < 1$. This reflected light is spread into an angular spectrum which depends on the surface shape. This spectrum is filtered by the spatial filter. It results in a transmission of $\tau_F \leq 1$. Indeed, the light passes once again the cross grating with a transmission of $\tau_{grating}(\pm1,0)$. This time, however, the mixed $(0, \pm1^{st})$ orders are selected by the spatial filter (optically conjugated to the first spatial filter) for 4 times with an individual diffraction efficiency of $\eta(\pm1,0)$ and $\eta(0,\pm1)$. In summary, a transmission factor of $4\cdot\eta(\pm1,0)$ results. In fact, each of the optics introduces losses τ_L (forwards and backwards), The performance of the measurement signal τ_{signal} is expressed by the multiplication of the transmissions of each component and the reflection at sample ρ_{sample} following:

$$\tau_{signal} = \tau_{grating}(0,0) \cdot \rho_{sample} \cdot \tau_F \cdot {\tau_L}^7 \cdot \tau_{grating}(\pm1,0) \tag{3.47}$$

This can be simplified to:

$$\tau_{\mathrm{signal}} = \tau_{\mathrm{grating}}(0,0) \cdot \tau_{\mathrm{grating}}(\pm 1,0) \cdot \mathrm{C} \tag{3.48}$$

The variable of C includes all the components losses in the beam path. The terms of ρ_{sample} and τ_F depend on the test sample and reduce the setup efficiency further for real freeform samples for instance. The constant of C equals to 1 under the assumption of lossless optical components and a flat ideal mirror, else $0 \leq C < 1$ is valid. The "signal-to-back-reflection" ratio of the setup SRR_{setup} can finally be estimated by the relationship of the (transmitted) measurement signal by the unwanted reflection ρ_{br} in the accumulated orders (±1,0) and (0,±1) of the grating $\rho_{grating}$ (±1,0):

$$\mathrm{SRR}_{\mathrm{setup}} = \frac{\tau_{\mathrm{signal}}}{\rho_{\mathrm{br}}} = \frac{\tau_{\mathrm{grating}}(0,0) \cdot \tau_{\mathrm{grating}}(\pm 1,0) \cdot \mathrm{C}}{\rho_{\mathrm{grating}}(\pm 1,0)} \tag{3.49}$$

This should be as large as possible for a successful measurement. In our case, the SRR_{setup} results in nearly 0.03 for a chromium mask and 0.72 for black silicon. This means that the back reflections overcome the signal intensities for a simple chromium grating. Obviously, a measurement is not possible with a highly reflecting chromium grating. Replacing this mask by the structured black silicon glass wafer allowed a measurement based on a difference image with and without a sample.

3.5 Summary

In this chapter, a novel theoretical approach based on a linear approximation of the angular spectrum propagator is presented. This approximation enables the reconstruction of a complex wavefront by using a binary modulating cross grating and the following optical Fourier filtering as well as the Fourier analysis of the captured intensity signal. The great advantage of the presented approach is the possibility to reconstruct complex wavefronts at any arbitrary propagation distance after the amplitude grating. After the derivation of the wavefront basic theory, its extension was presented. Based on it, it becomes possible to measure surfaces not only in transmission but also in reflection. For this, a minimal change in the experimental setup is needed .

IV. Simulation

In this chapter some simulations are presented in order to confirm our theoretical investigations and to find well suited parameters for the preparation of the experimental validation of our theory. In the first section, free-form wavefronts are modulated with an amplitude diffractive grating under ideal conditions. From the acquired intensities, the theory is numerically tested. The second section examines the influence of the tolerance of the most important parameters on the accuracy.

4.1 Simulation under ideal conditions

This part of simulation shows how well the proposed approach works under ideal conditions. Therefore, all important parameters are considered ideal, i.e. free of errors. The environmental conditions are likewise considered as ideal. Besides, in all simulations, care is taken to adjust the dimensioning of the intensity image (pixel size and number of pixels) with the grating period and the free-form wavefront being tested in such a way that the Nyquist criterion of proper sampling is obeyed: the bandwidth of the signal spectrum is limited and a sampling frequency (sampling rate of the camera sensor) which is more than twice the maximum spatial frequency of the measured signal is used. Then the subspectra of the intensity images are separated and aliasing can be avoided. The simulation is divided into two steps: First, the gradients of the reconstructed wavefronts are compared to the original test wavefronts. Second, the different fully reconstructed wavefronts are compared among each other. The aim of this separation is to distinguish between the errors resulting from the integration and those from the approximations of the presented theory.

4.1.1 Generating freeform wavefronts

The main objective of this thesis is the development of a measuring method, which allows an accurate and rapid characterization of wavefronts generated by free-form optical elements. In order to create a clear and detailed quality analysis of the measuring method, it is meaningful to test the theory by using various free-forms. To investigate the influence of the sample geometry on accuracy, fifty arbitrary free forms were numerically generated. These wavefronts differ mainly in the form and the maximum gradient. Fig.4.1 shows the histogram of the maximum gradient of the aforementioned free forms. Three different freeform samples used as test objects are reported in Figure.4.2.

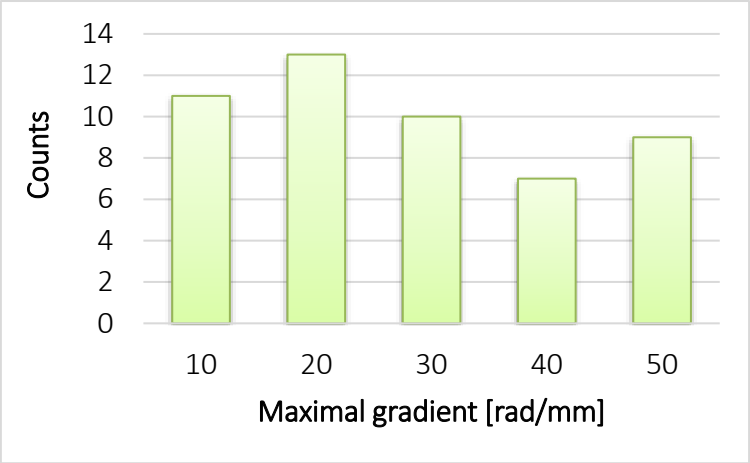

Fig.4.1 Histogram of the maximum used gradient.

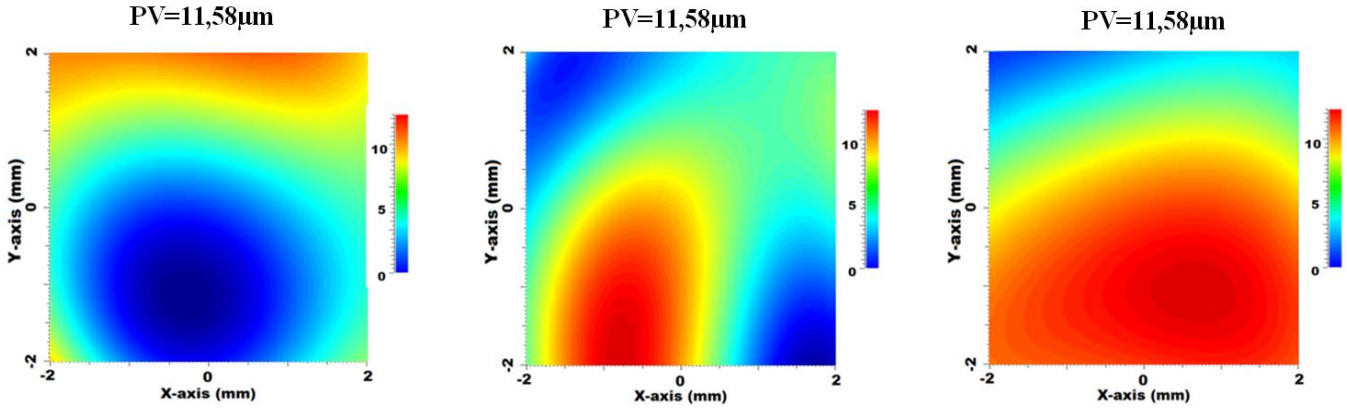

Fig.4.2 Test objects: three different numerical free forms.

4.1.2 Wavefront modulation by the amplitude grating

The test wavefront passes the grating. The result of the modulation between the grating transparency function and the freeform is numerically propagated to different distances. For this numerical propagation, the angular spectral method is used. Fig.4.3 (left) shows the intensity distribution of the diffractive grating. On the other hand, fig.4.3 (right) shows the modulation between the grating and a selected freeform wavefront at the propagation distance of 500µm. This freeform is also used to show the important steps in the simulation for which the propagation distance varies from 50µm to 1mm in 50µm steps. To emphasize the validity of the theory at arbitrary distances and not only at special Talbot distances, the cited theory is therefore propagated to distances different from the fractional Talbot distances.

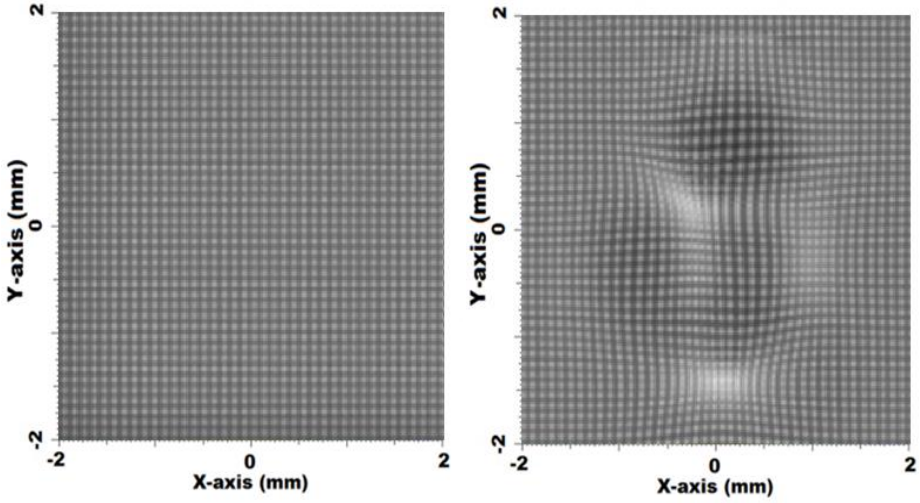

Fig.4.3 Example of the intensity distribution without (left) and with test wavefront of peak function (right) using a grating period of d_x = 100µm and propagation distance of z = 500µm.

4.1.3 Gradient extraction and comparison to the original test object

Assuming in the next step that the signal intensity behind the grating is captured by the camera, the intensity distribution is Fourier transformed. The subspectra in x and y directions are therefore filtered and shifted to the center of the frequency domain for the analysis (demodulation). Then, a Gaussian filter with slight slopes is used for appodisation. The exact position of the center of the Gaussian filter is calculated analytically and corresponds to $\omega_{x0} = 2\pi/d_x$. The exact position is determined using a subpixel alghorithm and the dimension of the used filter is $D_f = 2\pi/d_x$. After the demodulation, the gradients in x and y are extracted. Fig.4.4 shows the effect of the maximal gradient on the gradient extraction result. Two freeform peak functions, created by Matlab$^{(TM)}$'s function toolbox, having a maximum gradient of 20rad/mm and 30rad/mm are modulated by the grating and propagated to the distance of 500µm. The extracted gradient maps are shown in Fig.4.4. In the case of freeform with the highest gradient, the gradient map is wrapped. On the other hand, the phase has to be unwrapped. In our studies, the Goldstein Algorithm is used [151].

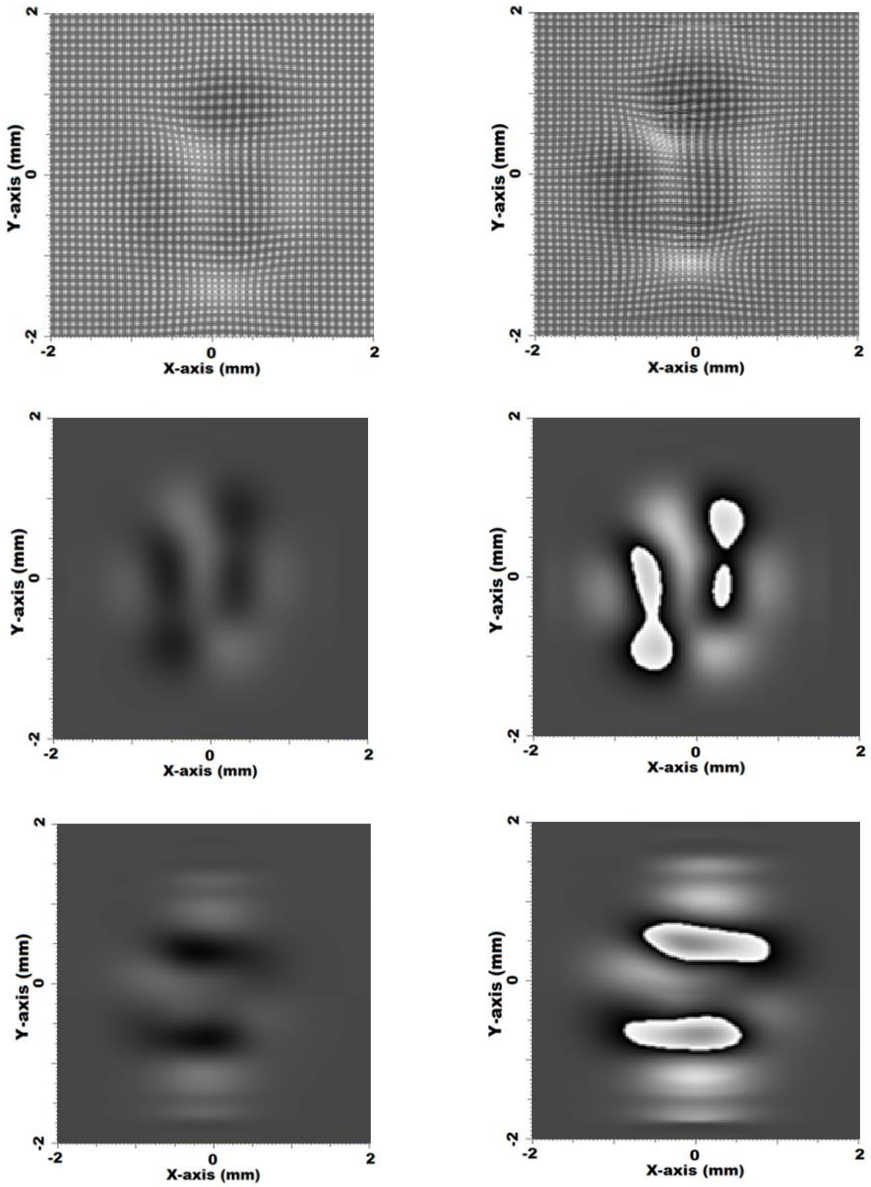

Fig.4.4 Comparison of two test distributions, i.e. Peak functions, having a maximum gradient of 20rad/mm (left) and 30rad/mm (right). Top line: captured intensity distributions, Center line: extracted x gradient distributions, Bottom line: extracted y gradient distributions.

After the successful extraction of the x and y gradients, the reconstructed and the original gradients are compared with each other. As example for this deviation, Fig.4.5 shows the difference between the reconstructed gradients of the peak function wavefront with 30rad/mm and the original one at the distance of 500µm behind the grating. The maximal deviations 0,025rad/mm and 0,06rad/mm for x and y gradient respectively are quite small related to its maxima. This processing step can be considered as validated at this position. A detailed analysis with more parameters will be presented in the next part of this chapter.

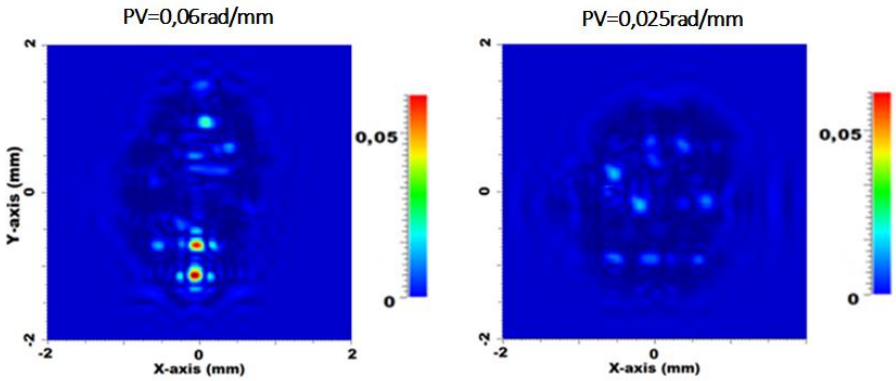

Fig.4.5 Difference to the original gradients of a peak wavefront at a propagation distance of 500µm: difference of the x gradient (right), difference of the y gradient distribution (left).

4.1.4 Two-dimensional integration

The last simulation step is the integration of the two gradients using the Frankot & Chellappa integration method [146]. Thereafter, the resulting wavefront is compared to the original wavefront. Fig.4.6 shows an example of the 2D original and reconstructed wavefronts of the peak function at the position 500µm behind the grating. The PV at this position of the original and reconstructed surfaces shows a deviation of 60nm. A detailed analysis with more parameters will be presented in the next part of this chapter.

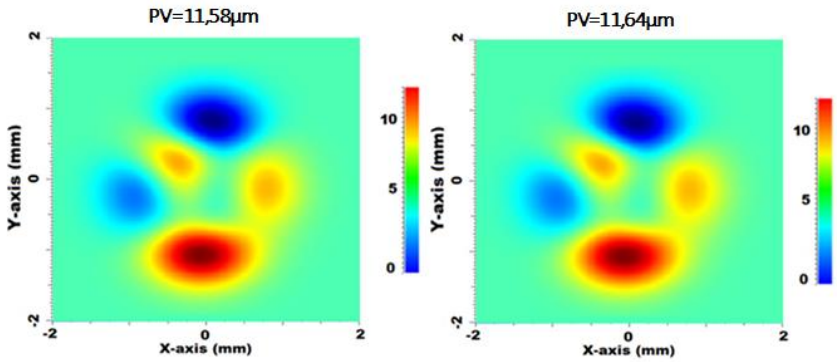

Fig.4.6 Original (left) and reconstructed wavefronts (right) of the peak function at the position 500µm behind the grating.

The set of theory steps discussed in this chapter is summarized in the chart below. The goal is to highlight their chronological order.

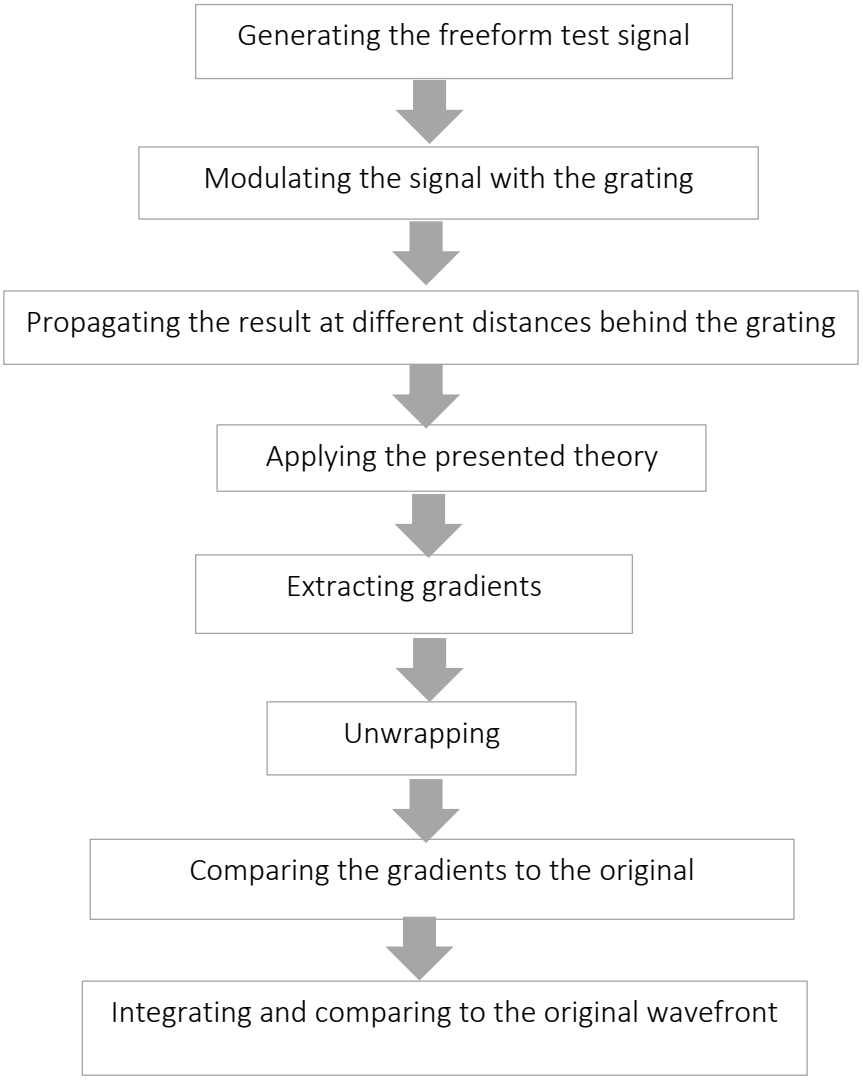

Fig.4.7 Flowchart of our simulation and numerical tests.

4.1.5 Simulation parameters

In order to demonstrate the validity and the proper functioning of the described method, not only in a single propagation position behind the grating or for a specific form, several simulations of different gradients at different positions are performed. 20 simulations per position are accomplished. In the following diagrams, the results of the statistical study using the standard deviation are reported. The aim is to give the necessary explanation of the error evolution in the obtained results. In order to simulate simultaneously the influence of the wavelength, the grating period and the distance z behind the grating, two wavelengths (400nm, 800nm) and two grating periods (25µm, 150µm) are selected. The propagation distance varies from 50µm to 1mm behind the grating in 50µm steps. Simulations with four-parameter combinations are performed as follows:

- ✓ Parameters for simulation1: λ= 800nm, d_x = 150µm.
- ✓ Parameters for simulation2: λ= 800nm, d_x = 25µm.
- ✓ Parameters for simulation3: λ= 400nm, d_x = 25µm.
- ✓ Parameters for simulation4: λ= 400nm, d_x = 150µm.

The aforementioned combinations are used to perform the extraction of the gradients x and y depending on the propagation distance behind the diffractive grating for all fifty arbitrary free forms. For each reconstructed wavefront, the difference to the original one is calculated.

4.1.6 Results and discussion

Since errors of the gradient extraction introduced by our calculation and approximations will be evaluated, all simulation parameters are considered as error-free and free of noise.

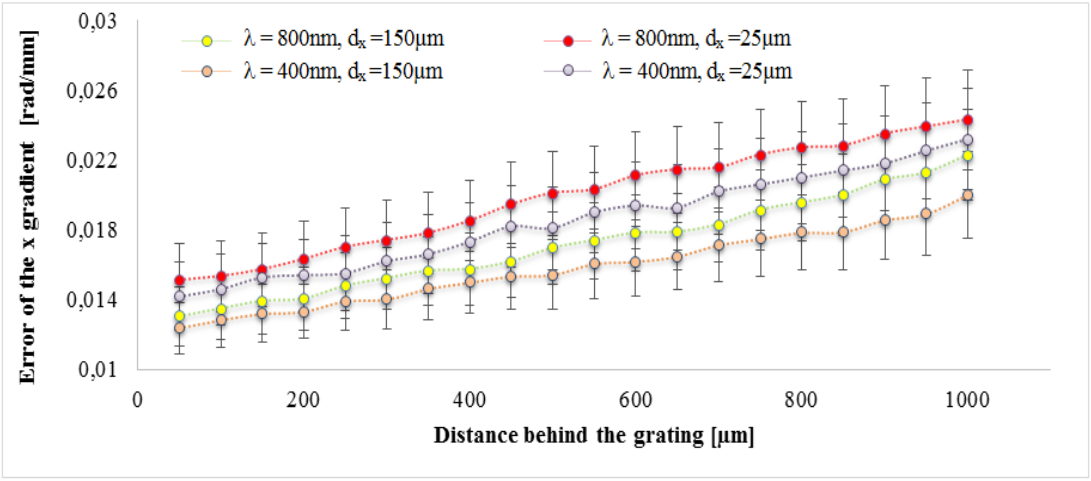

(a)

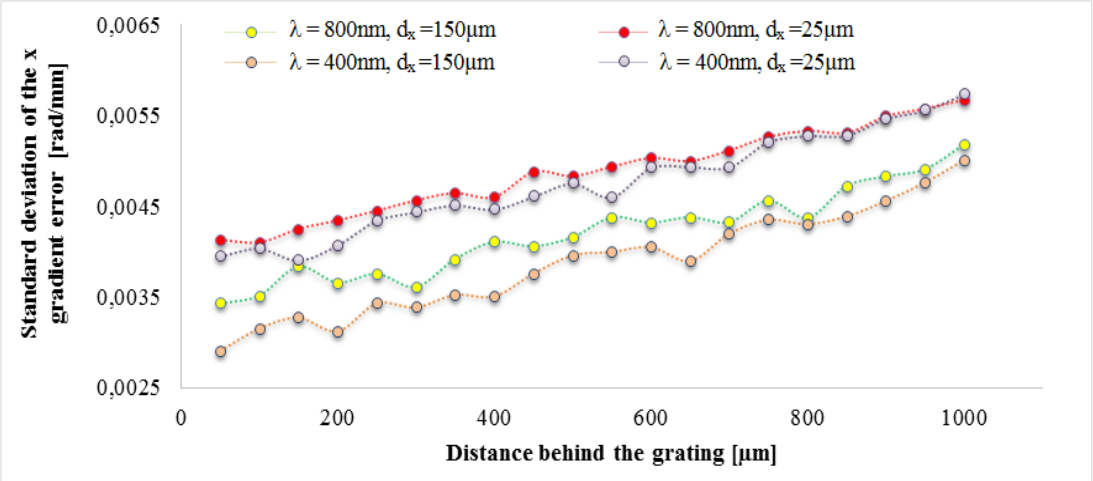

(b)

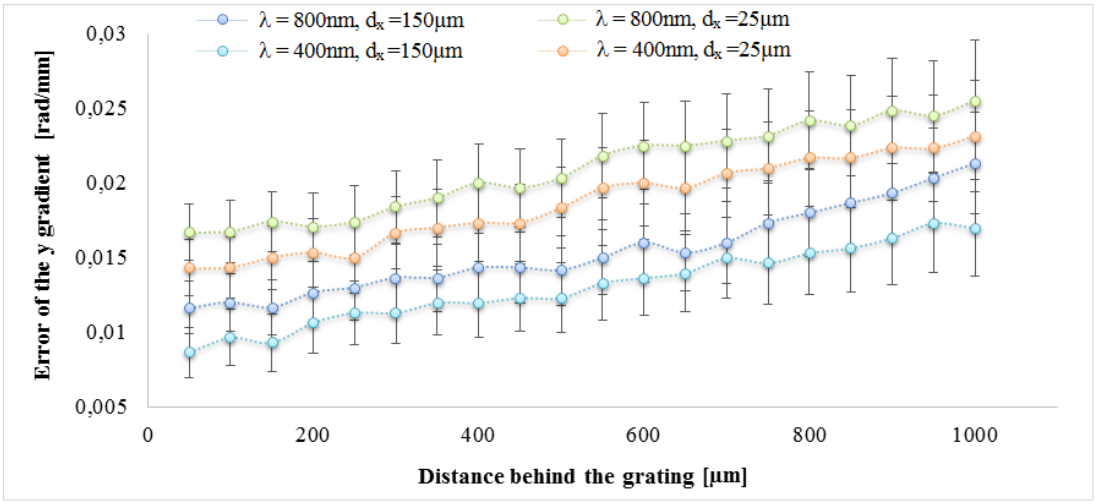

(c)

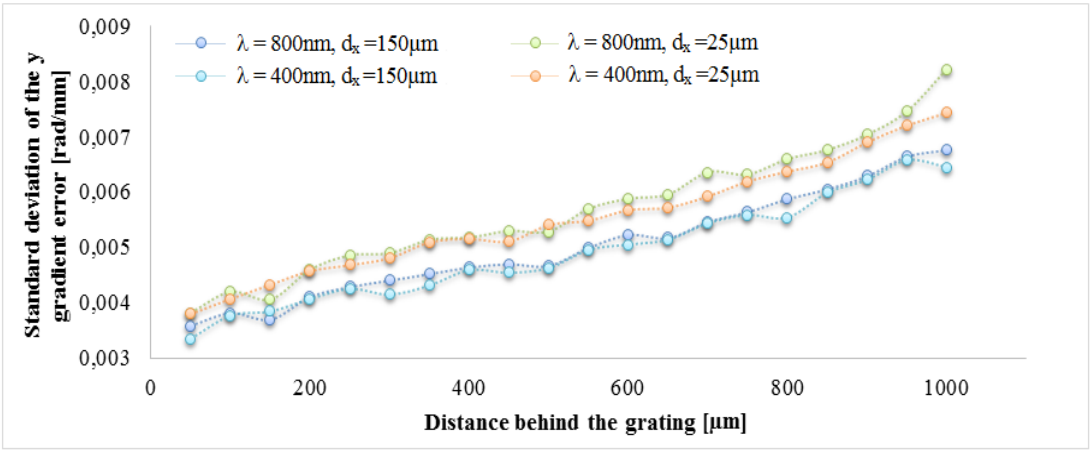

(d)

Fig.4.8 Errors of phase gradient in x gradient (a) and y gradient (c) vs. propagation distance behind the grating as well as their corresponding standard deviation (b) and (d) respectively.

In general, the reconstruction of the gradients using the presented theory shows good results. The error increases with increasing distance behind the diffraction grating (Fig.4.8). It was observed that the development of the standard deviation for all 4 parameter combinations has the same similar course of the mean value analysis. The error increases with increasing propagation distance and is caused by the first approximation of our proposed method. It can be explained by the curvature of the propagation phase ϕ_z: The larger the propagation distance is, the bigger the curvature of the propagation phase and the higher the deviation of ϕ_z to our introduced linear approximation become. The other error source is the approximation of ϕ_t used for the extraction of the gradients. This error approaches to a minimum for a very small value of ϕ_t. It should be as small as possible. This is fulfilled for a large grating period, smaller propagation distance and shorter wavelength (see Eq.3.10). Fig.3.11 shows the evolution of ϕ_t in dependence on the distance behind the grating. The gradient error evolution as a function of the propagation distance z reveals that there is a similar course for ϕ_t . It can be notable that the gradient error is likewise dependent on ϕ_t .

In both combinations using grating with 25µm period, and compared to the gratings with150µm period, the error increased. However, the maximum error of the gradient reconstruction using both grating periods and 400nm wavelength at the propagation distance of 1mm behind the grating is less than 0.84% based on the maximum x gradient and only 0.25% on the maximum y gradient. For the position 50µm behind the grating, the maximum error is less than 0.036% and 0.042% based on the maximum of y and x gradient, respectively. The difference between the errors generated at the wavelengths 400nm and 800nm in the propagation distance 50µm is less than 0.001% with respect to the maximal gradient. In the propagation distance of 1mm, the difference is 0.002% relative to the maximal gradient. This simulation shows that results issued from gratings with bigger periods have less negative influence on the reconstruction of the gradients. On the other hand, results deduced from gratings with small periods show higher deviations. Besides, the distance and the position behind the diffractive grating is of a great importance on the error improvement. In contrast, the influence of the wavelength plays a minor role. Thus, the degree of freedom can be expanded by the search for the appropriate wavelength. This confirms our proposed theory. After the successful extraction of the x and y gradients, the 2D integration of the two gradients is performed. This step is carried out for all extracted gradients from the previous section and the resulting wavefront is compared to the original ones. As mentioned in the previous subsection, all remaining parameters are considered as error- and noise-free. Since the error of the gradient extraction increases with increasing axial position z behind the grating, the peak-to-valley value of the mean difference to the original wavefront also increases. Therefore, the additional integration error to the result should be evaluated when simulating an increasing distance z behind the grating. After the integration process, the same error development was observed as in the previous gradient extraction step (Fig.4.9). It has been shown that the smallest peak-to-valley error is related to bigger grating periods. In contrast, the influence of the wavelength plays a minor role. Nevertheless, using smaller wavelengths results in smaller errors compared to longer wavelengths.

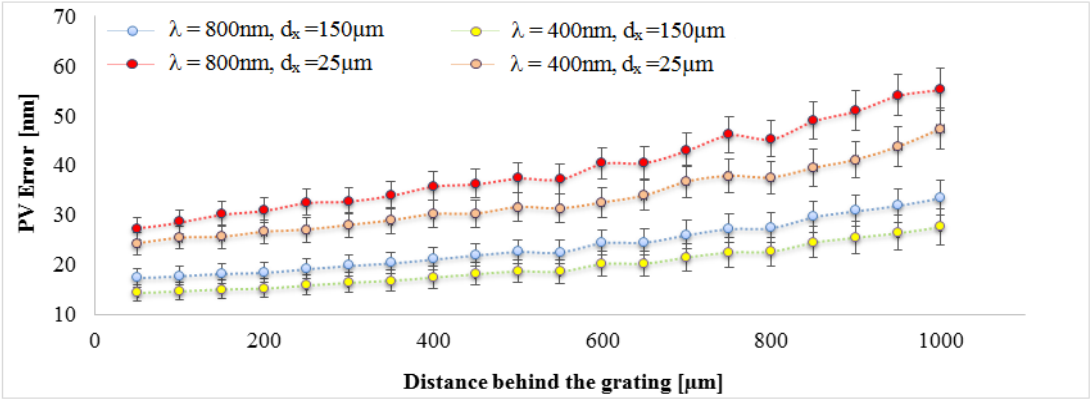

(a)

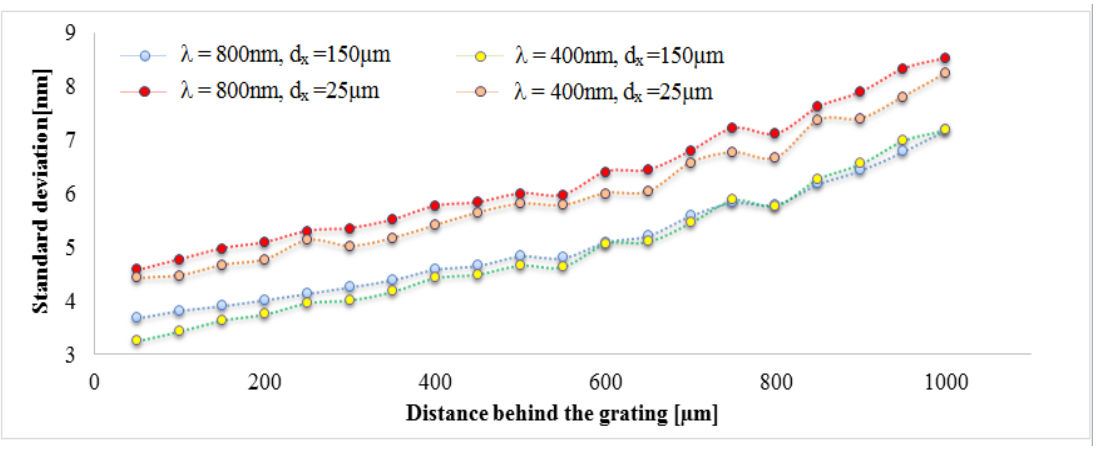

(b)

Fig.4.9 Peak-to-valley error (a) and the corresponding standard deviations (b) vs. propagation distance.

Based on the maximum height of the test wavefront, the maximum mean error at the propagation position of 1mm is less than 0.3% for all parameter combinations. At z = 50µm, the error is reduced to 0.014%. The development of the standard deviation as a function of the propagation distance behind the grating shows a clear increase with increasing distance. At z = 50µm, the standard deviation is less than 5nm. At the axial position of 1mm behind the grating, the standard deviation increases to 9nm.

4.2 Simulation with tolerance analysis and noise

4.2.1 General introduction

The wavelength of the used illumination system, the grating period of the diffraction gratings and the axial position of the propagated signal behind the diffraction grating are the important parameters for the measurement process. Therefore, a tolerance analysis concerning these parameters is performed and their influence on the quality of the reconstruction is evaluated. The same previously applied freeform surfaces are used in these simulations. Tolerances are considered and expected later in our experimental setup. In order to get as close as possible to the experimental environment, an arbitrary noise is added to the intensity image. The maximum amount of this noise is 0.5% of the normalized image intensity (Fig.4.10).

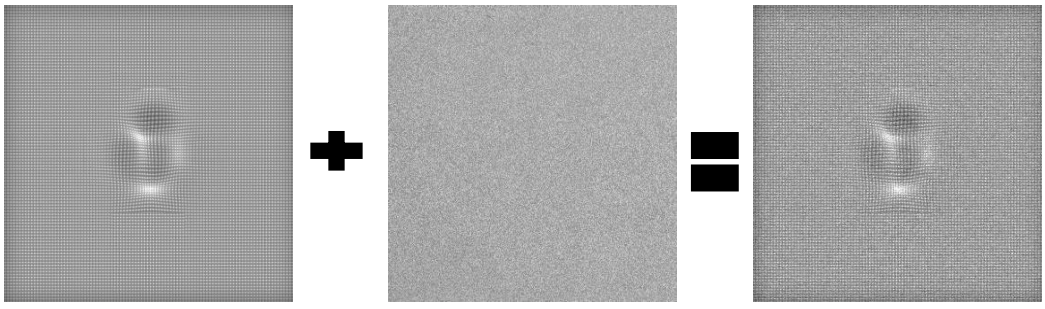

Fig. 4.10 Introduction of additive noise to our expected intensity distribution.

Indeed, the influence of the spatial filtering mentioned in the theory is investigated and compared to the case without spatial filtering. All these investigations are analyzed statistically using peak-to-valley and RMS values. Fig.4.11 presents a flow chart for this analysis.

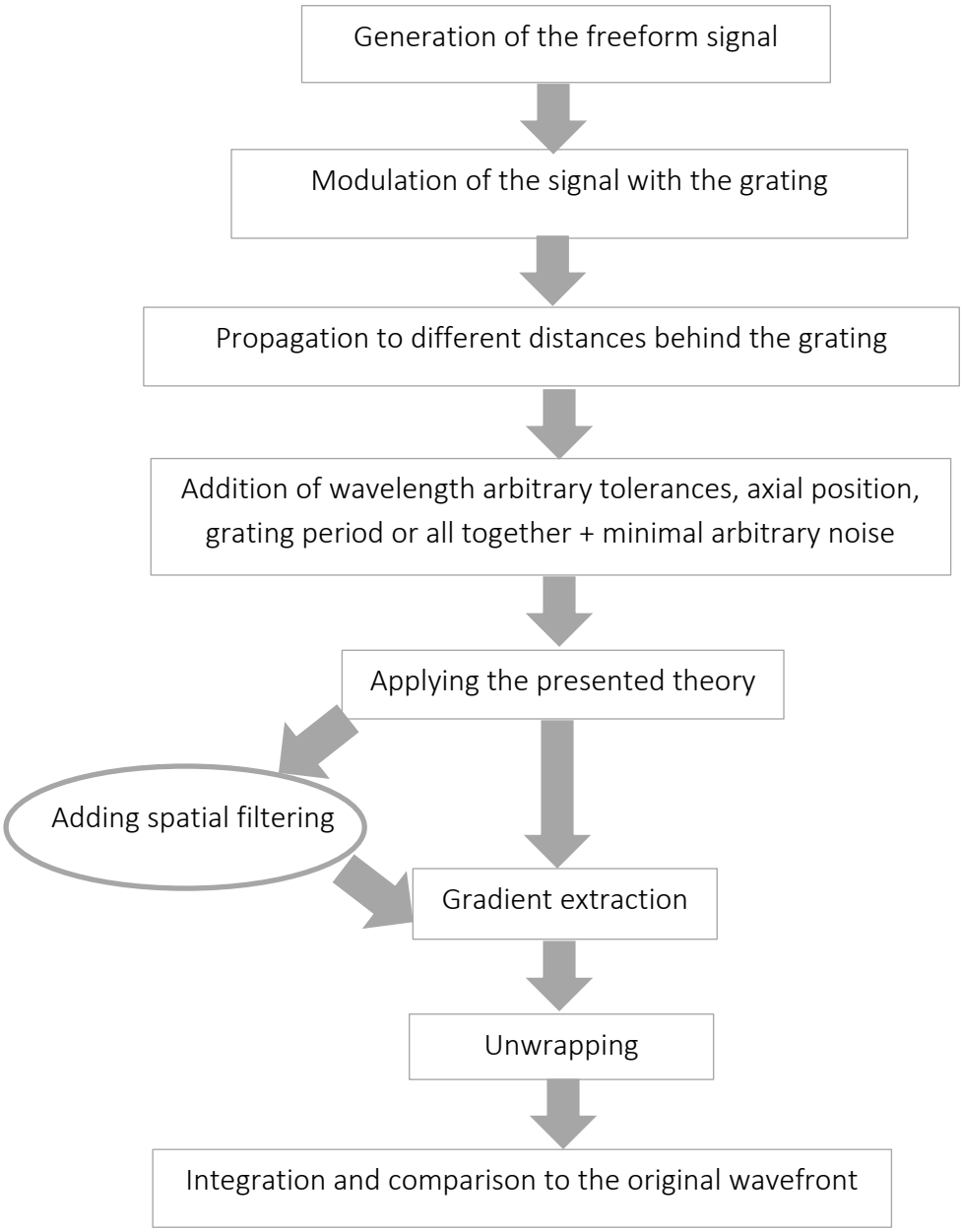

Fig.4.11 Flow chart of the tolerance analysis.

4.2.2 Simulation with wavelength tolerance

The wavelength of an illumination source is not temporally stable and varies with the type of light source. In the present work, LEDs are mainly applied. The emission wavelength change depends on the temperature changes. In fact, the semiconductor band gap varies as a function of the temperature, which leads to a change in the wavelength. Indeed, the deviation is different and depends on the material. In our applications, the instability of the wavelength has a negative influence on the diffraction angles behind the diffraction grating.

In the presented theory, the derived prefactor for the gradient extraction also contains a wavelength term (see Eq.3.20 and 3.21). Hence, the influence of this tolerance on the quality of the reconstruction is statistically analyzed by numerical simulation. This is achieved when the grating period (50µm) and the position z (200µm) are fixed and assumed as error-free. The wavelength varies from 400nm to 700nm in steps of 50nm. Each step is simulated with the previously proposed fifty free forms. In each of these simulations, 5nm error is added to the wavelength. This error value represents the maximum error given in the data sheet of the LEDs. The results are shown in Fig.4.12.

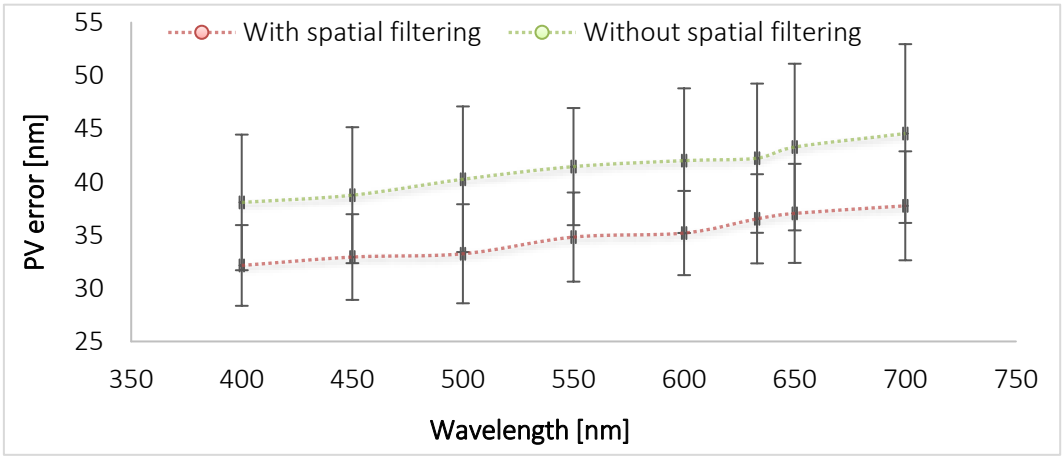

(a)

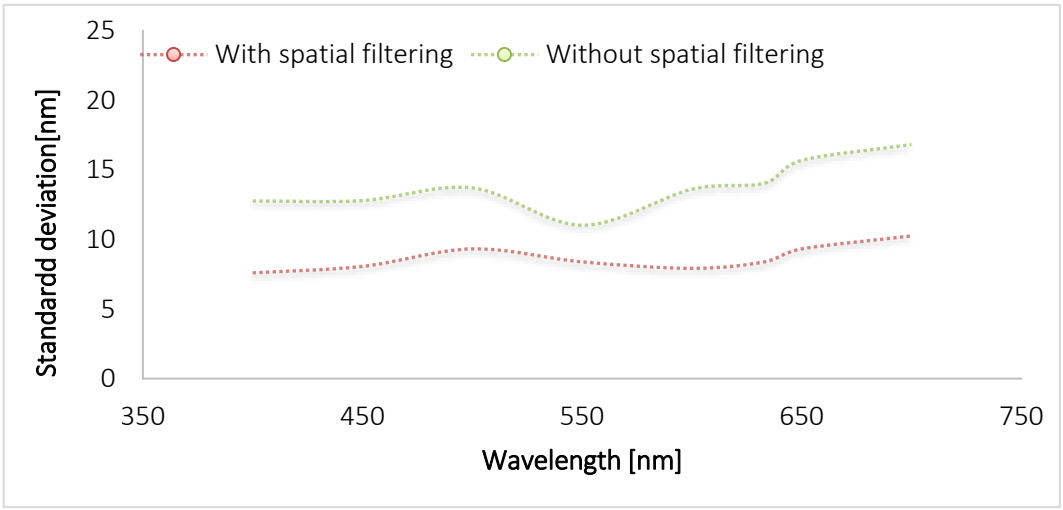

(b)

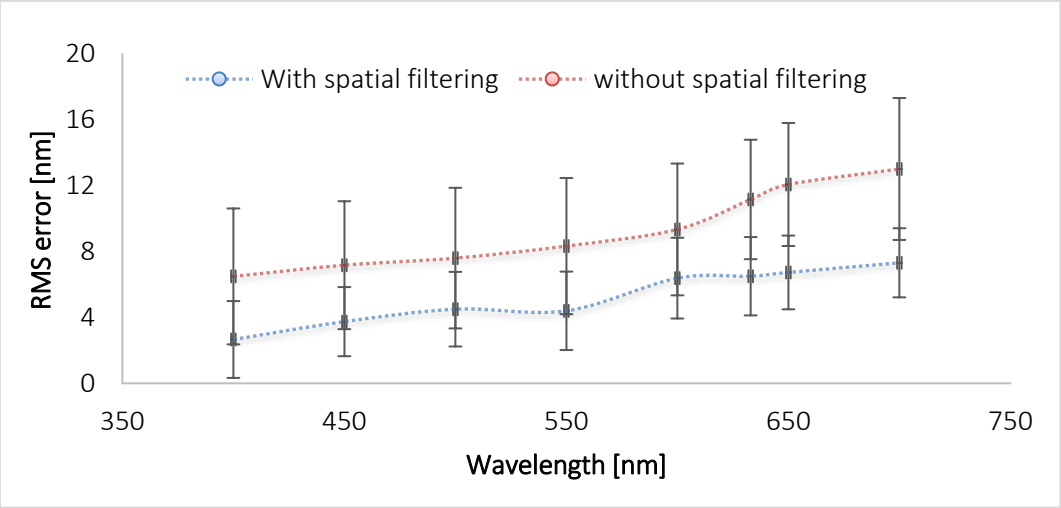

(c)

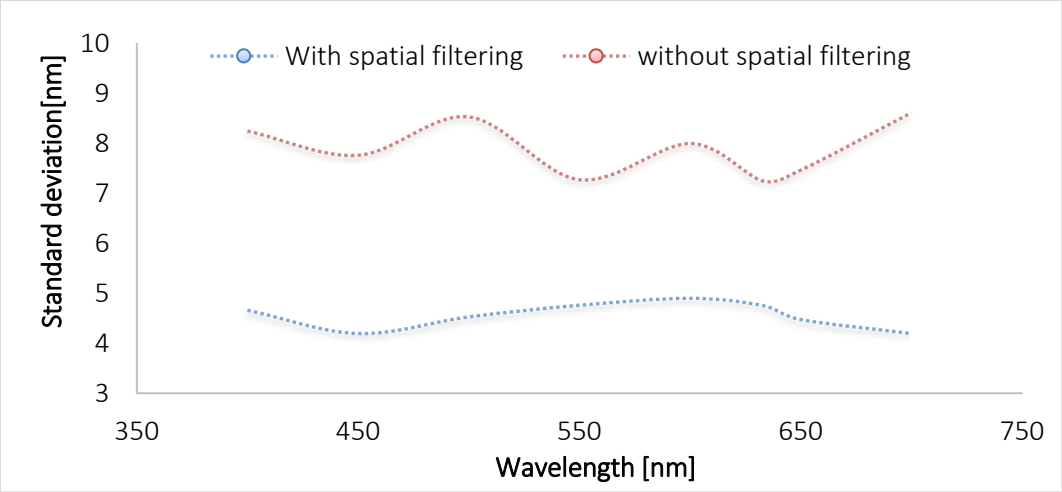

(d)

Fig.4.12 Deviations of numerical wavefront reconstructions introduced by wavelength tolerances (5nm). (a) Peak to valley, (b) Standard deviation of PV, (c) RMS, (d) Standard Deviation of RMS.

For the explanation of this result, the error propagation analysis is carried out first. The equation for the extraction of the gradient consists of a prefactor $y = -\frac{\sqrt{d_x^2-\lambda^2}}{2z\lambda}$ and a second term depends on the properties of the wavefront and the applied numerical processing. The prefactor in the equation consists of three variables. Those are the wavelength of the illumination λ, the grating period d_x (for d_y is straight forward) and the distance z. Since the statistical independence of these parameters is ensured, the uncertainties for the prefactor using the Gaussian error propagation law can be calculated [152,153]. First, the derivative of the prefactor is derived with respect to each of the three parameters. For each of these parameters, the maximum possible measurement error is indicated and multiplied with the aforementioned derivative.

Therefore, the propagation error of the prefactor Δy can be calculated as following:

$$\Delta y = \sqrt{\left(-\frac{d_x}{2z\lambda\sqrt{{d_x}^2-\lambda^2}}\cdot\Delta d_x\right)^2+\left(\frac{{d_x}^2}{2z\lambda^2\sqrt{{d_x}^2-\lambda^2}}\cdot\Delta\lambda\right)^2+\left(\frac{\sqrt{{d_x}^2-\lambda^2}}{2\lambda z^2}\cdot\Delta z\right)^2} \qquad (4.1)$$

In this part only the influence of the wavelength tolerance Δλ on the reconstruction is shown, therefore the tolerances of Δd_x and Δz are considered as zero. The influence of the wavelength tolerance on the total error propagation is simplified as follows in equation (4.2).

$$\Delta y(\lambda) = \sqrt{\left(\frac{{d_x}^2}{2z\lambda^2\sqrt{{d_x}^2-\lambda^2}}\cdot\Delta\lambda\right)^2} = \left(\frac{{d_x}^2}{2z\lambda^2\sqrt{{d_x}^2-\lambda^2}}\cdot\Delta\lambda\right) \qquad (4.2)$$

According to the theory, the approximation for the gradient extraction is applied if φ_t is small. Fig.4.13 shows the influence of the wavelength error on the prefactor and the φ_t as a function of the wavelength.

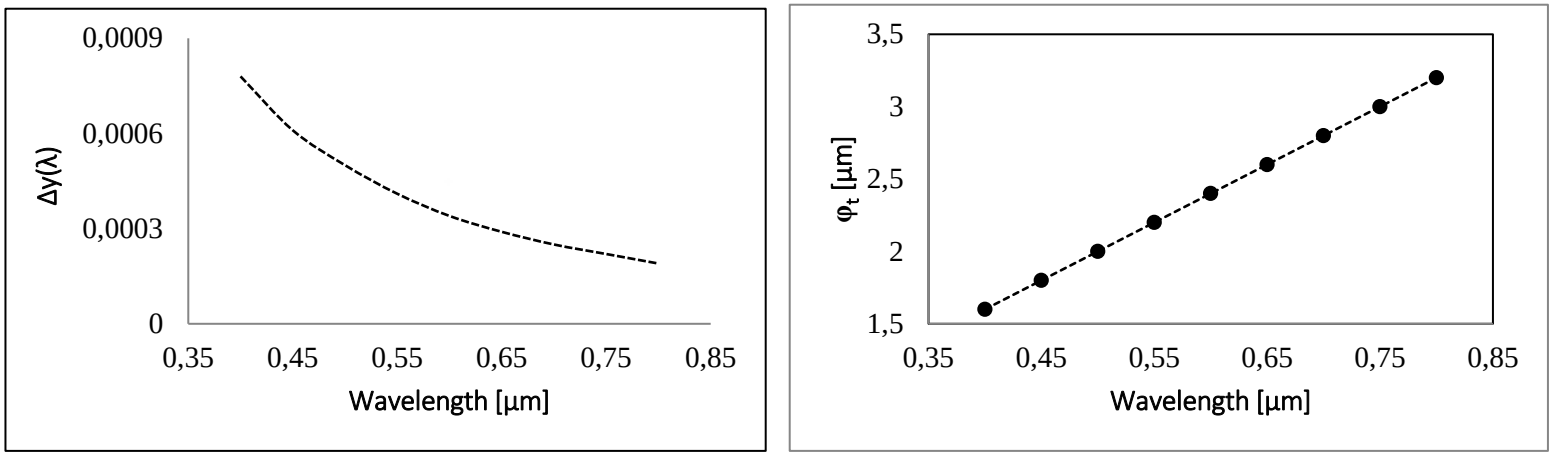

(a) (b)

Fig.4.13 (a) Influence of the wavelength error on the prefactor y, (b) φ_t as a function of the wavelength.

It is noteworthy that φ_t becomes larger with increasing wavelength, whereas the prefactor measurement error decreases. Therefore, the evolution of the wavelength error influence on the wavefront reconstruction has the same course of φ_t. For smaller wavelengths, both investigations of peak-to-valley with and without spatial filtering show a reducing influence of tolerances on the quality of reconstructions. The average value of this error for a wavelength of 400nm is 31.1nm when using the spatial filtering. In the case of no filtering, this error increases for the same wavelength up to 38.08nm.

It also increases with increasing wavelength and equals to 37.76nm at the wavelength 800nm with spatial filtering. Without filtering, the deviation for this wavelength is 44.56nm. The standard deviation of these measurements remains relatively constant along the entire wavelength range. However, spatial filtering has a positive influence (reduction) on the standard deviation. Without spatial filtering, the standard deviation at the wavelength 400nm is 12.7nm. By applying the spatial filtering, the value is only 7.5nm. At the wavelength 800nm, the deviation reaches 16.8nm without filtering. With the filtering, the error is 10.2nm. The RMS analysis shows the same behavior as in the peak-to-valley analysis. At smaller wavelengths, the wavelength error has a minimal impact on the overall reconstruction of the walls front. At shorter wavelengths, the spatial filtering has a larger impact on the RMS value compared to the case without filtering. At 400nm, the mean value of the RMS without filtering is 6.49nm with 8.25nm standard deviation. With the implementation of the spatial filtering, the mean value is only 2.66nm and the standard deviation is 4.66nm. At 800nm and without filtering the mean becomes 13.01nm with 8.6nm standard deviation. With filtering, the value is only 7.31 nm with 4.19 nm standard deviation. The standard deviation of the RMS remains relatively constant within the range of wavelengths from 400nm to 800nm. The peak-to-valley error as well as the RMS error showed a low value at smaller wavelength. It means that the measurement method is more sensitive to the wavelength instability at increased wavelength values;

4.2.3 Simulation with Gratings period tolerance

As with the wavelength, the inaccuracy of the grating period influences the diffraction angles behind the grating and the value of the prefactor (see Eq.3.20 and 3.21), too. This should be considered for the design (dimensions and axial position) of the following spatial filter. The cited deviations can reduce the overall accuracy of the measurement process. Indeed, the applied grating is made using a precise lithographic manufacturing technique. However, as with all manufacturing methods, deviations from the desired geometries up to 1µm are observed. Therefore, a simulation which numerically considers this influence should be performed. A wavelength of 633nm and a z position of 200µm are applied. The grating period varies from 25µm to 150µm in increments of 25µm. Each position was also simulated with the previously introduced 50 different freeforms. For each of these simulations, an additional 5µm error is added. This value is five times greater than the largest measurable grating period deviation.

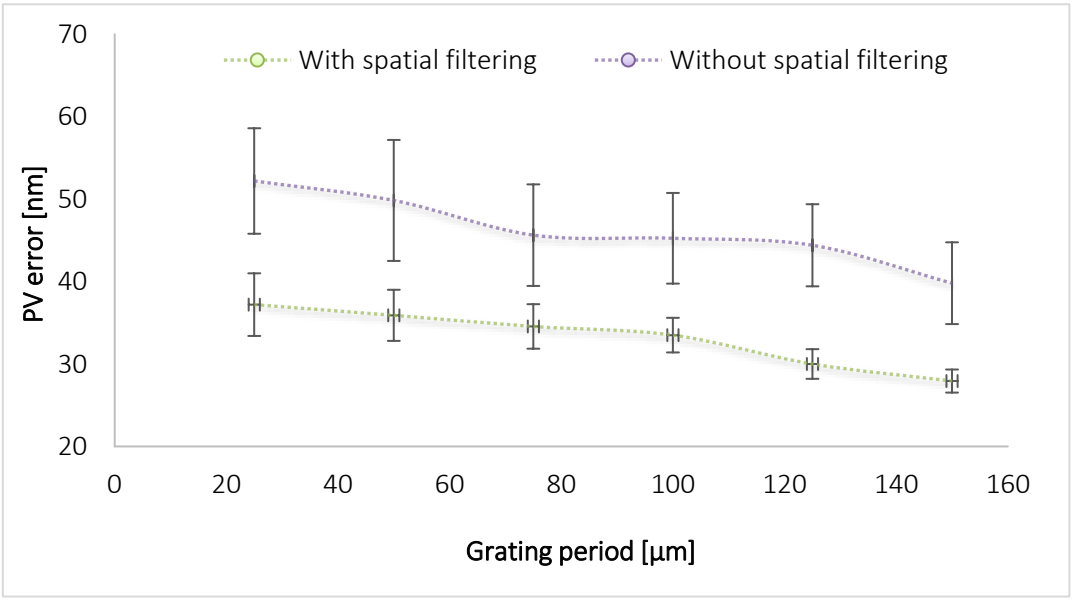
With spatial filtering
Without spatial filtering
PV error [nm]
70
60
50
40
30
20
0
20
40
60
80
100
120
140
160
Grating period [µm]

(a)

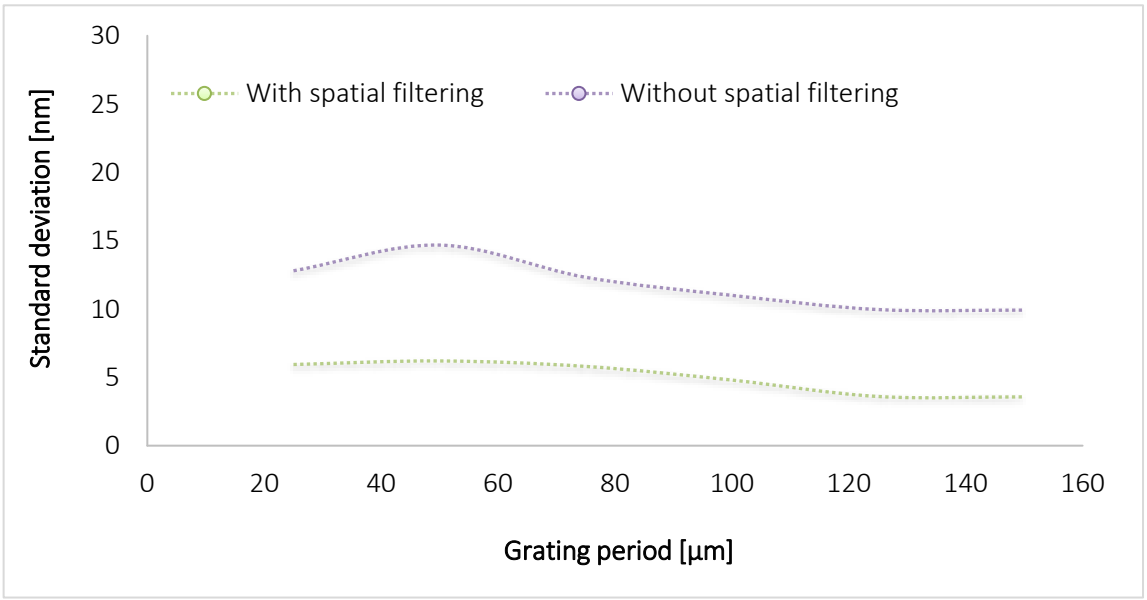
With spatial filtering
Without spatial filtering
Standard deviation [nm]
30
25
20
15
10
5
0
0
20
40
60
80
100
120
140
160
Grating period [µm]

(b)

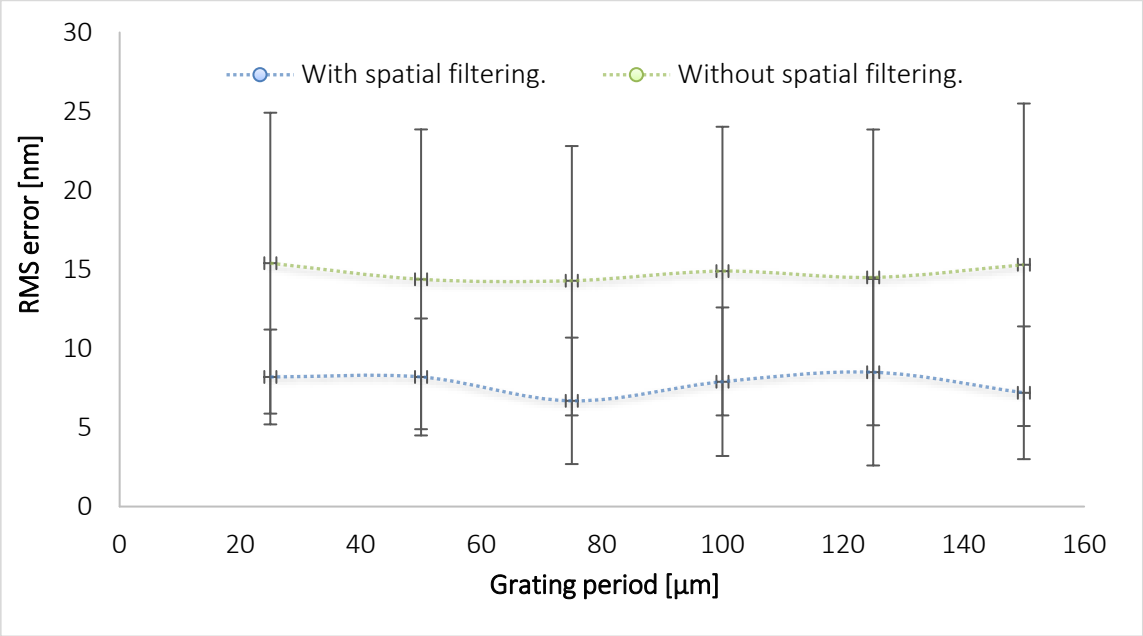

(c)

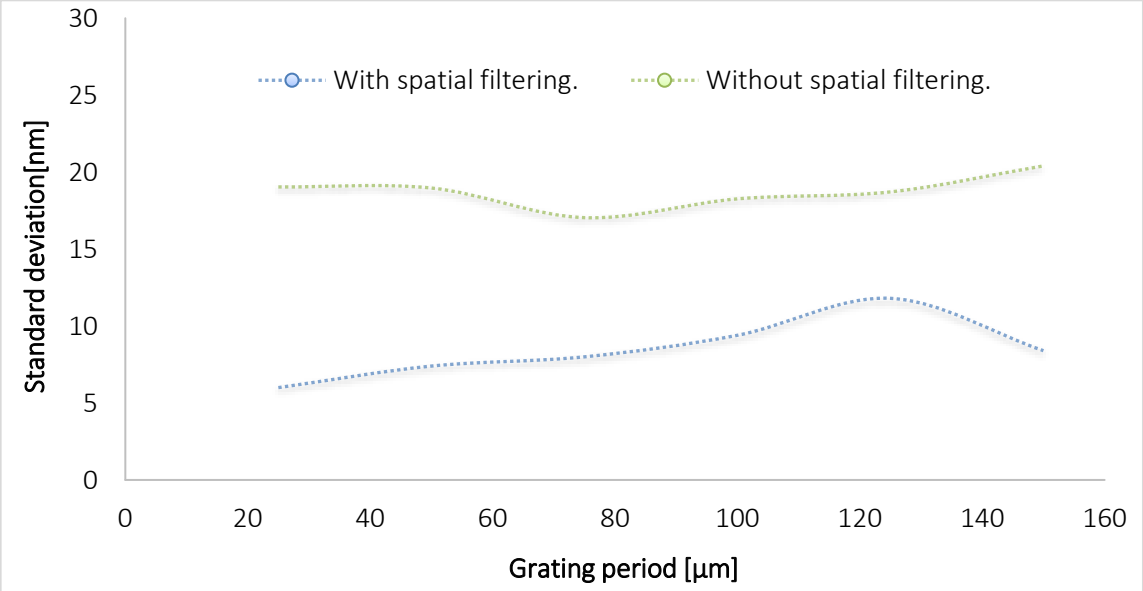

(d)

Fig.4.14 Influence of the grating period tolerance (5µm) on the wavefront reconstruction at a wavelength of 633nm and the propagation distance of 200µm. (a) peak-to-valley error, (b) standard deviation of the peak-to-valley, (c) RMS error, (d) standard deviation of the RMS error.

The wavefront reconstructions of the 50 test samples with the introduced grating period errors show good and relatively constant results (Fig.4.14). The sensitivity of wavefront reconstruction to grating period tolerance increases when the grating period decreases. The spatial filtering has a positive influence on the quality of the reconstruction.

The mean difference between filtering and no filtering at the grating period of 25µm is 15nm and at 150µm is almost 12nm. The filtering has also a positive influence on the development of the standard deviation as a function of the grating period. With spatial filtering, the standard deviation remains quite constant and reaches a maximum of 6.2nm. Without filtering, the standard deviation varies from 12nm to 22nm. The RMS analysis shows a constant functional behavior. However, the spatial filtering reduces the RMS value in average by 7nm compared to the error appearing without spatial filtering. The standard deviation remains relatively constant over the whole range of the grating period. It has been shown that the error evolution affects the wavefront reconstruction in the same manner for the whole range of grating periods. Constant standard deviation development is also observed. The influence of the grating period tolerance on the total error propagation Δy is simplified as in equation (4.3)

$$\Delta y = \sqrt{\left(-\frac{d_x}{2z\lambda\sqrt{{d_x}^2-\lambda^2}}\cdot\Delta d_x\right)^2} \approx \left(\frac{d_x}{2z\lambda\sqrt{{d_x}^2-\lambda^2}}\cdot\Delta d_x\right) \qquad (4.3)$$

Figure.4.15. shows the influence of the grating period error on the prefactor and the φ_t as a function of the grating period.

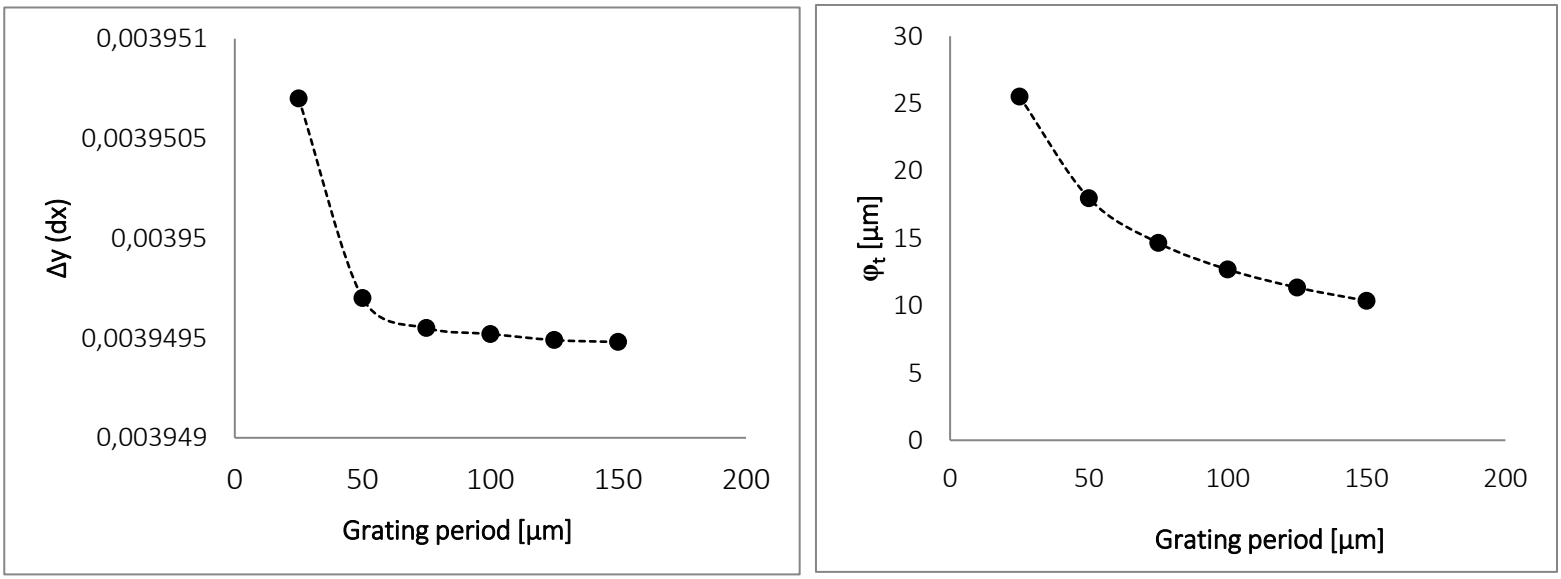

(a) (b)

Fig.4.15 Influence of the grating period error on the prefactor y (a) and the linear phase term φ_t (b) vs. grating period.

It is noteworthy that the φ_t decreases with increasing the grating period d_x. Likewise, the prefactor error is decreasing. Both error sources in the simulation become smaller as the grating period increases.

4.2.4 Simulation of the tolerance of axial position

For the derivation of the theory, different approximations were assumed. The axial position z plays also an important role.

However, the exact knowledge of the propagation position z behind the diffraction grating is desirable. The accuracy of this position depends on various parameters. For instance, the accuracy of the moving table, the exact position of the grating and the field depth of the imaging system. Simulation reveals the influence of the tolerance of the axial positions z on the overall accuracy of the system. We consider this at a wavelength of 633nm and a grating period of 50µm. The position z is simulated in increments of 40µm from 10µm to 1mm. At each position, simulations with 50 different free form samples are carried out. To each of these simulations, 5µm error is added. The exact moving table has a positional accuracy of 1µm, and the additional 4µm uncertainty comes from the inaccuracies in determining the position of the gratings relative to the imaging system. The results are shown in Fig. 4.16

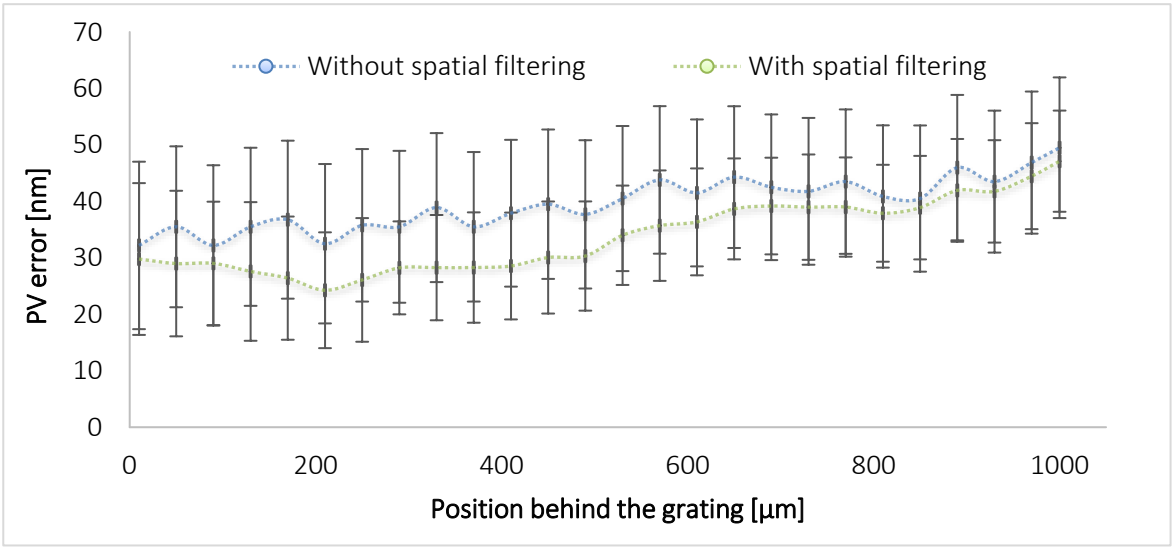

(a)

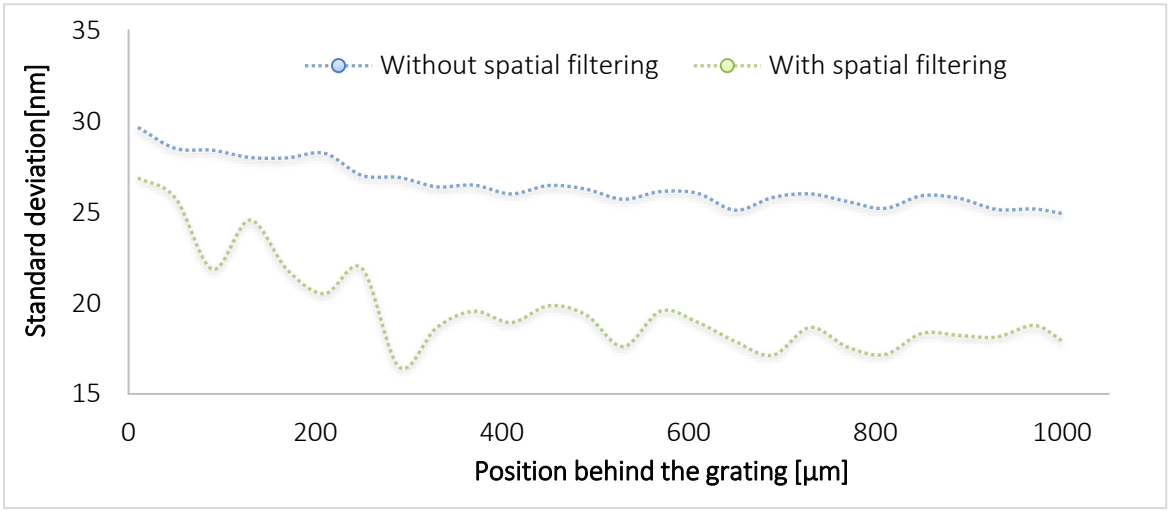

(b)

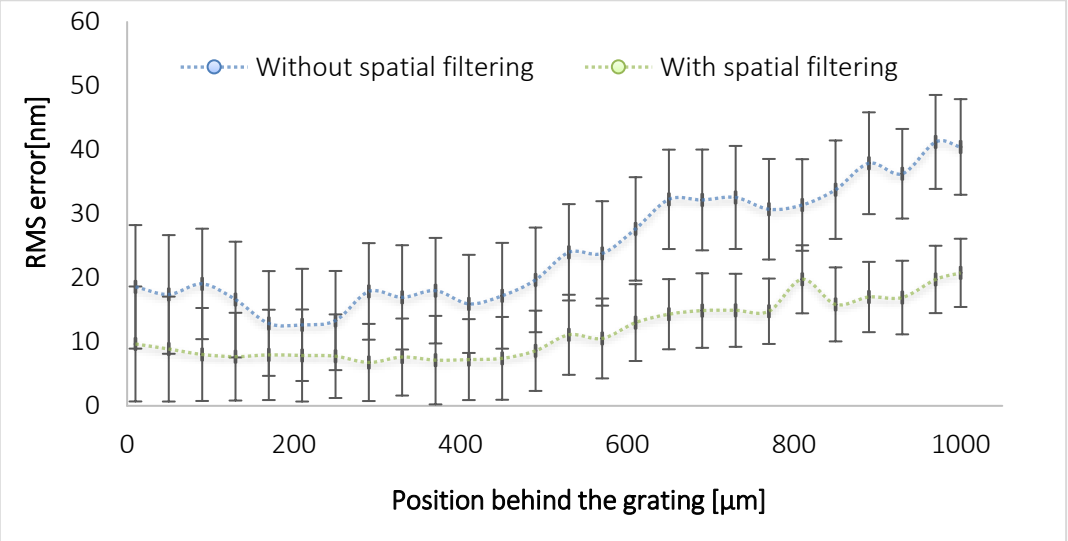

(c)

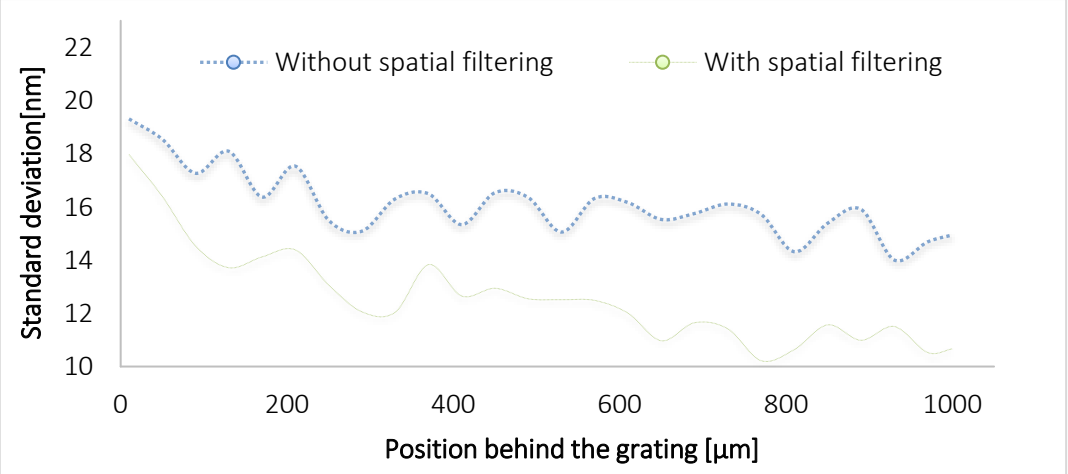

(d)

Fig.4.16 Influence of position tolerance (5µm) on wavefront reconstruction vs. axial position. (a) peak-to-valley error, (b) standard deviation of the PV error, (c) RMS error, (d) standard deviation of the RMS.

The analysis of the error influence in position z on the reconstruction of the wavefront as a function of the position behind the grating without filtering shows an increasing error with increasing the grating period. For the case with spatial filtering, this error decreases first then increases. At larger distances, the influence of the filtering on the quality of the reconstruction becomes minimal. The standard deviation becomes smaller with increasing axial position behind the grid; independent of the included or not included filtering. However, applied filtering, reduces significantly the error value. Similar behavior as in the PV analysis for the RMS curvature is observed. The influence of the position z tolerance on the total error propagation is simplified following the Eq.4.4:

$$\Delta y = \sqrt{\left(\frac{\sqrt{{d_x}^2-\lambda^2}}{2\lambda z^2} * \Delta z\right)^2} \approx \left(\frac{\sqrt{{d_x}^2-\lambda^2}}{2\lambda z^2} * \Delta z\right) \quad (4.4)$$

The following Figure shows the influence of the grating period error on the prefactor and the φ_t as a function of the position z behind the grating.

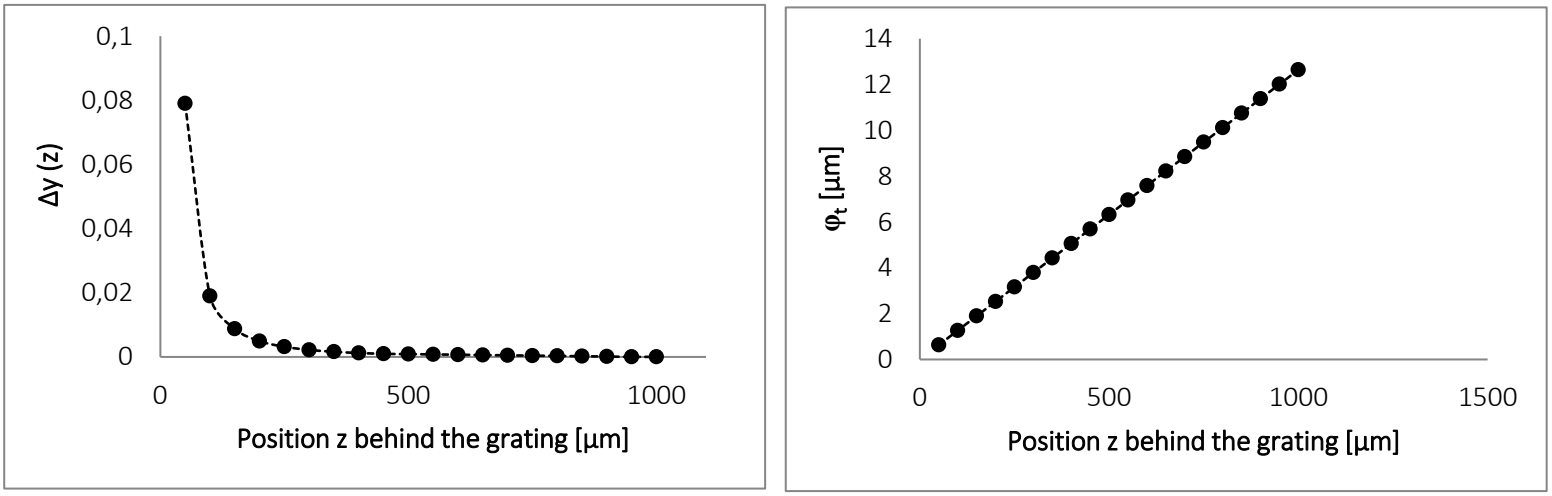

(a) (b)

Fig.4.17 (a) Influence of the grating period error (5µm) on the value of prefactor and (b) the linear phase term φ_t as a function of the position z behind the grating.

The explanation that the reconstruction of the PV error of the wavefront first decreases then increases is shown in Fig.4.17. The prefactor resulting from the tolerances of the position first decreases strongly then remains constant and minimal, while the function ϕ_t continuously increases as a function of the position z. The merging of these two errors has an identical course as PV difference to the original wavefront and indicates its dependency.

4.2.5 Simulation with simultaneous uncertainty of: position, gratings period and wavelength

The wavelength, the grating period and the position z are independent of each other. In an experimental environment, each of these parameters will never be 100% accurate. Therefore, it is important to perform a general simulation when each of these parameters delivers its individual error contribution. In this analysis, an additional arbitrary measurement error is added to all parameters. This simulation is important for demonstrating the total influence of this error combination on the accuracy of the measurement methods. For this simulation we choose a wavelength (633nm ±2.5nm), a grating period (50µm ±2.5µm) and a position z (50µm ±2.5µm) that relate to the tolerances in our coming experiments. For the statistical studies, the simulation was repeated with the 50 freeforms mentioned before. Additionally, intensity noise is introduced.

It turns out that the mean deviation to the given ideal wavefront equals to 86.9nm ±13.65nm and to 125.6nm ±25.32nm respectively without spatial filtering. Referring to the maximum height of 10µm of the free form samples, this corresponds respectively to a relative error of 0.7% ±0.01% with and of 1.1% ±0.02% without spatial filtering.

4.3 Summary

In this chapter, the proposed theory was confirmed by various simulations. For the statistical analysis several numerical freeform wavefronts with arbitrary gradients were generated. With this wavefront, the theory was first tested under ideal conditions. First, the quality of the gradient extraction was tested. Subsequently, the 2D wavefronts were reconstructed on the basis of these gradients and compared with the original ones. In the second part, the influence of the faulty main parameters on the quality of the reconstruction was investigated in order to be able to simulate close to the experimental environment. In order to evaluate the sensitivity of the measurements to those parameters, a noise source was added to the simulations. For the determination of these tolerances the worst case was assumed (larger than expected in the experimental environment), nevertheless the presented measurement method shows robust results.

V. Experimental

In the present chapter, our developed approach is experimentally tested on an example of transparent freeform. A commercial Shack Hartman Sensor (Optocraft SHS) is used as a reference tool for the confirmation of our measurements. In order to achieve reliable measurements using our method, it was necessary to develop an innovative grating element based on black silicon. Its fabrication is described in the first section. Two concepts of illumination sources are then characterized and compared with each other. Afterwards, an appropriate setup that combines our measurement with the reference measurement by the Shack Hartman Sensor is built up, in order to compare both wavefront reconstruction methods instantaneously. In the next step, a statistical analysis is performed in order to confirm both methods. With the intention to extend the measurement area of the sample, a stitching algorithm is introduced. Finally, our approach is expanded to the measurement of reflective samples and the validity of our experimental results is confirmed by comparing to Shack Hartman Sensor.

5.1 Experiment

In order to check the accuracy of the presented measurement method, different approaches exist. One of these is the use of a well-characterized test object. This measurement object must be characterized using a metrological method with a higher accuracy than the one of the tested methods. The challenge is that the test object must be integrated into the two different measurement setups and should be in the same position. This leads to an enormous effort in the adjustment and calibration. In the present work, a measurement setup is realized. In the latter, it is possible to compare directly under the same conditions the introduced measuring system with an established measuring method. At the same time, the influence of different parameters on the accuracy can be simultaneously investigated. In this context, the proposed theory is compared with a conventional Shack-Hartmann wavefront sensor. Both test methods should be exactly coordinated and aligned. After adjustment, the optical freeform sample is positioned and tested. Thereafter, the repeatability and the reproducibility of the measurement method are examined. Afterwards the measurement setup is adjusted to measure a specular free form. At the beginning the test freeform object is introduced. Subsequently, the production and characterization of the important diffraction grating will be shown. At the end, the experimental setups and the statistical investigations in reflection and transmission will be presented.

5.1.1 Freeform

The presented theory is experimentally tested using the example of a freeform wavefront generated by a phase plate Fig.5.1. The profile is described by a seventh-order polynomial with maximum sag of 1.119mm.

It has been fabricated on PMMA by ultraprecision machining at the the Institute of Micro and Nanotechnologies (IMN) at Technische Universität Ilmenau [154,155]

.

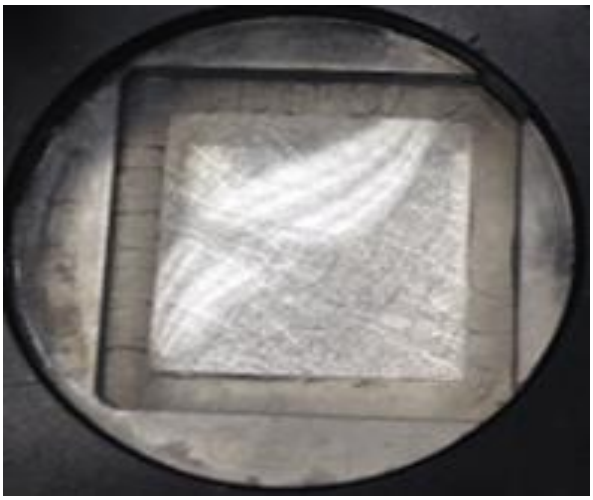

Fig.5.1 Freeform surface (Phase plate) [154].

5.1.2 Black Silicon amplitude grating

The most important and innovative element of the presented measurement method is the diffractive element. For the present work, different binary gratings with different surface properties were produced, characterized and tested. These gratings differ from the materials, the manufacturing methods and the surface reflectance. The conventional chrome coated binary gratings have nearly 100% reflections at chromium areas [156]. These unwanted reflexes introduce strong disturbances on the measurement accuracy of both methods. These perturbations have been described in more details in chapter (3.4.3). In order to avoid/ suppress these reflections, a black silicon binary grating as illustrated in Fig.5.2 has been fabricated.

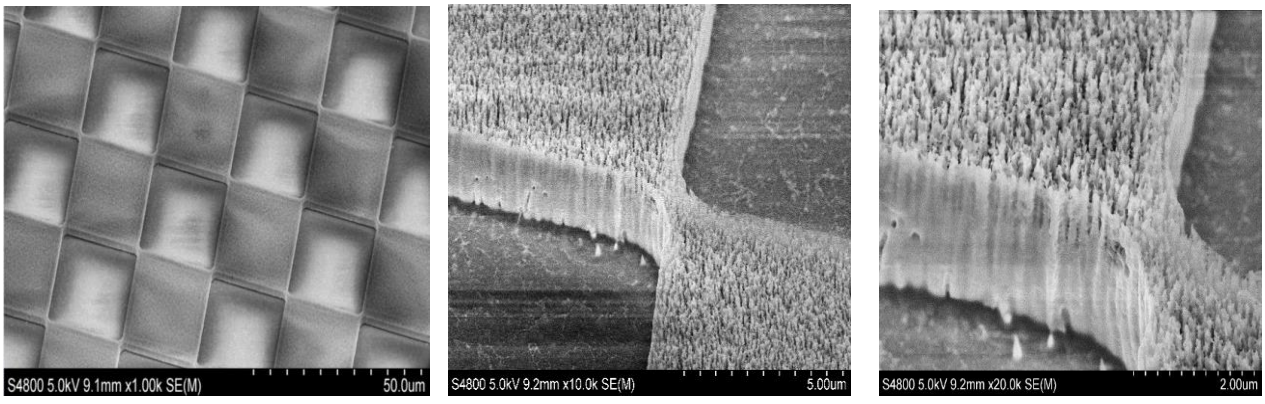

Fig 5.2 Cross grating structure based on black silicon on glass wafer at different magnifications.

The black silicon amplitude grating is a two-dimensional binary diffractive grating based on nanostructured silicon [157-160] and is fabricated by means of lithography at the Institute of Micro- and Nanotechnologies at TU Ilmenau. The achievement of this structure component is challenging and not a standard process yet. Therefore, the applied method to integrate the silicon grass antireflection structures into a glass-wafer is described. Afterwards, the grating is characterized. The process sequence is shown in Fig.5.3. In the sub-chapters "manufacturing process of the diffractive grating 5.1.1.2 to 5.1.2.8", it is clearly stated that all production steps were carried out by the Institute of Micro- and Nanotechnologies of the TU Ilmenau. The design of the lithographical amplitude mask and the characterization of the diffractive element were performed by my person.

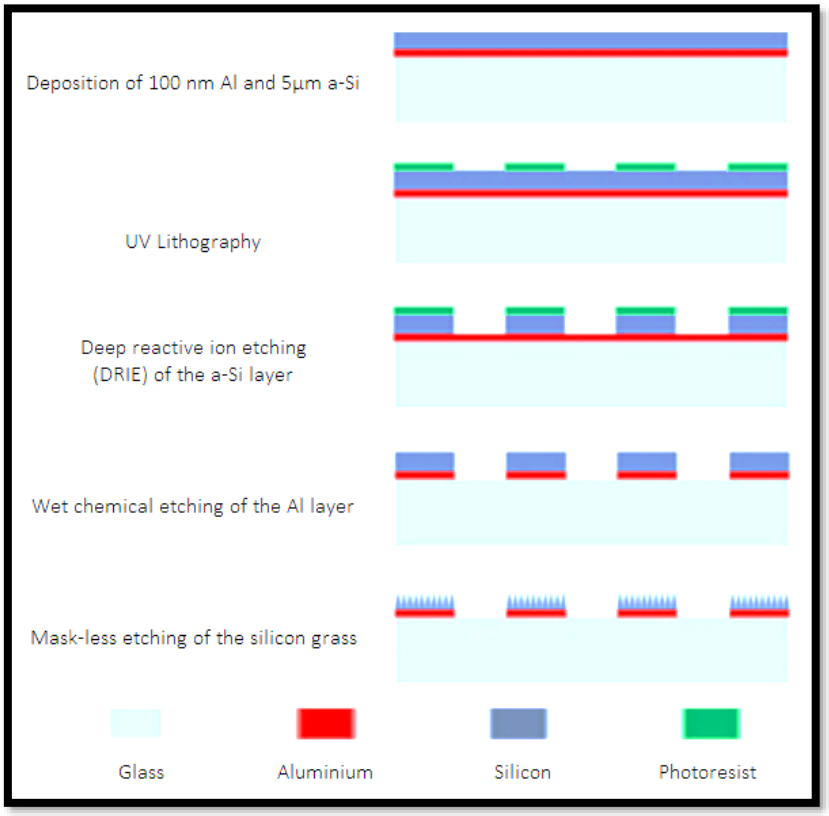

Fig.5.3 Process sequence for the diffractive grating pattern with antireflective silicon grass layer.

5.1.2.1 Lithographical amplitude mask

The used gratings are lithographically produced. For the fabrication, a mask is needed. Therefore, a chrome mask is designed and produced. On this mask, binary structures with different grating periods (12.5µm, 25µm and 50µm) are designed. When measuring and characterizing the produced masks, a maximum deviation of 0.25µm in the grating periods is registered. It is also found that the corners between transparent and opaque surfaces are not connected. This error can be seen in Fig.5.4. This gap is nearly 0.15µm.

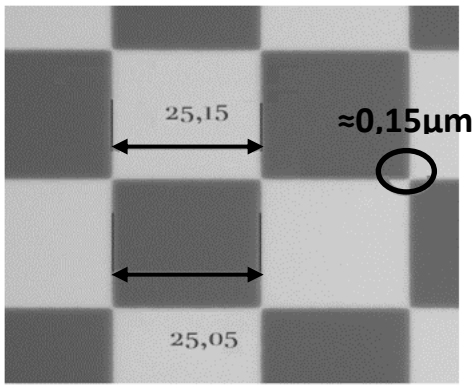

Fig.5.4 Characterization of the lithographical amplitude Mask.

After the preparation and characterization of the mask, different steps are carried out in order to fabricate the diffractive grating.

5.1.2.2 Cleaning

An important step in the production procedure is ensuring that the glass substrates are clean. In the case of an organically contaminated or particle-contaminated glass substrate, two-stage cleaning process is recommended to improve the coating wetting and adhesion. First, acetone is used to remove the organic impurities followed by isopropanol that removes contaminated acetone. During this procedure, it is recommended to use a vibrator. Due to the constant movement of the solution (acetone or isopropanol) paint residues, if present, are better solved or removed. If the surface had foreign substances such as metal ions, conventional chemical treatments are insufficient. Since these contaminants can have a great influence on subsequent processes, such as etching or coating processes, plasma cleaning is carried out. Due to the high energy level of the plasma, various impurities can be disrupted in their structure. In our case, the wafer is processed for 2 minutes with argon and tetrafluoromethane gases. Before the wafer surface is treated with argon and tetrafluoromethane, conditioning with these gases must be performed. This ensures pure plasma with the desired gases. If the chamber is contaminated by other processes, oxygen cleaning is carried out before the conditioning.

5.1.2.3 Metallization

The first step after the basic cleaning of the wafer, is the full-surface coating with aluminum on the front of the wafer. Since amorphous silicon transmits parts of the light spectrum in the range of 4-6µm, the aluminum layer serves as a transmission barrier starting from a thickness of 80nm. In addition, it facilitates the transfer of the wafer into the RIE system. Indeed, the sensor that measures the presence and the thickness of a wafer and glass does not send back enough information. The metallization process used is vapor deposition. Indeed, aluminum is heated below the wafer under high vacuum by an electric heater. The resulting vapor settles on the substrate, layer by layer. After metallization, the wafer is cleaned with deionized water and placed in the oven at 105°C for 30 minutes.

5.1.2.4 Amorphous silicon coating

In order to grow an amorphous silicon layer, an ICP-CVD (Inductively Coupled Plasma Chemical Vapor Deposition) process or LPCVD (low pressure chemical vapor deposition) process is required. The radicals and ions generated in this way, with their interaction, favor a layer deposition on the substrate.

5.1.2.5 Lithography

After the repeated chemical cleaning process with acetone, isopropanol and DI-water, the wafers are heated for at least 30 minutes at 105°C in the oven. The still adherent water molecules on the surface of the clean substrate will disappear by annealing. Depending on the relative humidity, a water film may appear on the substrate surface after few minutes. Therefore, subsequent coating should be possible soon after heating. To improve adhesion, it is necessary to use HMDS (hexamethyldisilazane). This is done through the gas phase using an HMDS hot plate at 95°C.

- ✓ Resist AZ 9260

The Resist AZ 9260 is a positive resist, which has an even lower optical absorption compared to other resists, such as the AZ 4500, which facilitates the exposure of very thick resist layers. AZ 9260 requires a higher exposure dose and has a low development rate.

- ✓ Developer

For the AZ 9260, the MIF 726, AZ Developer 1:1 or the AZ 400K 1:4 is recommended as the developer medium. In these experiments, the MIF 826 is used because it has a lower dark erosion. For coating thicknesses of more than 10µm, the AZ 400K can be diluted in a ratio of 1:3.5 or 1:3. The higher concentration shortens the development time and favors the process. For our sequence, the undiluted developer AZ Dev is used. The AZ MIF 726 as well as the AZ 400K etch the amorphous Si layer as well as the aluminum. In addition, the development revealed a strong reaction of the coatings with the two developers to a white non-removable layer. The reason could be among others the H_2/H_2O ingredient in AZ MIF and AZ400K.

5.1.2.6 Dry chemical etching

The generated mask structure is now transmitted via a dry-chemical etching process. Since the layer is 6µm thick, it needs a special etching process, the so-called Bosch process. By additionally passivating the sidewalls between the etch sections, larger etch depths with steep walls and good aspect ratios can be achieved. This is ideal for our amplitude grating, which needs a good structural integrity. The STS Flour Machine (Oxford) located in the Institute for Micro- and Nanotechnology MacroNano® in Ilmenau is used. After the process, the resist is only poorly solved using the standard AZ 100 remover, as well as the AZ P1316 power stripper. In fact, this is due to the etching process itself, as well as the previous problems of development and wise layering. Therefore, the resist mask is ashed by oxygen plasma.

5.1.2.7 Wet chemical etching

After patterning the amorphous silicon layer, the aluminum layer is wet chemically etched at the silicon-free position. In this case, the amorphous Si serves as a mask. Removing aluminum requires a mixture of chemicals. The so-called aluminum etcher consists of hydrogen, nitric acid, phosphoric acid and acetic acid. The nitric acid oxidizes the aluminum, which dissolves the phosphoric acid. The acetic acid buffers the nitric acid and supports the wetting as well. The mixed water adjusts the etch rate at a given temperature. Since the Al etching has a strong exothermic character, it is also strongly isotropic. Therefore, a permanent control during the process is necessary.

5.1.2.8 Saws

Before separating the given fields on the wafer, a protective varnish must be applied. The resulting dirtiness in the process (cooling water and sawdust) would contaminate the structures and make them useless at the same time. For this purpose, the AZ 1518 is used. The sawing process begins by stretching an adhesive film onto a frame. The wafer is then positioned on this film. Before attaching the device to the machine, the appropriate saw blade must be clamped. It is important then to define which material should be sawed with which thickness. In this case, a sheet for glass (fused silica) with a width of 150µm is selected. The resulting sawing on the wafer is approximately 300µm, which has to be considered in the layout. The cutting is done from saw line to another. After the sawing process, the individual parts are cleaned in the following order "Remover - DI-water - Acetone - Isopropanol - DI-water".

5.1.2.9 Geometrical properties

When measuring and characterizing the black silicon grating, a maximum deviation to the ideal grating periods of 0.4µm is observed (see Fig.6.17 left). It is also found that the corners between transparent and opaque surfaces are not separated. This error can be seen in Fig.5.5 right. The gap is nearly 0.6µm.

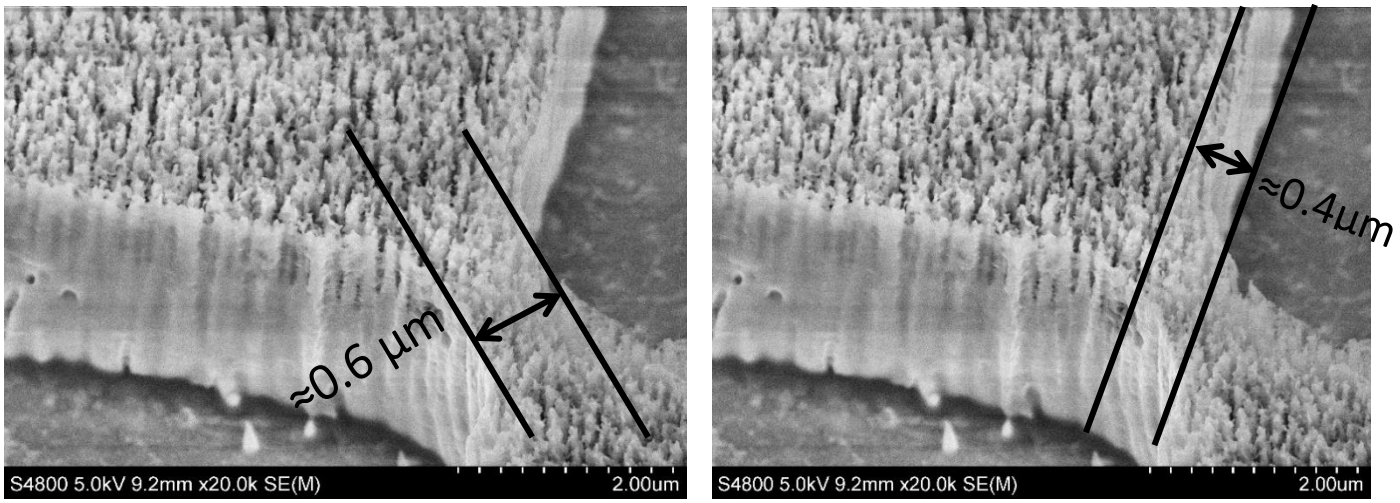

Fig.5.5 Incorrect geometry at adjacent structures. A connection between subsequent structure elements is remaining.

5.1.2.10 Reflective properties

For the spectral distribution of the reflective properties, the specular and the hemispherical spectral reflectance of the micro-structured silicon grass surface are measured. The measurements were conducted by dispersive spectroscopy (Cary 5000 from Varian) using the absolute specular reflectance accessory and an integrating sphere (internal DRA 2500). The zero and baseline calibration are carefully performed. Fig.5.6 shows the measured results for specular and hemispherical relative spectral reflectance of the presented silicon grass on top of the Al layer.

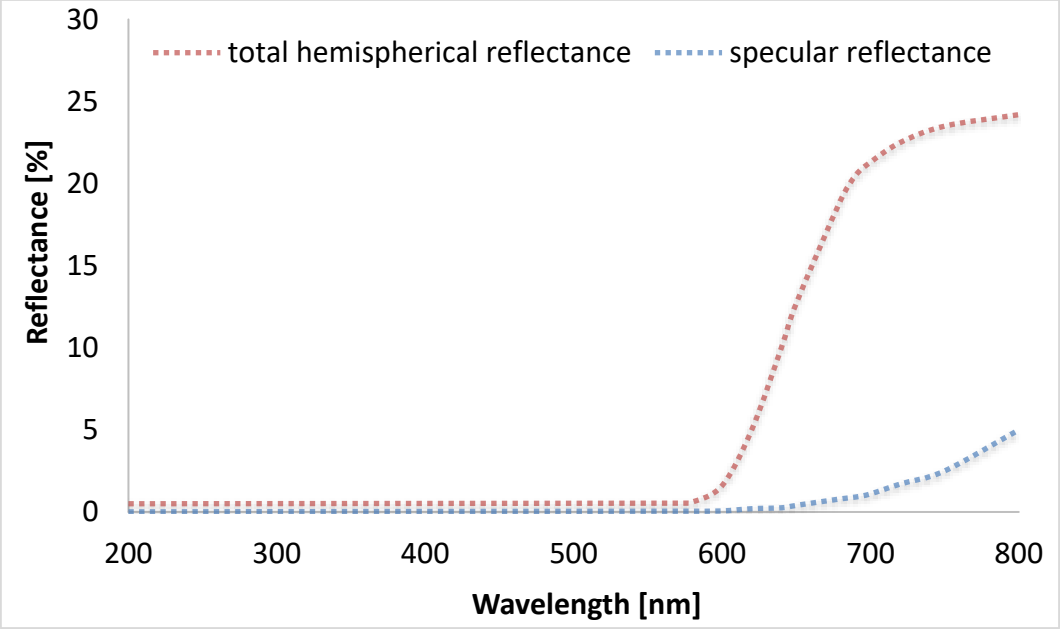

Fig.5.6 Relative specular and hemispherical spectral reflectance of the silicon grass.

The biggest difference between a silicon wafer and an a-Si layer is the thickness of the optically effective silicon. Regarding a silicon wafer with several hundreds of microns in thickness, the silicon grass structure acts as the anti-reflective surface structure and nearly the whole radiation is coupled into the bulk silicon. The silicon itself absorbs the radiation of a wavelength below nearly 1100nm, which corresponds to its band gap close to 1.1eV. The absorbance of the silicon depends on the wavelength: the longer the wavelength is, the lower the absorption becomes. This explains the measured behaviour of the silicon grass: For the larger wavelengths, the a-Si layer is not thick enough to absorb all the radiation. The latter is reflected at the Al layer and leads to the relatively high reflectance for wavelength longer than 650nm. Due to the scattering characteristics of the silicon microstructures, the total hemispherical reflectance is significantly higher than the specular reflectance. For the presented application, only the specular reflectance is relevant. At the desired wavelength (633nm), the total specular reflectance of the black fields of the checkerboard pattern is smaller than 0.3%. In the following, the grating is tested and implemented in the experimental setup with the aim to demonstrate how well the black silicon grating performs to reduce the unwanted reflexes (Fig.5.7).

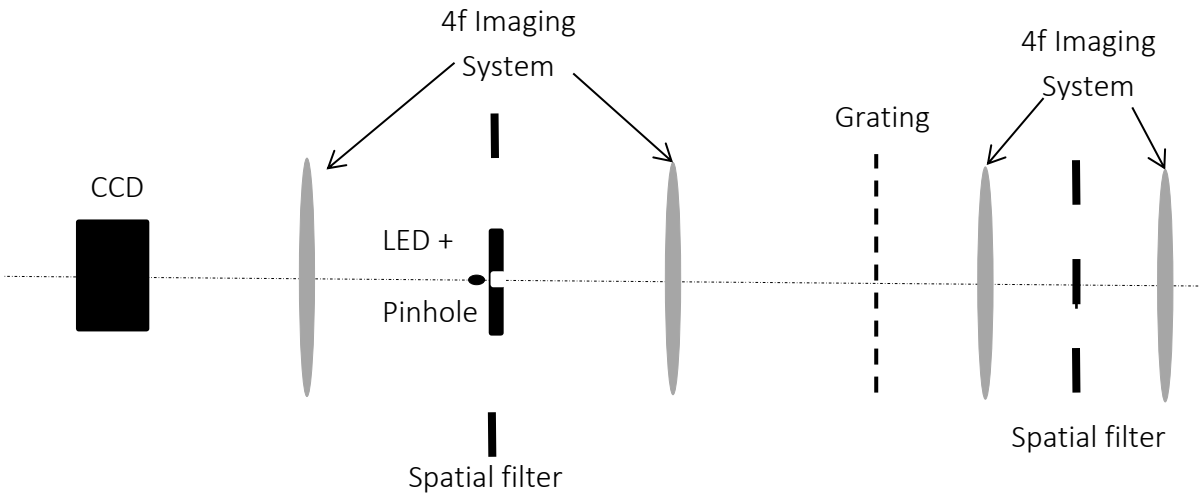

Fig.5.7 Scheme of the setup for characterizing the grating based on black silicon.

The presented setup is suitable for both reflection and transmission measurements. It consists of two 4f imaging systems, a CCD camera, a pinhole LED and two spatial filters. These arrangements were experimentally set up in the laboratory with two different diffraction gratings: The first grating is conventionally made of chrome. For the second one, the black silicon grating is used. Both are manufactured at the Institute of Micro- and Nanotechnologies at TU Ilmenau and have a grating period of 50µm. They are likewise illuminated with the identical LED at the same power. The identical intensity distributions are captured with the same settings of the monochrome CCD camera (uEye UI-1240SE, IDS Imaging Development Systems GmbH), especially the exposure time. The sample is taken out to measure only the direct reflections from the chromium or the black silicon gratings (Fig.5.8). These unwanted light reflections represent the background noise and thus should be as small as possible. For both gratings the histograms of intensity are extracted (Fig.5.8 c, d). The number of counts is normalized to the same maximal value. We clearly see that the use of the black silicon grating causes significantly lower reflections than the chromium grating. This corresponds to our expectations.

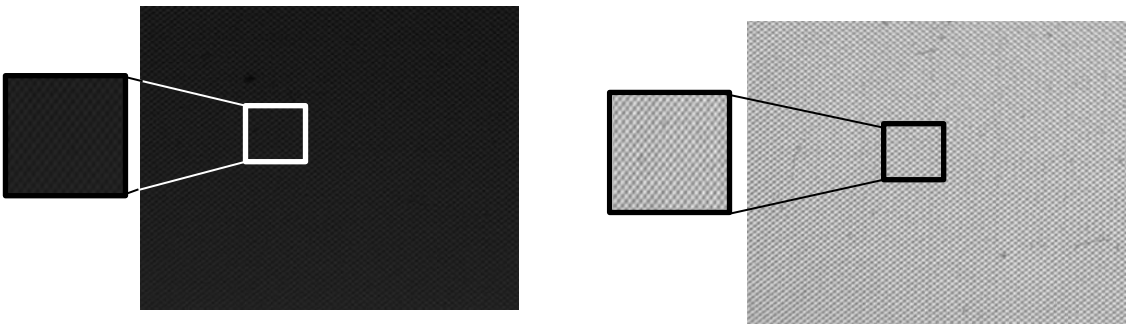

(a) (b)

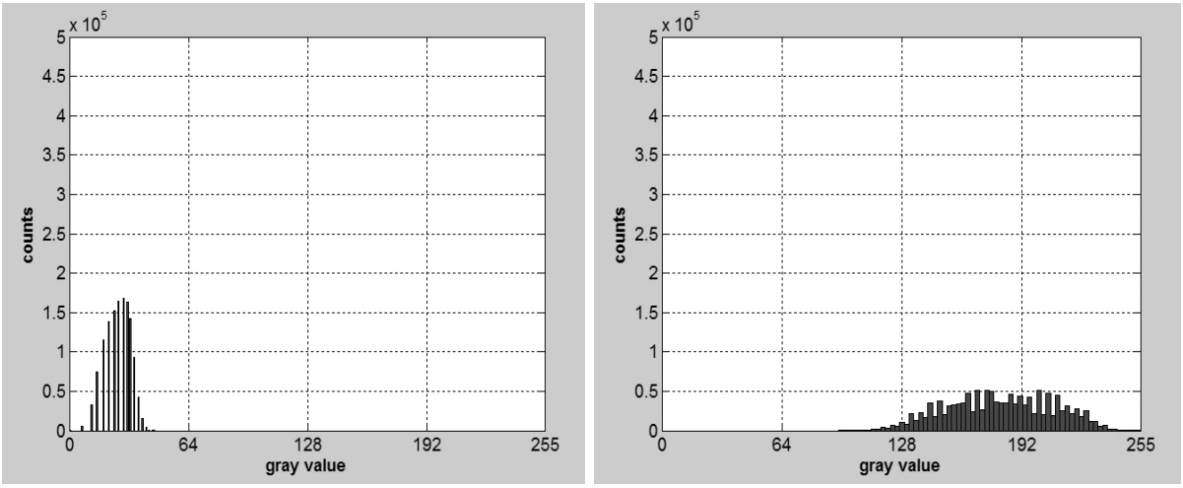

(c) (d)

Fig.5.8 Captured images using (a) black silicon grating and (b) chromium grating; histograms of the intensity of captured images using (c) black silicon grating and (d) chromium grating.

5.2 Experimental Setup for transmission

5.2.1 Setup

The schematic setup for the experimental validation of the presented theory in transmission is shown in Fig.5.9. The used illumination consists of a partially coherent illumination with the wavelength of 632nm and a pinhole with 50µm diameter. Both elements are in the focal plane of a lens with a focal length of 80mm. The resulting collimated beam illuminates the freeform under test. The subsequently generated wavefront contains the information about the wavefront caused by the freeform.

In case of a freeform with a gradient exceeding the dynamic range of our measurement method or of the commercial Optocraft SHS, a 4f system with Fourier-filtering is used to transmit only

the maximal possible frequency to validate the Nyquist criteria for our application while not exceeding the maximum dynamic range of the SHS. This filtering plays an important role in adapting the measurement setup to allow measurement of specular surfaces.

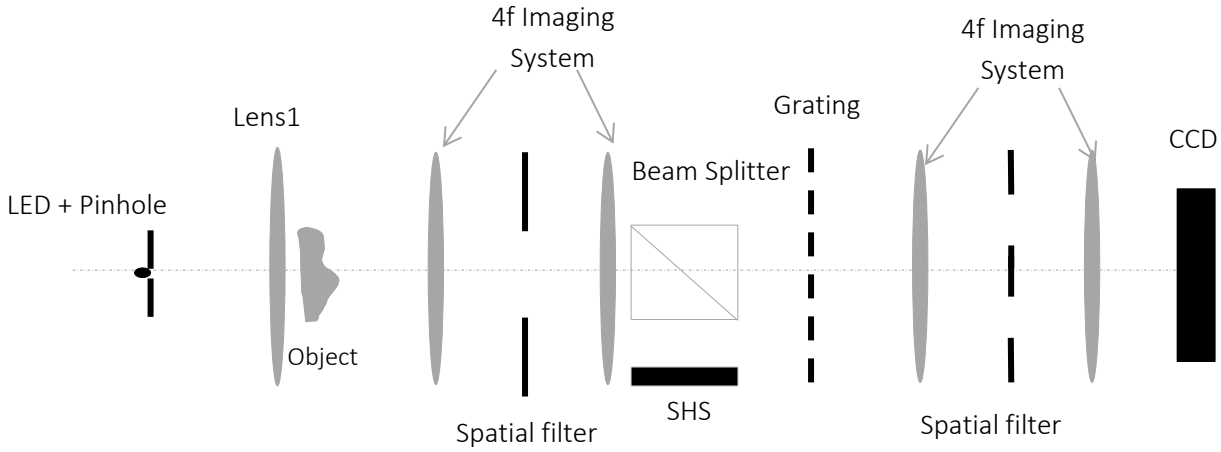

Fig.5.9 Schematic of the Experimental investigation.

Using a beam splitter, the propagated wavefront is divided into two identical parts: The first part is deflected to the SHS, the second one will be propagated to the used grating. Our intention is to set both path lengths (sample – SHS, sample – grating) to equal path lengths in order to compare these two measurement principles. The grating and the SHS are aligned with best possible precision. The grating is placed at the distance z in front of the focal plane of a 4f system. This system contains two similar achromats with a focal length of 80mm. With this system, the intensity distribution behind the grating is imaged onto a CCD U-eye camera having a resolution of 1280x1024 pixels and a pixel size of 5.2µm. In the Fourier plane of the 4f system, a filter is placed, allowing then only the $\pm 1^{st}$ diffraction orders to pass. The 4f system, the Fourier filter and the CCD Camera are mounted on a precision linear stage with an accuracy of 1µm.

5.2.2 Results

First, let´s consider the axial position of the image plane behind the grating. In order to experimentally determine the influence of this propagation distance on the results of the wavefront reconstruction using our proposed method, series of measurements were carried out with and without spatial filtering. The distances behind the grating used for those experiments are from 50µm to 1mm. For each measurement, the wavefront of the freeform was measured simultaneously with the SHS. To perform a comparative statistical analysis, these experiments were performed ten times at each position.

Figure 5.10 shows an example of the intensity distribution at the position 200µm behind the diffractive element in the cases with and without spatial filtering. This position does not

correspond to a fractional Talbot distance. Using spatial filtering, the structure of the grating can be recognized in the intensity distribution (first line in Fig.5.10, right). In contrast to the case without spatial filtering (left), only the grating structure can hardly be recognized. This effect is to be expected because the complete self-image of the grid appears only in fractional Talbot distances. The result of the Fourier transform of the detected intensities is shown in second line in Fig.5.10. The distributions in the spectral domain underlines the positive influence of spatial filtering on the separation of spectral orders of intensities: The reduced number of spectral replica due to spatial filtering offers sufficient space to perform a clean filtering. This appropriate suppression of unused spectral replica reduces the chance of overlapping as well as the level of noise. The upper replica in y direction (corresponding to $\tilde{I}_{0,2}$) and the right replica in x direction (corresponding to $\tilde{I}_{2,0}$) are selected. After the shifting, the spectral replicas to the origin, the x and y gradients are extracted as mentioned in chapter 3. In this example and at this position, it can be observed that the extracted gradients are wrapped and the selected unwrapping algorithm must be used (see third and fourth line in Fig.5.10). After the unwrapping, the 2D integration has to be performed. The Frankot-Shelappa algorithm [146] delivers the final result of wavefront shapes which are illustrated in Fig.5.11 for the case without (left) and with included spatial filtering (right).

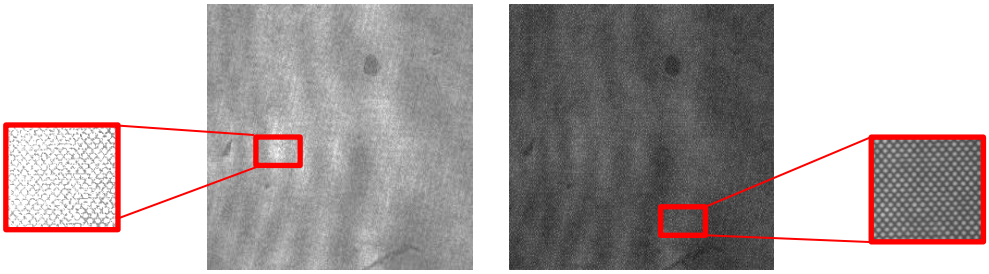

Intensity Distribution

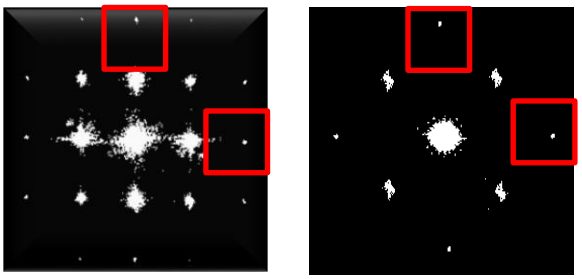

Intensity Distribution and extraction of required sub spectra

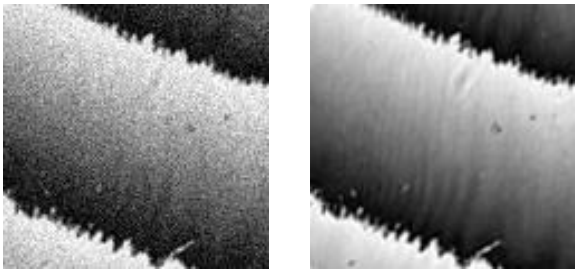

Extraction of x gradient

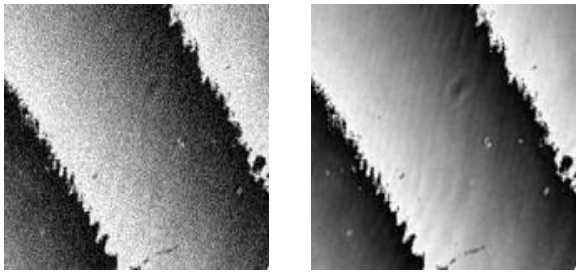

Extraction of y gradient

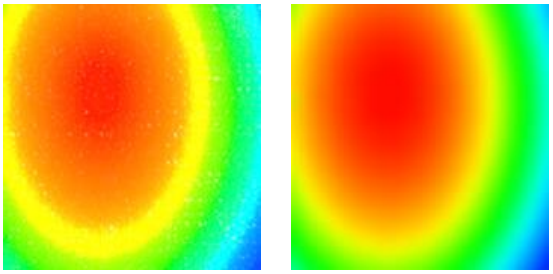

2D Integration

Fig.5.10 Steps of wavefront reconstruction at a propagation distance of 200µm behind the grating without (left) and with included spatial filtering (right), respectively.

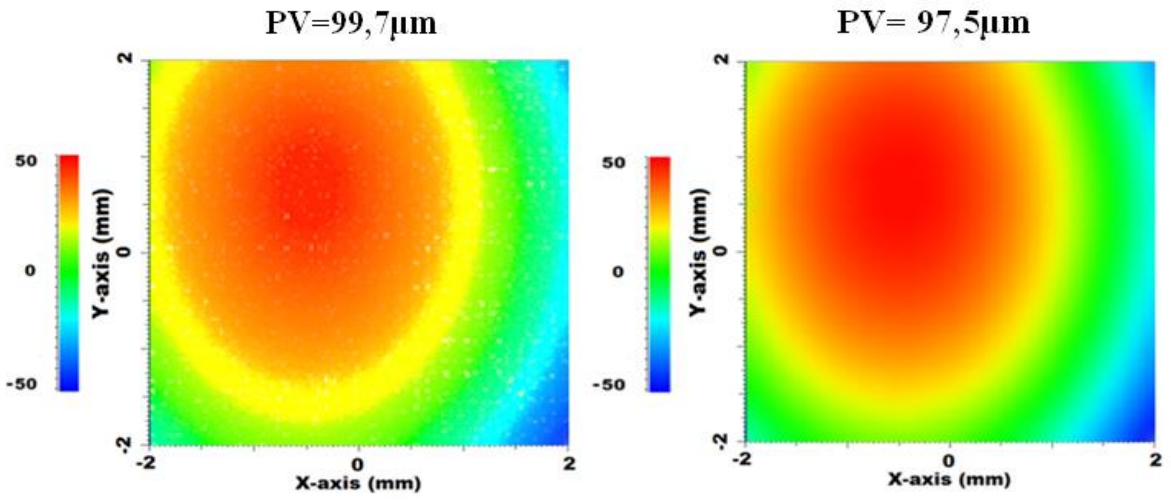

Fig 5.11 The final 2D wavefront for the case without (a) and with included spatial filtering (b).

Fig.5.12 shows the reconstructed wavefront from the SHS without image-processing by its application software. The resolution of this array of raw data is much lower (53 x 53 data points) compared to the used CCD camera in our method (1280 x 1024 pixels). In order to perform a point-by-point comparison to the presented measurement method, the number of SHS data has to be adapted to our data number by a numerical interpolation. For this, each data point from SHS is added to the next and then divided by two. This creates a virtual data point. This process is performed until our measurement method and SHS have the same data point. Then, a subtraction of the wavefronts is possible and will be performed.

The point-to-point differences to our measuring methods with and without spatial filtering are shown in Fig.5.13.

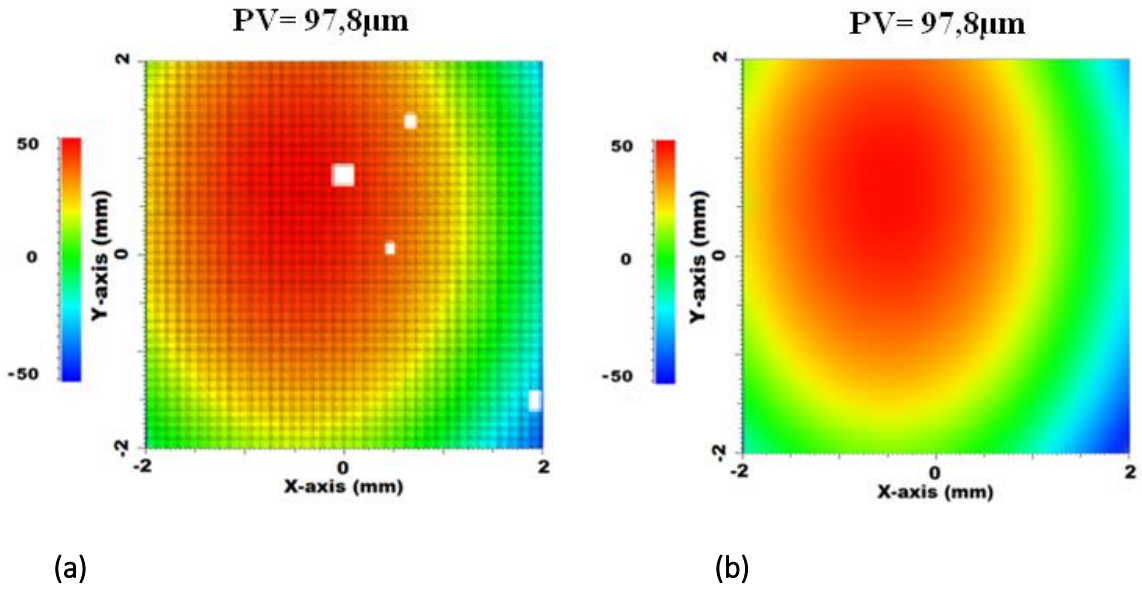

Fig 5.12 Reconstructed wavefront resulting from Shack-Hartmann Sensor (a) and after Image processing (b).

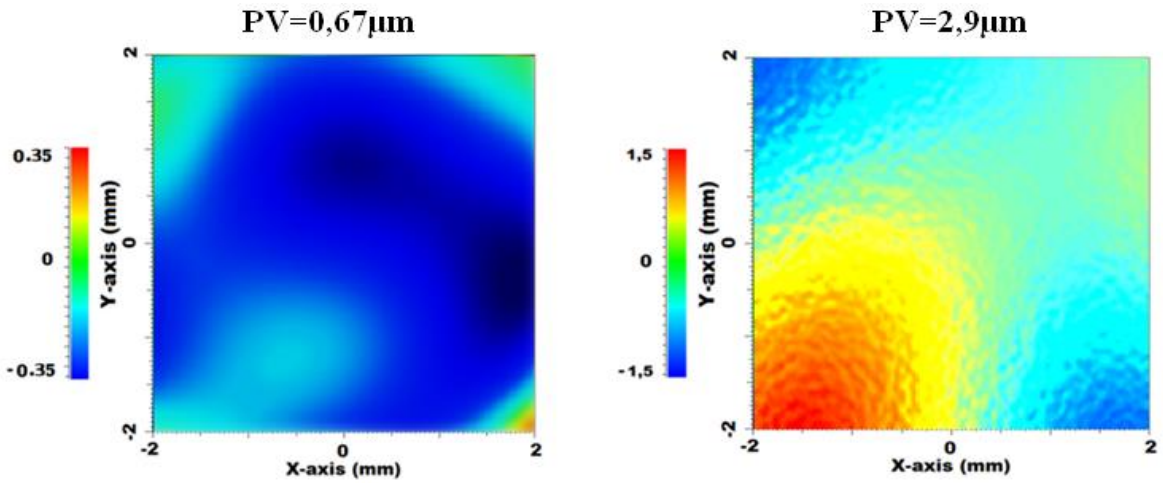

(a) (b)

Fig5.13 Difference of reconstructed wavefronts from Shack-Hartman Sensor and our measurement. Aliasing occurs without spatial filtering (b) and is cancelled if spatial filtering is performed (a).

The Fig.5.13 demonstrates the difference between the Shack Hartman Sensor and our measurement and processing. Artifact of higher frequencies are observed. This is due to aliasing if a spatial filtering is not applied. This is mainly because the spectral replica cannot be separated properly. Therefore, aliasing occurs. When spatial filtering is applied, this artifact effect is suppressed and the PV of the error between the measurement methods reduces from 2.9µm to 0.67µm.

- **Repeatability**

To demonstrate the repeatability of the presented theory, an experimental test has been performed by subtracting two consecutive measurements without any nominal change in the system. This provides information about the sensitivity of the setup to vibration, temperature and other noise sources. The experimental repeatability using the freeform surface is 4,8nm (PV) and 1,8nm (RMS) as shown in Fig.5.14.

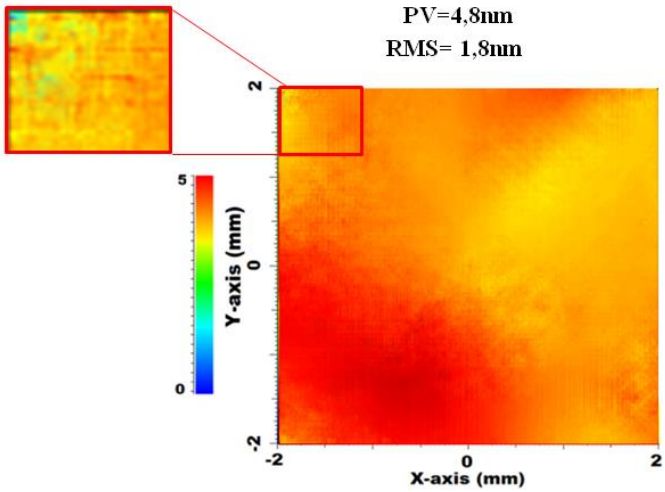

Fig.5.14 Repeatability of the measurement method: Difference between two consecutive measurements without any nominal change in the system.

- Statistical evaluations with the same wavefront

To illustrate the statistical evaluations of the experiment and to emphasize the influence of the propagation distance on the experimental results, the difference between the two measurement methods is shown in Fig.6.15 and Fig.6.16.

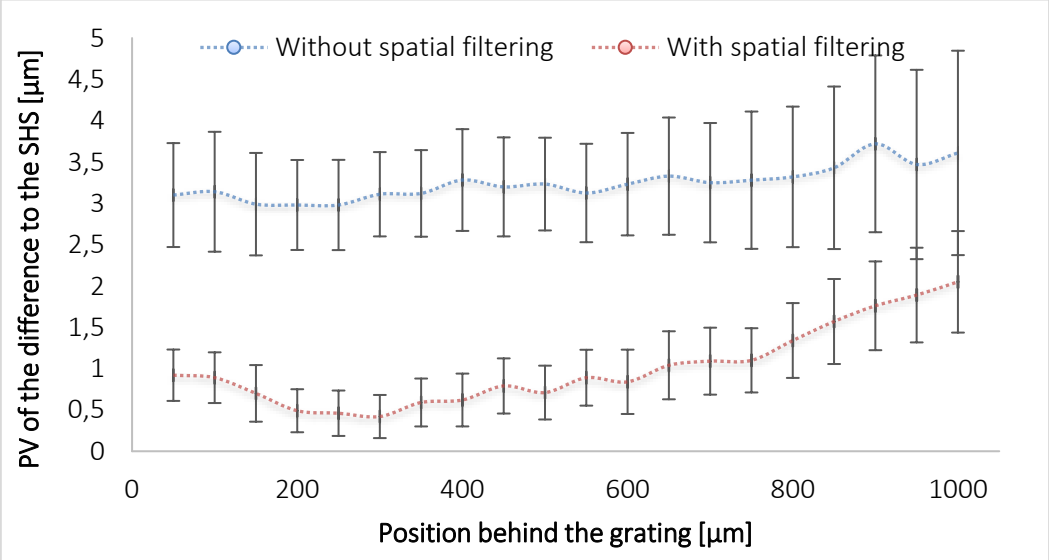

Fig.5.15 Peak-to-valley difference of reconstructed wavefront based on measurements of Shack Hartman Sensor and our method vs. propagation distance.

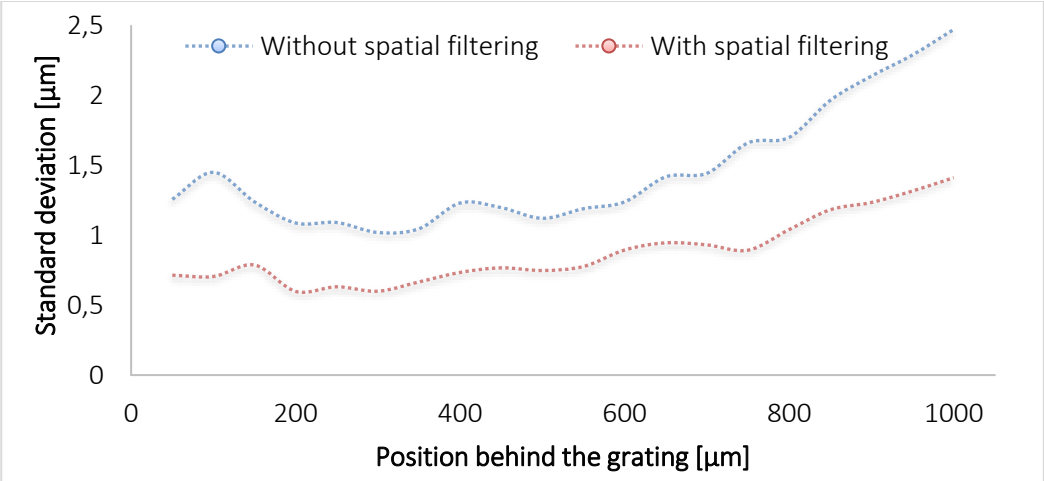

Fig.5.16 Standard deviation of difference of reconstructed wavefront based on measurements of Shack Hartman Sensor and our method vs. propagation distance.

When analyzing the course of the difference in the case of spatial filtering, a similarity in terms of the simulation is noticed. The error values are much higher than in the simulation. In the propagation position of 50µm the peak-to-valley difference to the SHS is 920nm. Up to the position of 300µm behind the grating, the error initially decreases to 420nm, and then increases continuously. At the position of 1mm behind the grid, the error grows to 2.05µm. In the case without spatial filtering, the error increases continuously with increasing the propagation distance. However, the values are higher than in the case without spatial filtering. At the propagation position of 50µm the difference to the SHS is 3.1µm and is equal to 3.61 µm at the position of 1mm behind the grating. The standard deviation of difference of reconstructed wavefront based on measurements of Shack Hartman Sensor and our method depending on the propagation distance have the same course as the error between both measurement methods Figure.5.17 and Figure.5.18 exhibit the development of the RMS and the standard deviations of the difference between both measurement methods with and without spatial filtering, respectively.

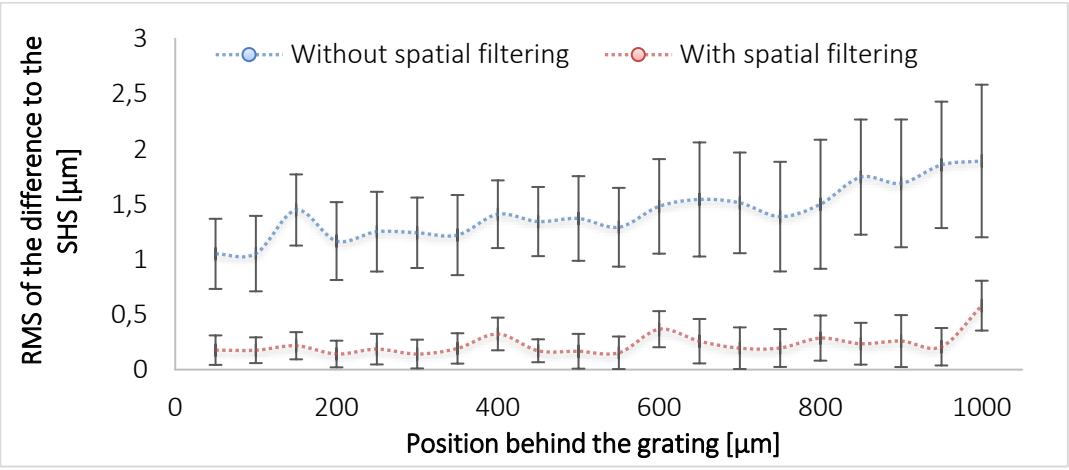

Fig.5.17 RMS of the difference between the reconstructed wavefront based on measurements of Shack Hartman Sensor and our method vs. propagation distance.

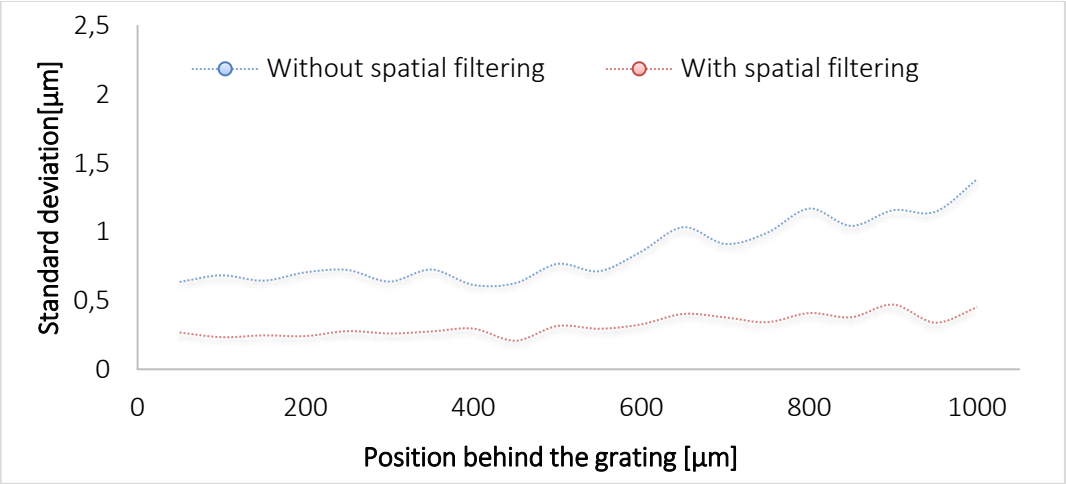

Fig.5.18 Standard deviation of the RMS of the difference between the reconstructed wavefront based on measurements of Shack Hartman Sensor and our method vs. propagation distance.

The analysis of these curvatures shows that the spatial filtering also reduces the RMS value. For spatial filtering, the RMS value remains almost constant over the entire distance behind the grating and averages 0.17µm. Without spatial filtering this value increases continuously with increasing distance z behind the amplitude grating. The error at the position of 50µm is 1.04µm. This is six times larger compared to the measurements with spatial filtering. At 1mm behind the grating, this error is 1.8µm in the case without and only 0.5µm including the spatial filtering, respectively.

➢ Statistical analysis of the reconstruction of arbitrary wavefronts

In the present experimental part, the lateral position of the test freeform element was changed five times without changing the respective optical element or the position of the grating with respect to the imaging system. This change is arbitrarily and creates a new wavefront with new properties. The aim of this step is to influence the shape of the test object to highlight the quality of the experimental results on several freeform wavefronts. Fig.5.19 shows the examples of 3 wavefronts reconstructed at 3 different lateral positions of the freeform. With each new position of the freeform, measurements are simultaneously performed using our measurement method and the SHS. For our measurement method, the distances behind the grating increase from 50µm to 1mm with 50µm steps. For each of these positions, the difference between the two measurements methods is then calculated (fig5.21).

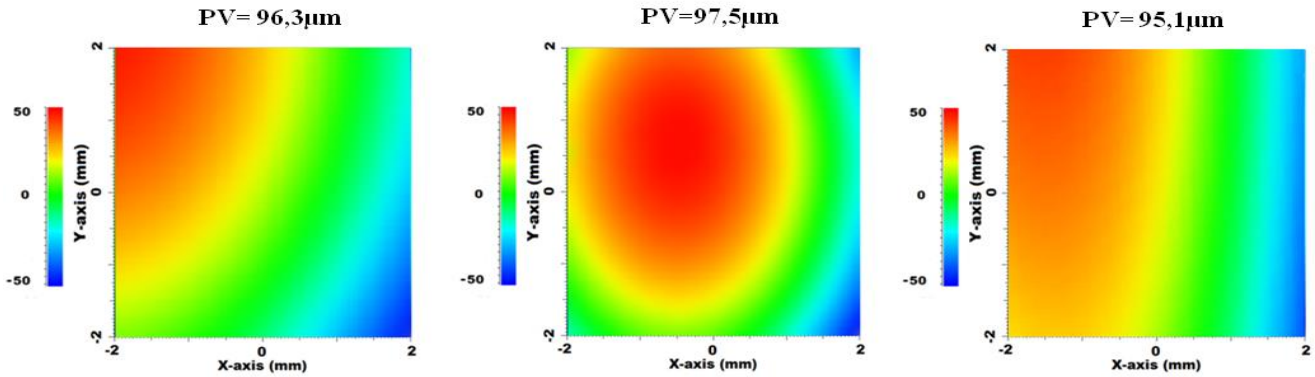

Fig.5.19 Examples of reconstructed wavefronts for 3 different locations of the freeform sample.

The characterization of the LED revealed that the LED has an unstable wavelength or intensity drop during longer working time (Fig5.20). This is the reason behind the choice of only five series of measurements at each arbitrary position.

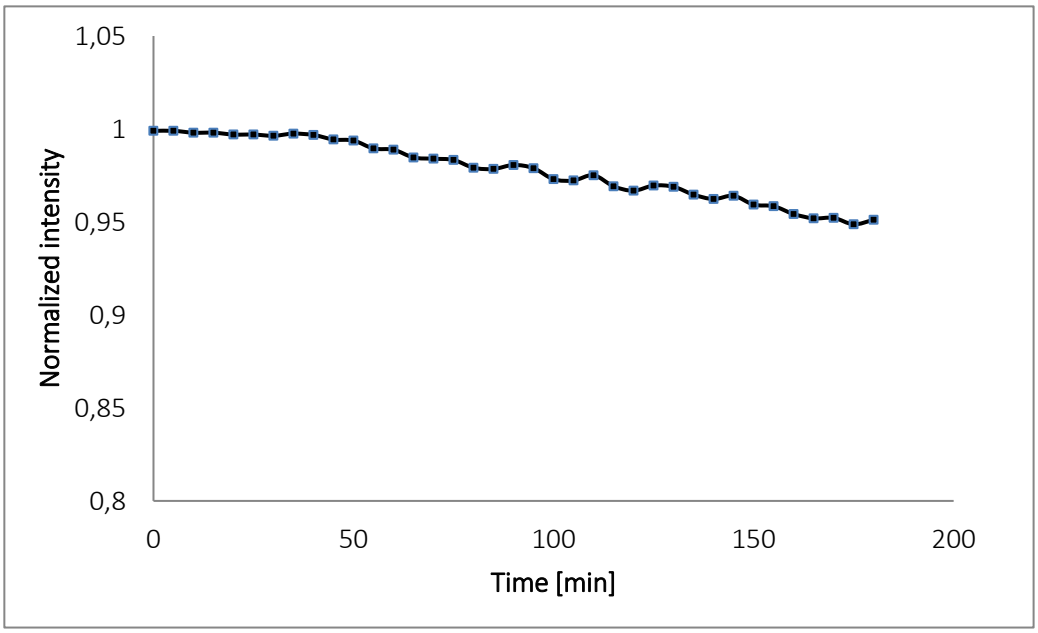

Fig.5.20 Degradation of the intensity in dependency of the time.

Thanks to the high-precision line table and the LabVIEW program, all series of measurements require less than 10 minutes. During this short time, no changes in wavelength or intensity are registered. Thus, the influence of the lighting system instability of the measurement process quality is excluded.

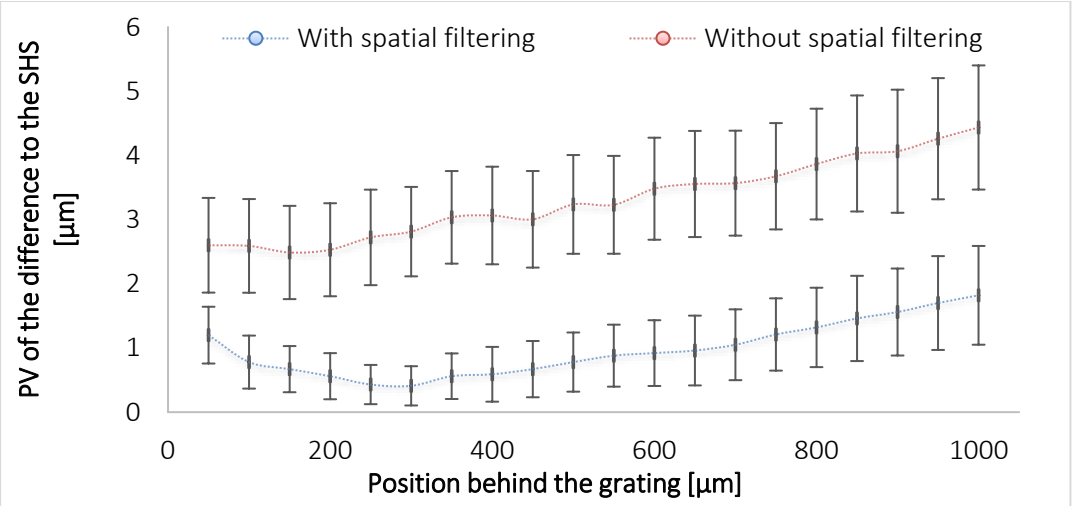

Fig.5.21 Peak-to-valley difference of reconstructed wavefront based on measurements of Shack Hartman Sensor and our method vs. propagation distance behind the grating.

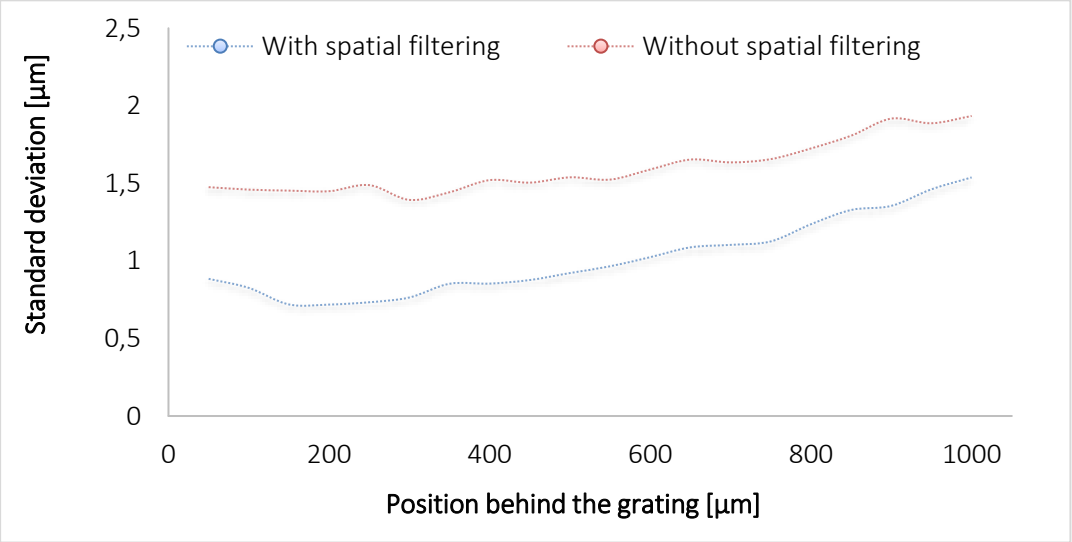

Fig 5.22 Standard deviation of the difference of reconstructed wavefront based on measurements of Shack Hartman Sensor and our method vs. propagation distance behind the grating.

In the present statistical study, the evolution of the difference between the presented method and the Shack Hartman Sensor with and without filtering are also similar to the simulation and to the results of the first experimental part. It has been shown that first the PV of the error decreases and then increases with considerable distance behind the grid. At the same time, the spatial filtering has the big effect of reducing the error and this confirms all previous results and simulations. The standard deviation in the measurement with the spatial filtering at the position 200µm behind the grating is only 0.7µm and increases at the position of 1mm to 1.5µm (Fig.5.22). Without filtering, the standard deviation is much larger and is equal to 1.45µm at the position of 200µm and 1.9µm at the position of 1mm. Three different wavefronts were generated with the help of one freeform element and simultaneously measured and characterized by the two measuring methods. These results are compared with each other. It turns out that the presented methods can measure and characterize different wavefronts with sufficient accuracy.

The observed difference to the Shack Hartman Sensor may also be due to the misalignment of the two measurement methods in the measurement setup. Nonetheless, they can be considered as minimal. In summary, the obtained results confirm the simulation part and the previous experimental results.

5.3 Experiment for reflection application

5.3.1 Setup

The measurement approach is experimentally tested on the example of a wavefront generated by the specular freeform surface shown in Fig.5.23. The freeform sample is an ophthalmic lens coated by a chromium layer. The schematic representation of the experiment is shown in Fig.5.24 and in Fig.5.25.

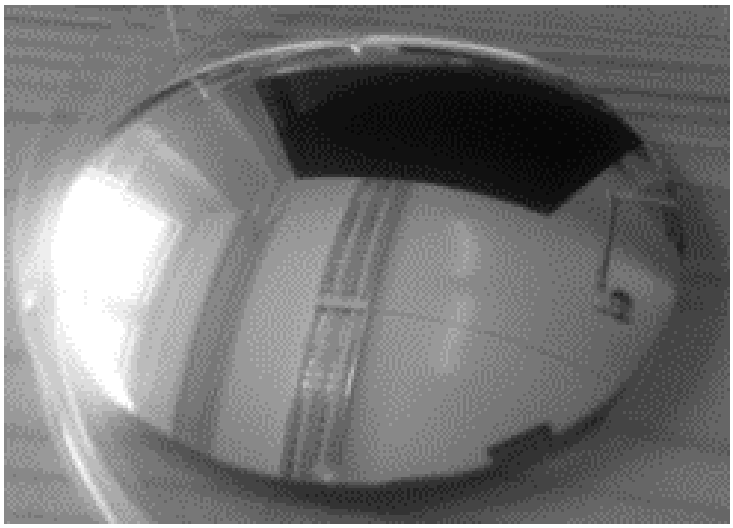

Fig.5.23 Freeform surface under test.

The setup consists of a LED source with a peak wavelength λ = 632nm, a spatial filtering assembly, two 4f systems including two similar achromats with a focal length of 120mm and a freeform surface under test. Our measurements are verified using a commercial Shack Hartmann Sensor (SHS) from Optocraft. A beamsplitter is inserted between the 4f system and the test object in order to deflect a part of the reflected light to the SHS (Fig.5.24). The rest is led to our monochrome CCD camera (uEye UI-1240SE, IDS Imaging Development Systems GmbH, 1280 x 1024 pixels, 5.2 x 5.2µm² pixel size) as described below.

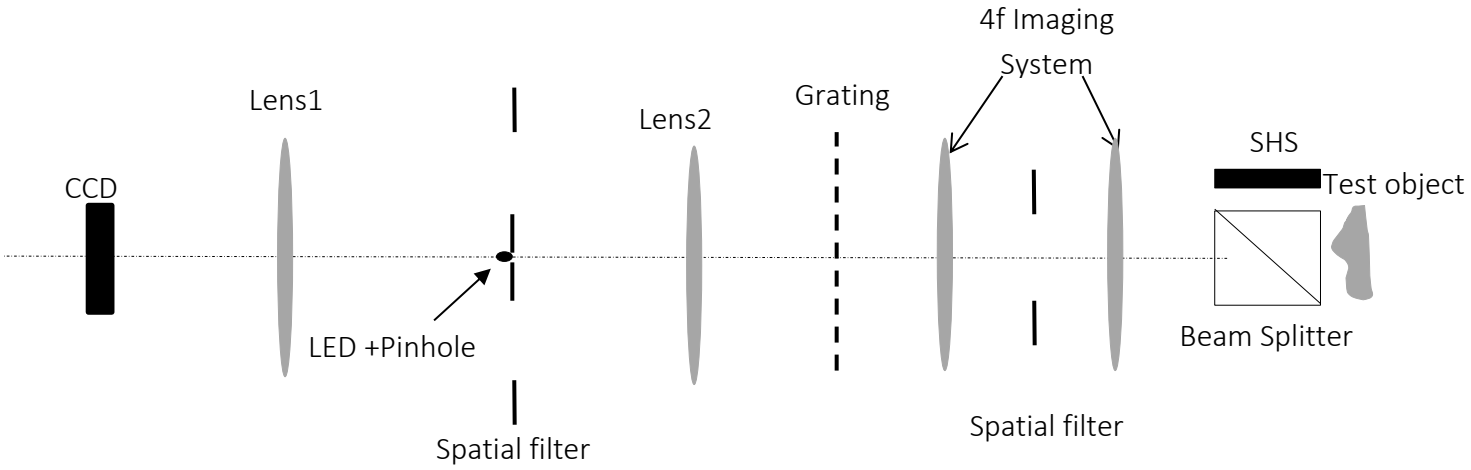

Fig.5.24 Schematic representation of the optical layout for the experimental validation.

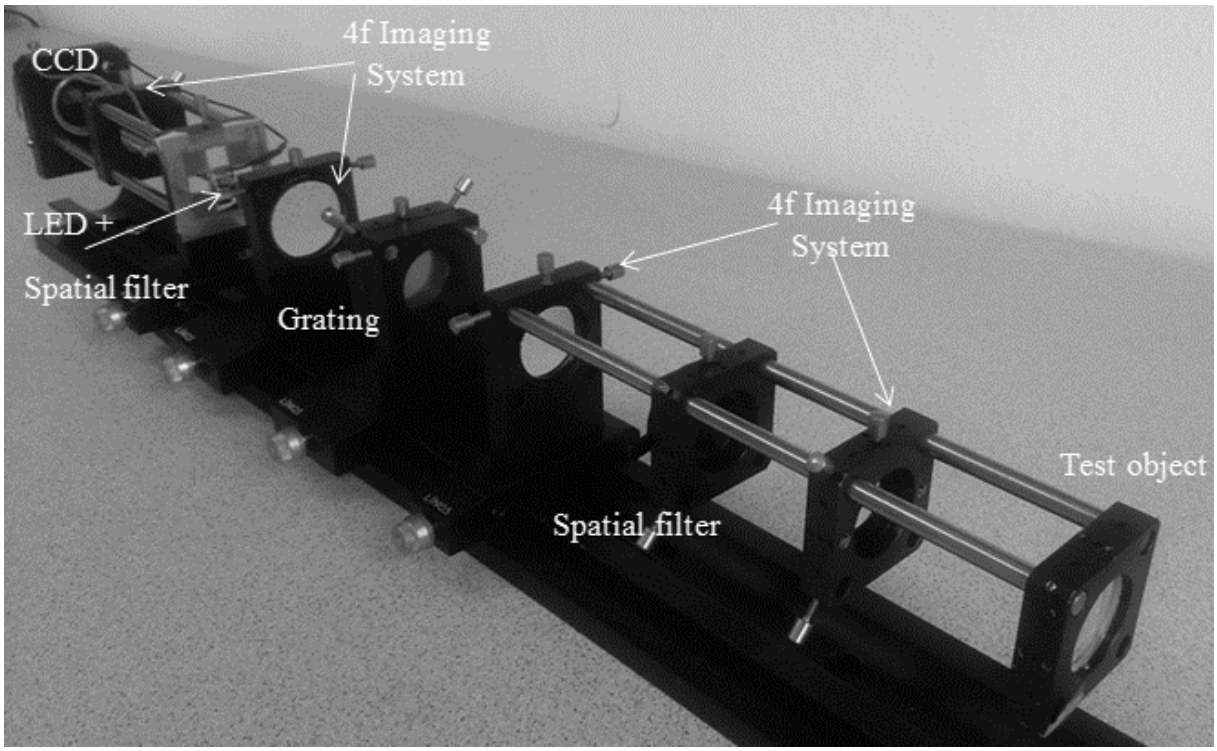

Fig 5.25 Setup for testing the measurement of reflective elements.

5.3.2 Results

After recording the intensity at the position of 200µm behind the grating with the CCD camera, the Fourier transform of the intensity is calculated numerically and the corner sub spectra in each direction are selected. After shifting the spectral replica to the origin, the presented proceeding steps is used. A point by point comparison to the SHS is presented in Fig.5.26. A section of 3 x 3mm² of our sample is observed.

The experimental results show a good correspondence between the SHS and our approach. Using the commercial SHS, a maximum profile height of 30.88µm (48.87waves) is registered. The maximal peak-to-valley deviation to our method is less than 348nm (0.55waves). This confirms the functionality of our method for reflective samples. The difference plot in Fig.5.26 (c) reveals a tilt. The latter is most likely the result of an inaccurate adjustment of the sensor relative to the optical axis. The RMS value including the tilt is 73.4nm (0.1162waves). It decreases to 32.0nm (0.05067waves) by subtracting the tilt. The maximal peak-to-valley deviation is less than 139.7nm (0.221waves).

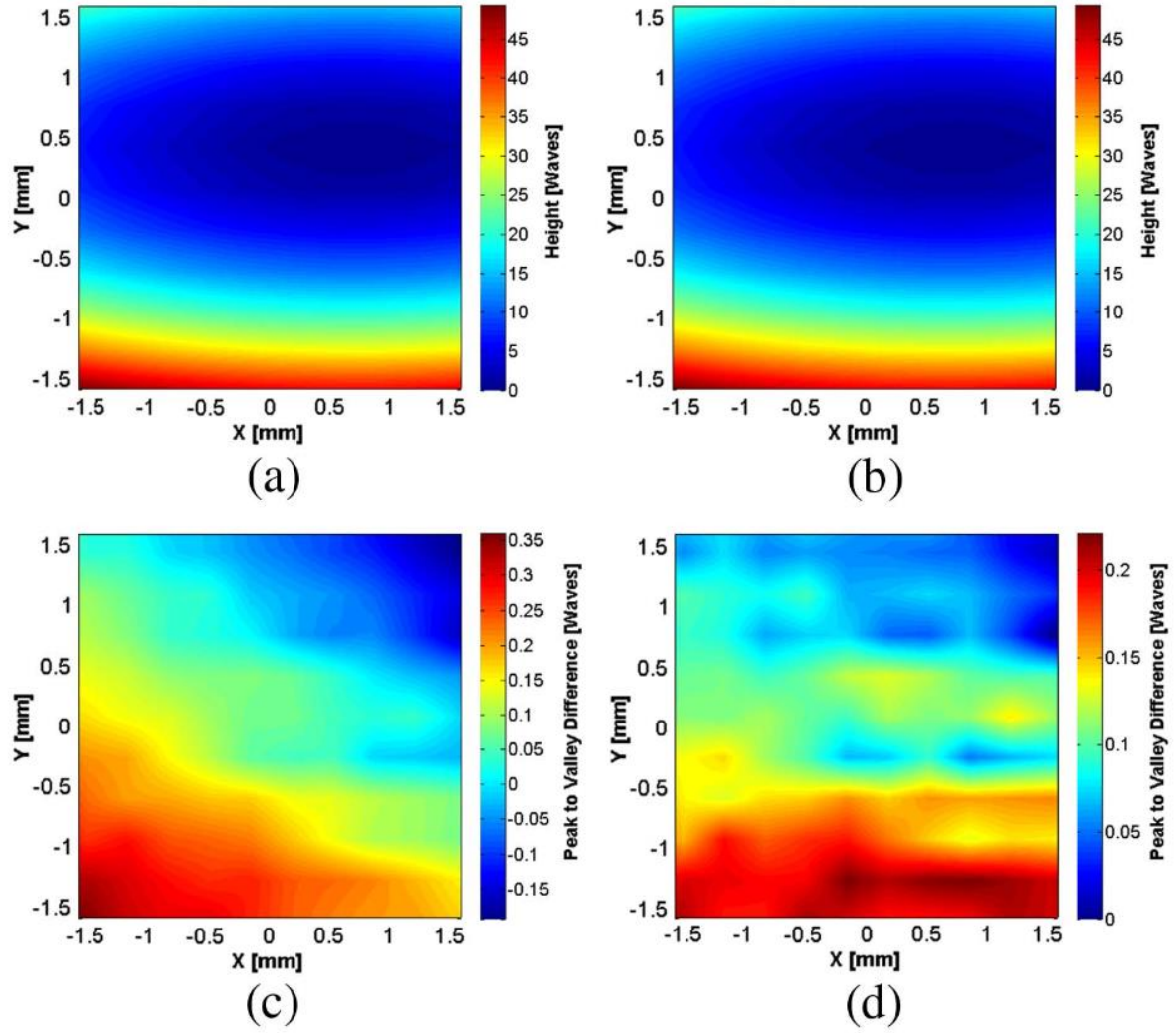

Fig.5.26 Wavefront reconstruction (a) by the Shack Hartman Sensor, (b) measurement by the presented method, (c) difference between both measurements, excluding the tilt (d).

- **Influence of the illumination intensity, exposition of sensor and signal to noise ratio**

In the previous section, it was demonstrated that the presented measurement method provides results comparable to those of Shack Hartmann. In the present work, the behaviour of the CCD sensor related to the registered signal strength is considered. The characteristic of the CCD sensor is considered linear with the accumulated energy, here the number of photons.

There are two limitations for the exploitation of the sensor dynamics: i) the noise overlapping (overcoming) low signal components and ii) the saturation which destroys useful signal information. The measurement should be well balanced between these limiting cases.

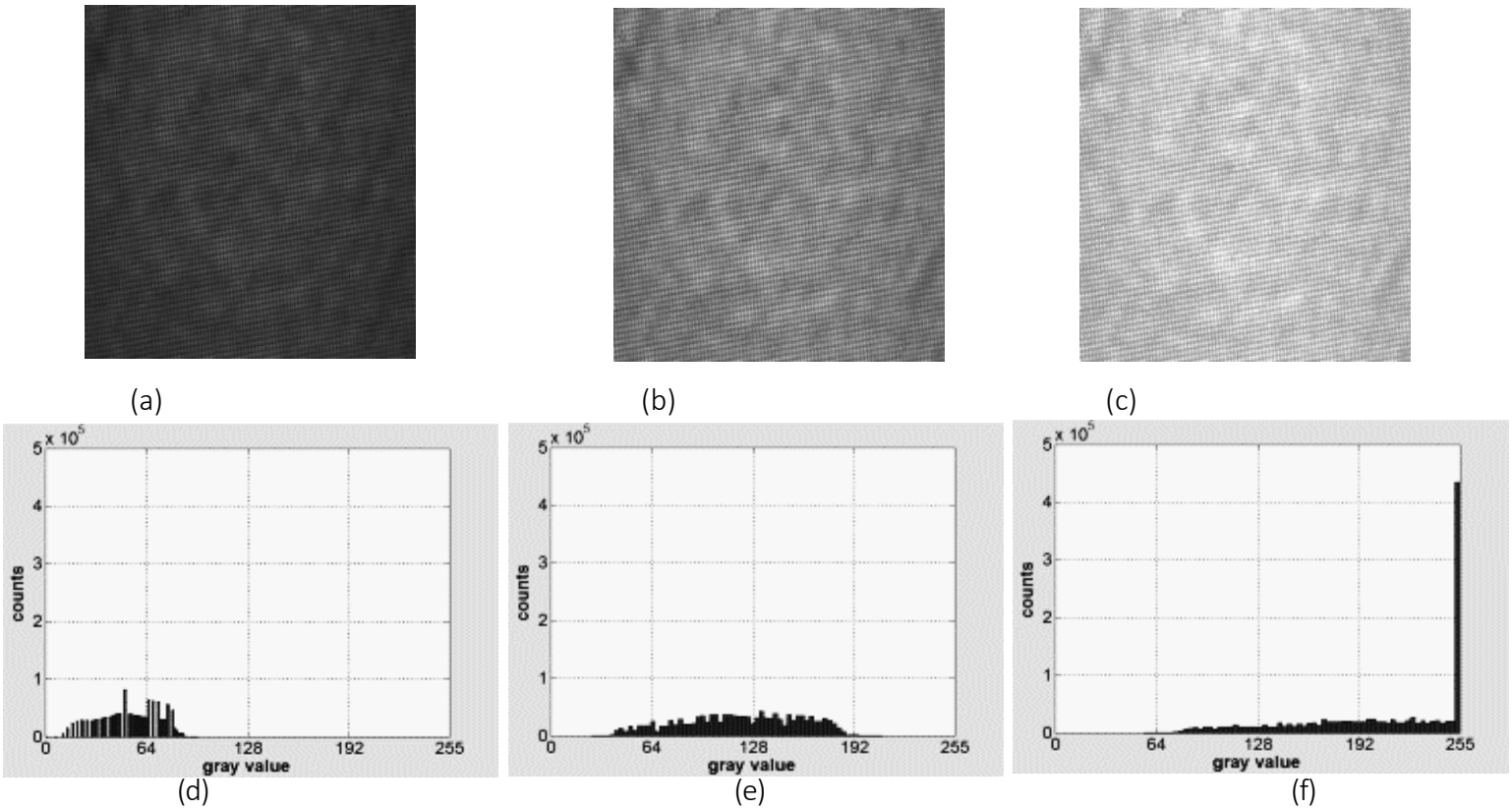

Fig.5.27 Top: Intensity patterns captured by (a) underexposed (exposure time: 25.5ms), (b) a best driven sensor (exposure time: 50.5ms) and (c) an overstressed sensor (exposure time: 113ms). bottom: histogram of the intensity of captured images (d) underexposed, (e) a best driven sensor and (f) an overstressed sensor.

In order to test the influence of the sensor characteristics on the measurement performance in our setup, the number of accumulated photoelectrons is adjusted by varying the exposure time ranging from 0.5ms up to 113ms in steps of 12.5ms (for examples of captured intensity distributions see Fig.5.27). The same sample point is therefore observed repeatedly.

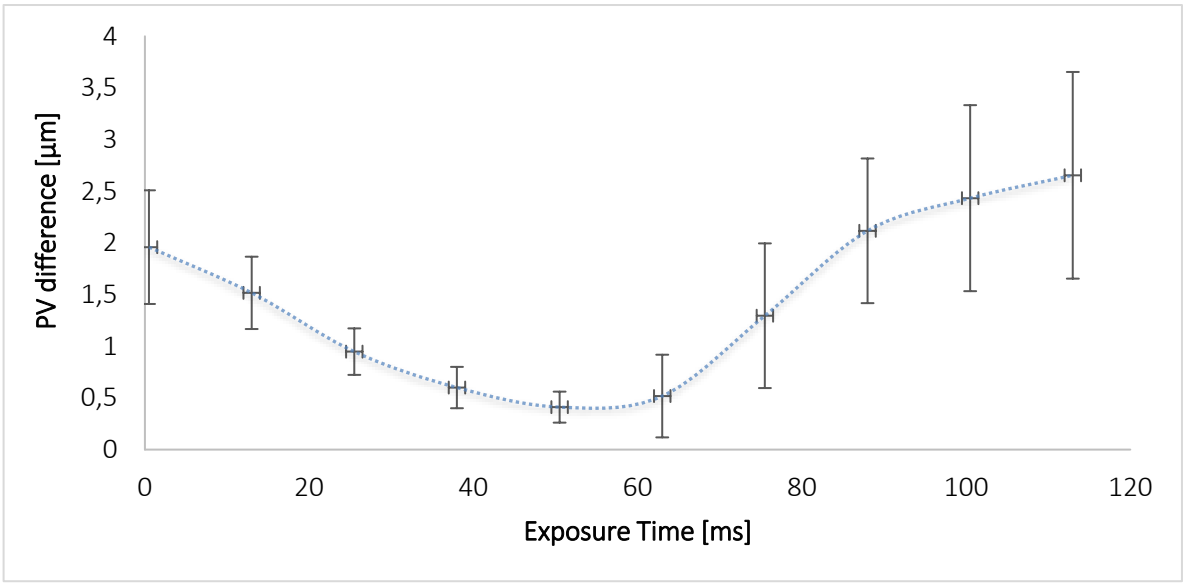

(a)

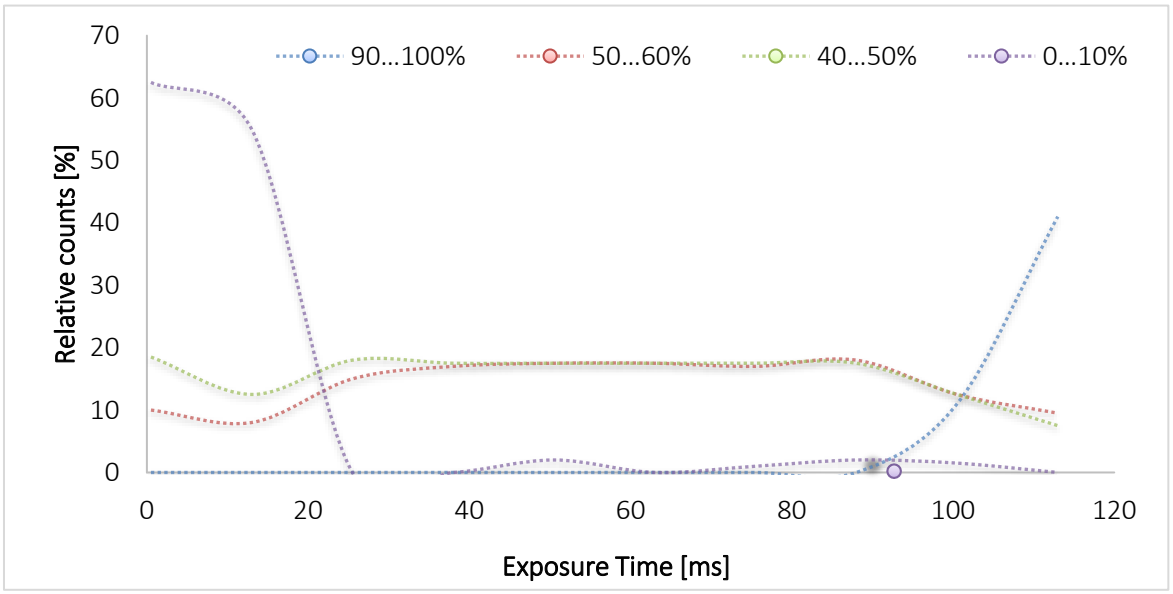

(b)

Fig5.28 (a) Peak-to-valley difference of both measurement methods including the standard deviation as a function of the exposure time. (b) Relative counts of captured intensity values in intervals of 0 to 10%, 40 to 50%, 50 to 60% and 90 to 100% related to the saturation of pixel vs. exposure time.

At each exposure time, the measurement is repeated 20 times. Then the results of both regimes are compared and the difference is illustrated in Fig.5.28 (a). It is referred to the maximal deviation (peak-to-valley) between the measurements of the Shack Hartman Sensor to our approach (blue curvature) which is more obvious than the RMS value between the determined surface geometries. The vertical bars at each exposure time measurement represents the standard deviation as uncertainty interval. Fig. 5.28 (b) illustrates the frequencies of captured pixel values related to its saturation.

These counts are accumulated in intervals of 0 to 10% (underexposed sensor pixel, high noise and quantization error), 40 to 50%, 50 to 60% (well exposed) and 90 to 100% (highly exposed/overstressed sensor pixel) depending on the exposure time. Indeed, it turned out that there is a minimum of the peak-to-valley deviation to the commercial SHS, here close to 50ms. Near this minimum, the smallest standard deviation is also recognized, which results in the best measurement stability. Beyond this minimum, the distortions increase due to information losses caused either by coarser quantization of smaller intensity values or by higher noise components of an overexposed sensor for high intensity values. The case of sensor overexposure in Fig.5.27 (c), which becomes clearly visible in the histogram in Fig. 5.27 (f), is not only linked with a cut of higher values but also with a strong increase of spectral noise. It is worthwhile to use captured images whose histograms imply a uniform distribution of the registered intensity values.

5.4 Summary

After the development of the theoretical fundamentals of the innovative measuring methods for the simultaneous characterization of optical elements in transmission and reflection and subsequently the confirmation of the theory by means of different simulations, various experiments were carried out in the last chapters. These experiments served to validate the measurement method in a real experimental environment. Initially, the experimental setup was constructed using a standard chrome diffractive element. However, unwanted back reflections had a great influence on the signal-to-noise ratio. In order to solve this challenge, an innovative diffractive amplitude grating based on nanostructured silicon was designed, manufactured, characterized and implemented in the test setup. The suppression of unwanted back reflection and thus the increase of the signal-to-noise ratio have been successfully confirmed. The next step was to confirm the measurement procedure for transmission. For this purpose, an optical freeform element was used as the test object. A SHS sensor was integrated into the measurement setup to enable simultaneous and comparable measurements with our measurement methods under the same measurement conditions. The measurements were carried out with and without spatial filtering. A statistical analysis has been established. The difference to the SHS showed that the use of spatial filtering has a positive influence on the generated results. The deviation from the SHS depends on the propagation distance behind the diffractive element. A repeatability study was also conducted. The results are compliant with the simulation results. After confirming the method on optical elements in transmission, additional optical elements were added to the measurement setup to be able to measure and characterize reflective optical element. After this minimal change, the SHS was again used to make a comparison. The difference between the two measuring methods also showed a dependence on the propagation distance behind the grating. In this section, an interesting parameter was examined at the end, namely the exposure time and the influence of these parameters on the results.

VI. Conclusion & Outlook

Optical free-form surfaces are advanced optical elements used in optical systems. The application areas can range from lighting systems to head-up displays arriving even to ophthalmic systems. The measuring technology for free-form surfaces is so far not fully mature. The inline characterization of freeform surfaces during the production cycle is even more challenging. For this, a measurement method for the simultaneous measurement in transmission and reflection would be desirable.

In this work, new results of the development of a versatile and compact sensor for inline evaluation are presented. Likewise, results of the characterization of free-form optical elements based on the Common Path Interferometric Approach are reported.

A method for reconstructing freeform wavefronts based on a novel theoretical approach has been developed. This theory allows the reconstruction of a complex wavefront using a binary modulating cross grating followed by optical Fourier filtering as well as Fourier analysis of the detected intensity signal. The presented theory is also based on a linear approximation of the angular spectrum propagator.

Our introduced approximation of the propagator phase ϕz enables to express this appropriate spectral decomposition, which allows the Fourier analysis in the shown manner. The introduction of spatial filtering in the Fourier region of the imaging system helps to improve the signal-to-noise ratio. Unlike other proposed methods that are limited to Talbot distances, the great advantage of our approach is that complex wavefronts can be reconstructed at each propagation distance.

This principle was extended to reflective components. The insertion of an additional point light source and a 4f imaging system allows the measurement and the characterization of optical elements simultaneously in transmission and reflection. Even if the test object is axially illuminated, conventional beam splitters are not required.

Operating with this arrangement and using a conventional binary diffraction grating, unwanted reflections occurred. Suppressing of such undesirable disturbance was a challenge and an important part of this work. For this purpose, an innovative nanostructured Silicon Amplitude Grating ("Silicon Grass") has been designed and manufactured.

Simulations and experimental studies on a freeform wavefront have verified this new approach. Due to the small experimental deviation compared to a commercial SHS, the proposed method and algorithm offers an efficient and cost-effective approach with high lateral resolution in non-imaging applications.

The influence of the partially coherent lighting system on the accuracy of the developed theory should be considered more closely. These influences should therefore be implemented in simulation to acquire the exact analysis of these most important parameters.

In the present dissertation, other works are performed concerning the increase of the dynamic range of the presented measuring method.

So far, the use of structured lighting has been designed and implemented. However, the appropriate stitching algorithm in Fourier space should be developed and implemented. Normally, the CCD sensors are geometrically limited. In some applications, the dimensions of optical elements are bigger than the CCD sensors. Thus, a stitching algorithm for freeform optical element was developed in cooperation with IIT Delhi (India Institute for Technology). Until now, this algorithm was only applied in combination with SHS. The first stitching experiments with the presented measurement method were carried out, but the results have to be analyzed systematically. Completing this work could be an interesting point for further investigation.

Bibliography

[1] G.W. Forbes and C.P. Brophy, ProcSPIE 7100 (2008) 1-15

[2] G.W. Forbes, Opt. Express 15 (2007) 5218–5226

[3] D. Malacara, Z. Malacara, Handbook of Optical Design, Dekker,Basel (2004).

[4] F. Fengzhou, C. Ying, Z. Xiaodong, Adv. Opt. Techn. 2 (2013) 445-453.

[5] K. P. Thompson and J. P. Rolland, Optics & Photonics News 23 (2012) 30-35.

[6] H. Ries, J. Muschaweck, J. Opt. Soc. Am. A 19 (2002) 590-595.

[7] G. E. Farin, Curves and Surfaces for Computer Aided Geometric Design: A Practical Guide, Academic Press, Boston 1993

[8] https://www.jenoptik.de

[9] R. Kleindienst, S. Sinzinger, Proc. SPIE 9751, Smart Photonic and Optoelectronic Integrated Circuits XVIII, 975110, 3 March 2016

[10] S.D. Hector, E.M. Gullikson, P. Mirkarimi, E. Spiller, P. Kearney and J. Folta, *Proc. SPIE* 4562 (2002) 863–881

[11] H. J. Levinson, T. A. Brunner, Proc. SPIE 10809, International Conference on Extreme Ultraviolet Lithography 2018, 1080903 24 October 2018

[12] D. Golini, W. I. Kordonski, P. Dumas, S. J. Hogan, Proc. SPIE 3782, Optical Manufacturing and Testing III, 11 November 1999

[13] Bayly A.R., Townsend P.D.Optical applications of ion beam machining Optics and Laser Technology, Volume 5, 1973

[14] H. L. Gerth, R. E. Hewgley, Proc. SPIE 0093, Advances in Precision Machining of Optics, 16 December 1976

[15] H. F. Talbot, The London and Edinburgh Philosophical Magazine and Journal of Science 9.56 (1836) 401-407

[16] Lord Rayleigh, The London, Edinburgh, and Dublin Philosophical Magazine and Journal of Science 11.67 (1881) 196-205

[17] K. Patorski, Appl. Opt. 24 (1985) 4448-4453.

[18] D. Podanchuk, V. Kurashov, M. Kotov, V. Danko, O. Parhomenko, Proc. SPIE 8338 (2011).

[19] D. Podanchuk, V. Kurashov, A. Goloborodko, V. Danko, M. Kotov, N. Goloborodko, Appl. Opt. 51 (2012) C 125-131.

[20] H. F. Talbot, Philos. Mag. Ser. 3 9 (1836) 401-407.

[21] L. Rayleigh, Philos. Mag. Ser. 5 11 (1881) 196-205.

[22] P. Latimer, R. F. Crouse, Appl. Opt. 31 (1992) 80-89.

[23] C. Zhang, W. Zhang, F. Li, J. Wang, S. Teng, Appl. Opt. 52 (2013) 5083-5087.

[24] N. Salama, D. Patrignani, L. De Pasquale, and E. Sicre, Opt. Laser Technol. 31 (1999) 269–272

[25] C. Siegel, F. Loewenthal, and J. E. Balmer, Opt. Commun. 194 (2001) 265–275

[26] R. Sekine, T. Shibuya, K. Ukai, S. Komatsu, M. Hattori, T. Mihashi, N. Nakazawa, and Y. Hirihara, Opt. Rev. 13 (2006) 207–211

[27] D. Podanchuk, V. Kurashov, A. Goloborodko, V. Dan'ko, M. Kotov, and N. Goloborodko, Appl. Opt. 51 (2012) C125–C132

[28] D. V. Podanchuk, A. A. Goloborodko, and M. M. Kotov, Proceedings of the International Conference on Advanced Optoelectronics & Lasers (CAOL), O. V. Shulika and I. A. Sukhoivanov, eds. (IEEE, 2013) 337–339

[29] D. Podanchuk, A. Kovalenko, V. Kurashov, M. Kotov, A. Goloborodko, and V. Danko, Appl. Opt. 53 (2014) B223-B230

[30] M. Takeda, H. Ina, S. Kobayashi, JOSA 72 (1982) 156-160.

[31] K. Ichikawa, A.W. Lohmann, M. Takeda, Appl. Opt. 27 (1988) 3433-3436.

[32] F. Roddier, Appl. Opt. 29 (1990) 1402-1403.

[33] C. Siegel, F. Loewenthal, J. E. Balmer, Opt. Commun. 194 (2001) 265-275.

[34] K. Patorski, Appl. Opt. 24 (1985) 4448–4453

[35] K. Patorski, Prog.Opt. 27 (1989) 1–108

[36] S. A. Benton and D. P. Merrill, Optical Engineering 15 (1976)154328

[37] C. S. Lim and V. Srinivasan, Opt. Commun. 44 (1983) 219–222

[38] J. Jahns and A. W. Lohmann, Appl. Opt. 43 (2004) 4339–4344

[39] J. Jahns, E. ElJoudi, D. Hagedorn and S. Kinne, International Journal for Light and Electron Optics 112 (2001) 295–298

[40] H. Kaijun, J. Jahns and A. W. Lohmann, Opt. Commun. 45 (1983) 295–300

[41] D. S. Mehta, S. K. Dubey, C. Shakher and M. Takeda, Appl. Opt. 45 (2006) 7602–7609

[42] M. Born, E. Wolf, Principles of Optics - Electromagnetic theory of propagation interference and diffraction of light, 1984

[43] George C. Sherman and W. C. Chew, J. Opt. Soc. Am. 72 (1982) 1076-1083

[44] The Taylor Series: an Introduction to the Theory of Functions of a Complex Variable. *Nature* 130**,** 188 (1932)

[45] J. Goodman, *Introduction to Fourier Optics*, Mc Graw Hill, 1996

[46] A. W. Lohmann, *Optical Information Processing,* Universitätsverlag Ilmenau,2006

[47] G. Rousset, Adaptive Optics in Astronomy, Cambrige University press, 1999

[48] D.R. Neal, D.M. Topa, J. Copland, Proceedings of SPIE 4245 (2001) 72-91.

[49] J. Pfund, N. Lindlein, J. Schwider, Optics Letters 23 (1998) 995-997.

[50] L. Seifert, J. Liesener, H.J. Tiziani, Optics Communications, 216 (2002) 313-319.

[51] J. Son, D. Podanchuk, V. Danko, K. Kwak, Opt. Eng. 42 (2003) 3389-3398.

[52] M. A. Solovev, V. Y. Venediktov, Proc. SPIE 9508 (2015).

[53] F. Roddier, Optical Engineering 29 (1990) 1239-1242.

[54] G. H. Kaufmann, Optics Communications 217 (2003) 141-149.

[55] K.-H. Hofmann and G. Weigelt, J. Opt. Soc. Am. A 3 (1986) 1908-1911

[56] K. Creath, Y. Y. Cheng, J. C. Wyant, Optic Acta 32 (1985) 1455–1464.

[57] K. Creath, Progress in Optics XXVI ed. E. Wolf, 1988

[58] J.E. Greivenkamp, Optical Engineering 23 (1984) 350-352

[59] C.J. Morgan, Optics Letters 7 (1982) 368-370

[60] J.C. Wyant, C.L. Koliopoulos, B. Bhushan, O.E. George, ASLE Trans. 27 (1984) 101-113

[61] J.C. Wyant, Laser Focus 65, 1982

[62] P. Carré, Metrologia 2 (1966) 13-23

[63] G. Baer, J. Schindler, C. Pruss, W. Osten, 114th conference of the DGaO, Braunschweig, p. P17, 2013

[64] A. Harasaki, J. Schmit, J.C. Wyant, Applied Optics 39 (2000) 2107-2115.

[65] http ://www.phase-shift.com/products/microxam.shtml.

[66] http ://www.veeco.com/html/product bymarket.asp.

[67] http ://www.zygo.com.

[68] E. Garbusi, C. Pruss, W. Osten, Opt.Lett. 33 (2008) 2973-2975.

[69] E. Garbusi, W. Osten, J. Opt. Soc. A 26 (2009) 2538-2549.

[70] C. Pruss, W. Osten, 114th conference of the DGaO, Braunschweig, p. H2, 2013

[71] G. Baer, J. Schindler, C. Pruss, W. Osten, 114th conference of the DGaO, Braunschweig, p. P17, 2013

[72] J. Schindler, G. Baer, C. Pruss, W. Osten, 114th conference of the DGaO, Braunschweig, A010-0, 2013

[73] J. Liesener, E. Garbusi, C. Pruss, W. Osten, Deutsches Patent und Markenamt 10 057 606.3, 2006

[74] G. Baer, J. Schindler, C. Pruss, W. Osten, JEOS 8 (2013) 130874

[75] I. Fortmeier, M. Stavridis, A. Wiegmann, M. Schulz, W. Osten, C. Elster, Opt. Express 24 (2016) 3393-3404.

[76] R. S. Hilbert, M. P. Rimmer, Appl. Opt. 9 (1970) 849-852.

[77] J. Pastor, Appl. Opt. 8 (1969) 525- 531.

[78] A. J. MacGovern, J. C. Wyant, Appl. Opt. 10 (1971) 619-624.

[79] J. Schwider, R. Burow, Optica Applicata VI (1976) 83-89.

[80] J. Schwider, R. Burow, J. Grzanna, Optica Applicata IX (1979) 39-45.

[81] G. Schulz, J. Schwider, Progress in Optics XIII, ed. E. Wolf Chap. 4 (1976) 93-167.

[82] J. C. Wyant, P. K. O'Neill, Appl. Opt. 13 (1974) 2762-2765.

[83] J.W. Goodman. Introduction to Fourier Optics. McGraw-Hill Inc., New-York (1968).

[84] C. Verinaud, Opt. Commun. 233 (2004) 27–38.

[85] S. Esposito, A. Riccardi, Astron. Astrophys. 369 (2001) L9–L12.

[86] R. Ragazzoni, J. Farinato, Astron. Astrophys. 350 (1999) L23–L26.

[87] M. Van Kooten, J. P. Veran, C. Bradley, J. Astron. Telesc. Instrum. Syst. 3 (2017) 029001.1-029001.6.

[88] E. Mieda, M. Rosensteiner, M. Van Kooten, J. P. Veran, O. Lardiere, G. Herriot, Proc. SPIE 9909, 2016

[89] http ://www.ifr58- cordeliers.jussieu.fr/microscopie/confocale/dossiers.htm.

[90] https://www.leica-microsystems.com/products/confocal-microscopes.

[91] M. C. Hutley, R. F. Stevens, J. Phys. E. Sci. Instrum. 21 (1988) 1037.

[92] M. A. Browne, O. Akinyemi, A. Boyde, Scanning 14 (1992) 145–153.

[93] M. Hillenbrand, “Design of confocal systems for spectral information coding”, Dissertation, Technische Universität Ilmenau Germany (2016).

[94] F. Charriere, J. Juhn, T. Colomb, F. Montfort, E. Cuche, Y. Emery, K. Weible, P. Marquet, C. Depeursinge, Appl. Opt. 45 (2006) 829-835.

[95] J. Muller, V. Kebbel, W. Juptner, Opt. Lasers Eng. Papers 43 (2005) 739-751.

[96] J. Muller, V. Kebbel, W. Juptner, Proc. SPIE 4778 (2002) 188-197.

[97] E. Cuche, P. Marquet, C. Depeursinge, Appl. Opt. Papers 38 (1999) 6994-7001.

[98] M. Knauer, J. Kaminski, G. Häusler, Proc. SPIE 5457 (2004) 366- 376.

[99] J. Kaminski, “Geometrische Rekonstruktion spiegelnder Oberflächen aus deflektometrischen Messdaten,” Dissertation, University of Erlangen Nuremberg (2008).

[100] G. Häusler, G., “Verfahren und Vorrichtung zur Ermittlung der Form oder der Abbildungseigenschaften von spiegelnden oder transparenten Objekten,” German patent DE 19944354 (1999).

[101] M. C. Knauer, J. Kaminski, G. Häusler, Proc. SPIE 5457 (2004) 366-376.

[102] R. Ritter, R. Hahn, Opt. Las. Eng. 4 (1983) 13-24.

[103] M. Petz, R. Tutsch, International Symposium of Photonics in Measurement 1844 (2002) 329-332.

[104] M. Petz, R. Tutsch, Messen und Prüfen – Optische Messtechnik, Carl Hanser Verlag, München (2002) 556-558.

[105] D. Pérard, J. Beyerer, Proc. SPIE 3204 (1997) 74-80.

[106] D. Pérard, Fortschritt-Berichte VDI, Reihe 8, Nr. 869, VDI Verlag, Düsseldorf (2001).

[107] E. Savio, L. D. Chiffre, R. Schmitt, CIRP Ann. - Manuf. Techn. Papers 56 (2007) 810-835.

[108] J. H. Price, A. G. David, U.S. Patent No. 5,790,710 (1998).

[109] K. C. Fan, C. L. Chu, J. I. Mou, Meas. Sci. Technol. Papers 12 (2001) 2137-2146.

[110] L. Firestone, K. Cook, K. Culp, N. Talsania, K. Preston, Cytometry 12 (2005) 195-206.

[111] A. Yacoot, L. Koenders, Meas. Sci. Technol. Papers 22 (2011).

[112] F. J. Giessibl, Rev. Mod. Phys. Papers 75 (2003) 949-983.

[113] H. U. Danzebrink, L. Koenders, G. Wilkening, A. Yacoot, H. Kunzmann, CIRP Ann. - Manuf. Techn. Papers 55 (2006) 841-878.

[114] M. A. Paesler, P. J. Moyer, Near-field optics: Theory, instrumentation and applications, Wiley-Interscience Publication New York (1996).

[115] D. Courjon, Near-field Microscopy and Nearfield Optics, Imperial College Press UK (2003).

[116] T. Mayes, M. Riley, K. Edward, R. Fesperman, A. Suraktar, U. Shahid, S. Williams, R. Hocken, CIRP Ann. Papers 53 (2004) 483-486.

[117] Y. H. Lin, D. P. Tsai, Opt. Exp. Papers 20 (2012) 16205-16211.

[118] G. B. Picotto, S. Desogus, S. Lanyi, R. Nerino, A. Sosso, J. Vac. Sci. Technol., B. Papers 14 (1996) 897-900.

[119] T. Fujii, M. Suzuki, M. Yamaguchi, Int. J. Nanotechnol. Papers 6 (1995) 121-126.

[120] J. Aoki, W. Gao, S. Kiyono, T. Ono, Key Eng. Mater. Papers 295-296 (2005) 65-70.

[121] G. L. Dai, F. Pohlenz, H. Danzebrink, M. Xu, K. Hasche, G. Wilkening, Rev. Sci. Instrum. Papers 75 (2004) 962-969.

[122] M. Stedman, K. Lindsey, Proc. SPIE 1009 (1989) 56-61.

[123] D. H. Lee, N. G. Cho, Meas. Sci. Technol. Papers 23 (2012) 1-12.

[124] M. Ashraf, C. Gupta, F. Chollet, S. V. Springham, R. S. Rawat, Opt. Lasers Eng. Papers 46 (2008) 711-720.

[125] P. Nussbaum, R. Völkel, H. P. Herzig, M. Eisner, S. Haselbeck, J. Eur. Opt. Soc. Part A Papers 6 (1997) 613-617.

[126] Radhakrishnan, V. Wear, 16, (1970) 325-335.

[127] P. M. Lonardo, D. A. Lucca, L. D. Chiffre, CIRP - Manuf. Techn. Papers 51 (2002) 701-723.

[128] H. T. Hsieh, L. Vinna, J. L. Hsieh, G. D. John Su, Opt. Commun. Papers 284 (2011) 5225-5230.

[129] http://epigem.co.uk/products/micro-optics

[130] J. M. Bennett, J. H. Dancy, Appl. Opt. Papers 20 (1981) 1785-1802.

[131] I. S. Savel'ev, J. Surf. Invest. Papers 5 (2011) 533-538.

[132] http://www.taylor-hobson.com

[133] http://www.kla-tencor.com/chip-manufacturing-front-end-defect-inspection/frontend-defect-inspection.html

[134] É. Lalor, J. Opt. Soc. Am. 58 (1968) 1235-1237

[135] K. Matsushima, H. Schimmel, and F. Wyrowski, J. Opt. Soc. Am. A 20 (2003) 1755-1762

[136] S. De Nicola, A. Finizio, G. Pierattini, P. Ferraro, and D. Alfieri, Opt. Express 13 (2005) 9935-9940

[137] M. Totzeck, J. Opt. Soc. 8 (1991) 27-32.

[138] T. Shimobaba, K. Matsushima, T. Kakue, N. Masuda, Opt. Lett. 37 (2012) 4128-4130

[139] J. J. Stamnes, J. Opt.Soc. 71(1981) 15-20.

[140] N. Delen, B. Hooker, J. Opt. Soc. A 15 (1998) 857-867.

[141] J. A. Hudson, Appl. Opt. 23 (1984) 2292-2295.

[142] C. Kopp, P. Meyrueis, Opt. Commun. 158 (1998) 7-10.

[143] S. Deng, T. Okada, K. Behler, and X. Wang, eds., Proc. SPIE 4915 (2002) 180–186

[144] N. Delen, B. Hooker, Appl. Opt. 40 (2001) 3525-2531.

[145] F. Shen, A. Wang, Appl. Opt. 45 (2006) 1102-1110.

[146] R. T. Frankot, R. Chellappa, IEEE Trans. Pattern Anal. Machine Intell. 10 (1988) 439-451.

[147] S. Leopold, C. Kremin, A. Ulbrich, S. Krischok, M. Hoffmann, J. Vac. Sci. Technol. B 29 (2010) 011002

[148] S. Leopold, L. Mueller, C. Kremin, M. Hoffmann, Journal of Micromechanics and Microengineering 23 (2013) 075025/1-075025/8

[149] H. K. Raut, V. A. Ganesh, A. S. Nair, S. Ramakrishna, Royal Soc Chemistry 4 (2011) 3779-3804.

[150] F. Flory, L. Escoubas, G. Berginc, Journal of Nanophotonics 5 (2011) 1-20

[151] R. M. Goldstein, H. A. Zebker, C. L. Werner , Radio Science 23 (1988) 713-720.

[152] L. McCarty, An Introduction to Measurement and Uncertainty. Physical Sciences 2 course home-page. Dept. of Physics, Harvard University, Sept 2006

[153] J. R. Taylor, An Introduction to Error Analysis: The Study of Uncertainties in Physical Measurements. 2nd ed. Sausalito, CA: University Science Books, 1997

[154]. G.S. Khan, K.K. Pant, M. Bichra, D.R. Burada, S. Sinzinger, C. Shakher, Freeform Optics, Optical Society of America (2015) FTh2B-3

[155] S. Stoebenau, R. Kleindienst, M. Hofmann, and S. Sinzinger, Proc. SPIE 8126, 812614 (2011)

[156] S. Singh, Optics & Laser Technology 31 (1999) 195-218.

[157] J. Ziegler, J. Haschke, T. Käsebier, L. Korte, A. N. Sprafke, and R. B. Wehrspohn, Opt. Express 22 (2014) A1469-A1476

[158] S. Leopold, L. Mueller, C. Kremin, M. Hoffmann, J. Micromech. Microeng. 23 (2013) 074001

[159] L. Müller, I. Käpplinger, S. Biermann, W. Brode, M. Hoffmann, J. Micromech. Microeng. 24 (2014) 035014

[160] N. Tucher, H. T. Gebrewold, and B. Bläsi, Opt. Express 26, A937-A945 (2018)

Awards

- ✓ International Trade Fair “Ideas – Inventions – New Products” iENA 2017 in Nüremberg : Bronze medal for the invention of „Anordnung zur Vermessung zumindest teilweise reflektierender Oberflächen“.

- ✓ International Trade Fair “Ideas – Inventions – New Products” iENA 2014 in Nuremberg : Silver medal for the invention of “ optical measurement system for freeform surfaces”.

- ✓ BEST POSTER Award of the 115th annual meeting of the DGaO (Deutsche Gesellschaft für angewandte Optik)

Patents

- ✓ M. Bichra, T. Meinecke, S. Sinzinger, “Anordnung zur Vermessung zumindest teilweise reflektierender Oberflächen” German Patent: DE 10 2017 001 524.4

- ✓ M. Bichra, N. Sabitov, S. Sinzinger, “Vorrichtung und Verfahren zur Vermessung zumindest teilweise reflektierender Oberflachen” German Patent: DE 10 2013 018 569.6

- ✓ M. Hillenbrand, L. Lorenz, M. Bichra, R. Kleindienst, S. Sinzinger, “Verfahren und Vorrichtung zur chromatisch-konfokalen Mehrpunktmessung sowie deren Verwendung” German Patent: DE 10 2013008 582 B4

Scientific publications and conference papers

1. P.-G Dittrich, M. Bichra, C. Pfützenreuter, M. Rosenberger, G. Notni “Measurement principle and arrangement fo the determination of spectral channel.specific angle dependencies for multispectral resolving filter-on-chip CMOS cameras”: Proc. SPIE 11144, Photonics and Education in Measurement Science 2019, 111440S (17 Septembe 2019); doi: 10.1117/12.2527871

2. D R. Burada, K K. Pant, V. Mishra, M. Bichra, G S. Khan, S. Sinzinger, and C. Shakher, “Development of a metrology technique suitable for in-situ measurement and corrective manufacturing of freeform optics “, Advanced Optical Technologies, 8(3-4), pp. 203-215. Retrieved 30 Jan. 2020, from doi:10.1515/aot-2018-0072

3. P.-G. Dittrich, M. Bichra, D.Stiehler, G. Notni “Extended characterization of multispectral resolving filter-on-chip snapshot-mosaic CMOS cameras” May 2019

DOI: 10.1117/12.2518842 Conference: Algorithms, Technologies, and Applications for Multispectral and Hyperspectral Imagery XXV

4. K. Pant, D R. Burada, **M. Bichra**, A. Ghosh, G S. Khan, S. Sinzinger, C. Shakher, “Weighted spline based integration for reconstruction of freeform wavefront”, Applied optics. 57. 1100-1109. 10.1364/AO.57.001100.

5. D. R. Burada, K. K. Pant, V. Mishra, **M. Bichra**, G. S. Khan, S. Sinzinger, and C. Shakher, "Development of an In-situ Metrology Technique for Freeform Optics," in Frontiers in Optics / Laser Science, OSA Technical Digest, paper JTu3A.11.

6. D R. Burada, K K. Pant, V. Mishra, **M. Bichra**, G S. Khan, S. Sinzinger, C. Shakher, "Development of metrology for freeform optics in reflection mode," Proc. SPIE 10329, Optical Measurement Systems for Industrial Inspection X, 103291K.

7. D R. Burada, K. Pant, **M. Bichra**, G S. Khan, S. Sinzinger, C. Shakher “Experimental investigations on characterization of freeform wavefront using Shack–Hartmann sensor”. Optical Engineering. 56. 10.1117/1.OE.56.8.084107.

8. **M. Bichra**, T. Meinecke, P. Fesser, L. Müller, M. Hoffmann, S. Sinzinger “Freeform characterization based on nanostructured diffraction gratings” Applied Optics. 57. 3808. 10.1364/AO.57.003808.

9. **M. Bichra**, N. Sabitov, T. Meinecke, S. Sinzinger “Wavefront sensing by numerical evaluation of diffracted wavefields” Applied Optics. 56. A13. 10.1364/AO.56.000A13.

10. **M. Bichra**, X. Cao, J. Pribošek, S. Sinzinger “Illumination concepts for integrated optical sensors” SeW3D.6. 10.1364/SENSORS.2016.SeW3D.6.

11. **M. Bichra**, N. Sabitov, K. Pant, D. Ramu, G S.Khan , S. Sinzinger “Subaperture wavefront measurement using Talbot interferometry “ DGaO-Proceedings 2016 – http://www.dgao-proceedings.de – ISSN: 1614-8436 – urn:nbn:de:0287-2016- B022-8

12. **M. Bichra**, T. Meinecke, S. Sinzinger “Innovative Verfahren zur Metrologie von Freiformoberflächen „ DGaO-Proceedings. - Erlangen-Nürnberg: Dt. Gesellschaft für angewandte Optik. -118 (2017), Art. A24, 2 S. ISSN: 1614-8436 URN: urn:nbn:de:0287-2017-A024-6

13. **M. Bichra**, T. Meinecke, S. Sinzinger “In-Line Setup for the Characterization of Optical Freeform Surfaces “ DGaO Proceedings 2018 – http://www.dgaoproceedings. de – ISSN: 1614-8436, – urn:nbn:de:0287-2018-P045-0

14. R. Fischer, **M. Bichra**, A. Straube, M. Stubenrauch, S. Sinzinger, H. Witte “Adaptable, automated platform for miniaturized cell cultivation experiments including Fourier-optical analytics”. - In: Basic & clinical pharmacology & toxicology - Oxford : Wiley-Blackwell, ISSN 1742-7843, Bd. 122 (2018), Supplement S1, ICBB17-13, Seite 6-7,https://doi.org/10.1111/bcpt.12952

15. **M. Bichra**, L. Müller, P. Feßer, M. Hoffmann, S. Sinzinger “Nanostrukturierte Beugungsgitter für integrierte Metrologie”. - In: MikroSystemTechnik Kongress 2017 "MEMS, Mikroelektronik, Systeme" - Berlin: VDE Verlag GmbH, ISBN 978-3- 8007-4491-6, (2017), S. 548-551

16. R. Robert, M. Stubenrauch, A. Straube, K. Wedrich, B. Goj, H. Bartsch, **M. Bichra**, H Rothe, H. Witte ”System for automated cell cultivation and analysis“. - In: Engineering for a changing world: 59th IWK, Ilmenau Scientific Colloquium, Technische Universität Ilmenau, September 11-15, 2017 : proceedings - Ilmenau : ilmedia, (2017), insges. 2 S.

17. **M. Bichra**, L. Müller, P. Feßer, M. Hoffmann, S. Sinzinger “Innovative freeform measurement method using two dimensional binary diffractive grating based on nanostructured silicon” - In: Engineering for a changing world : 59th IWK, Ilmenau Scientific Colloquium, Technische Universität Ilmenau, September 11-15, 2017 : proceedings - Ilmenau : ilmedia, (2017), insges. 7 S.

18. **M. Bichra**, T. Meinecke, S. Sinzinger “Wavefront sensing by numerical evaluation of diffracted wavefields”. - In: AMA conferences 2017 - Wunstorf, Germany : AMA Service GmbH, ISBN 978-3-9816876-4-4, (2017), S. 290-293

19. **M. Bichra**, S. Sinzinger “Subaperture wavefront measurement using Talbot interferometry” DGaO-Proceedings 2016 – http://www.dgao-proceedings.de – ISSN: 1614-8436 – urn:nbn:de:0287 2016-B022-8

20. **M. Bichra**, C. Shakher, G S. Khan, D R. Burada, S. Sinzinger; K. Pant “Investigations on sub-aperture stitching approach for testing freeform optics” In: OSA -Washington, DC, (2015);http://dx.doi.org/10.1364/ AOMS.2015. JT5A.12K

21. K. Panta, D. Ramu, **M. Bichra**, G S. Khan, S. Sinzinger , A. Ghosh , C. Shakher “Subaperture stitching for measurement of freeform wavefront using scanning Shack Hartmann Sensor”, XXXIX Conference of the Optical Society of India International Conference on Optics and Photonics ,ICOP2015, Calcutta, INDIA.

22. D. Ramu, K K. Pant, **M. Bichra**, G S. Khan, S. Sinzinger, C. Shakher "Shack- Hartmann Sensor Based Freeform Surface Metrology" XXXIX Conference of the Optical Society of India International Conference on Optics and Photonics ,ICOP2015, Calcutta, INDIA.

23. K. Pant, D. Burada, **M. Bichra**, S. Mahendra, G.Amitava, G.S Khan S.Sinzinger C. Shakher "Subaperture stitching for measurement of freeform wavefront" -In: Applied optics. -Washington, DC : Optical Soc. of America, ISSN 15394522, Bd. 54 (2015), 34, S. 10022-10028

24. V. Zürbig, D. Pätz, J. Fries, **M. Bichra**, W. Pletschen, K. Holc, M. Reusch, C. Nebel, S Sinzinger, O. Ambacher, "Tunable multisegment Si x N y /AlN piezo lenses for wavefront correction" –In: 2015 Transducers -2015 18th International Conference on Solid-State Sensors, Actuators and Microsystems (Transducers) / Transducers ; 18 (Anchorage, Alas.) : 2015.06.21-25. -Piscataway, NJ : IEEE (2015),S. 2045-2048

25. **M. Bichra**, S. Sinzinger "Innovative Verfahren zur Charakterisierung von Freiformoberflächen" Workshop "Gradient Based Optical Metrology" 01/2.10.2015 BIAS, Bremen,Germany.

26. **M. Bichra**, N. Sabitov, S. Sinzinger "Wavefront sensor based on modified Talbot effect" DGaO proceedings 2015 -http://www.dgao-proceedings.de -ISSN: 1614-8436 -urn:nbn:de:0287-2015-P009-submitted: 16.Jul.2015 -published: 19.Aug.2015

27. **M. Bichra**, F. Schurig, S. Sinzinger "New method for optical shape measurement of refractive surfaces" EOSMTOC IX: Testing for Fabrication and Assembly münchen 2015, Germany.

28. **M. Bichra**, N. Sabitov, S. Sinzinger "Fourier-Based Diffractive Shearing Interferometer for Wavefront Sensing" XXXIX Conference of the Optical Society of India International Conference on Optics and Photonics ,ICOL 2014 Derhardun, India.

29. **M. Bichra**,N. Sabitov, S. Sinzinger "Vorrichtung und Verfahren zur Vermessung zumindest teilweise reflektierender Oberflächen" –Best PosterIn: DGaOProceedings.-Erlangen-Nürnberg: Dt. Gesellschaft für angewandte Optik, ISSN 16148436, Bd. 115 (2014), insges. 1S.

30. **M. Bichra**, J. Schuppich, S. Sinzinger "Absolute Method for measuring the surface shape of reflective freeform optics" IONS 2014 Ankara. Turkey.

31. F. Schurig, **M. Bichra**, S. Sinzinger „Method and apparatus for detecting the surface shape of reflective freeform optics"In: Frontiers in optics / Frontiers in optics ; 98

(Tucson, Ariz.) : 2014.10.19-23.Washington, DC : OSA, The Optical Society, (2014)2014, ISBN1557522863http://dx.doi.org/10.1364/FIO.2014.FW5A.3

32. M. Hillenbrand, A. Grewe, **M. Bichra**, R. Kleindienst, L. Lorenz, R. Kirner, R. Weiß, S Sinzinger "Parallelized chromatic confocal sensor systems" -In: Conference Optical Measurement Systems for Industrial Inspection ; (Munich) : 2013.05.13- 16. -Bellingham, Wash. : SPIE (2013), insges. 10 S.

33. **M. Bichra**, S. Sinzinger "Freeform Optics at the Ilmenau University of Technology:Design, Fabrication, and metrology" International conference of optics ICO2013 Setif, Algeria.

34. G. S. Khan, **M. Bichra**, A. Grewe, N. Sabitov, K. Mantel. I. Harder, A. Berger, N. Lindlein, S. Sinzinger "Metrology of freeform optics using diffractive null elements in Shack-Hartmann sensors" EOSMOC 2013: 3rd EOS Conference on Manufacturing of Optical Components, Munich, 12.5.-16.5.2013.

35. M. Hillenbrand, A. Grewe, **M. Bichra**, B. Mitschunas, R. Kirner, R. Weiß, S.Sinzinger" Chromatic information coding in optical systems for hyperspectral imaging and chromatic confocal sensing".In: Optical Systems Design; (Barcelona): 2012.11.26-29.-Bellingham, Wash.: SPIE(2012

36. M. Hillenbrand, B. Mitschunas. C Wenzel, A. Grewe, X. Ma, P. Feßer, **M. Bichra**, S. Sinzinger"Hybrid hyperchromats for chromaic confocal sensor systems" In: Advanced Optical Technologies. -Berlin : De Gruyter, ISSN 21928584, Bd. 1 (2012),3,S.187-194

Erklärung

Ich versichere, dass ich die vorliegende Arbeit ohne unzulässige Hilfe Dritter und ohne Benutzung anderer als der angegebenen Hilfsmittel angefertigt habe. Die aus anderen Quellen direkt oder indirekt übernommenen Daten und Konzepte sind unter Angabe der Quelle gekennzeichnet.

Bei der Auswahl und Auswertung folgenden Materials haben mir die nachstehend auf geführten Personen in der jeweils beschriebenen Weise unentgeltlich geholfen:

1. Dr.-Ing. Nail Sabitov: Bei der Erstellung der Auswertprogramm.
2. Patrick Feßer: Bei der Herstellung und Charakterisierung der diffraktiven optischen Elemente.
3. Dr.-Ing. Mostapha Agour: Bei der Implementierung des Frankot Shelappa-Algorithmus

Weitere Personen waren an der inhaltlich-materiellen Erstellung der vorliegenden Arbeit nicht beteiligt. Insbesondere habe ich hierfür nicht die entgeltliche Hilfe von Vermittlungs- bzw. Beratungsdiensten (Promotionsberater oder anderer Personen) in Anspruch genommen. Niemand hat von mir unmittelbar oder mittelbar geldwerte Leistungen für Arbeiten erhalten, die im Zusammenhang mit dem Inhalt der vorgelegten Dissertation stehen.

Die Arbeit wurde bisher weder im In- noch im Ausland in gleicher oder ähnlicher Form einer Prüfungsbehörde vorgelegt.

Ich bin darauf hingewiesen worden, dass die Unrichtigkeit der vorstehenden Erklärung als Täuschungsversuch bewertet wird und gemäß § 7 Abs. 10 der Promotionsordnung den Abbruch des Promotionsverfahrens zur Folge hat.

Heidenheim, 30.01.2020 *Mohamed Bichra*